Parametric Processes for Generation and Low Noise Detection of Infrared Light

Experimental and Numerical Investigation of Fundamental Parameters for the Design of PPLN-based Light Sources and Detector Systems

Høgstedt, Lasse

Publication date:
2016

Document Version
Publisher's PDF, also known as Version of record

Ph.D. Thesis

DTU Fotonik
Department of Photonics Engineering

Parametric Processes for Generation and Low Noise Detection of Infrared Light

Experimental and Numerical Investigation of Fundamental Parameters for the Design of PPLN-based Light Sources and Detector Systems.

Lasse Høgstedt

DTU Risø Campus 2016

Summary

This thesis describes an experimentally based, and application oriented investigation of sum- and difference frequency generation for photon conversion, from one spectral domain to another. The applications in focus are coherent gas spectroscopy in the near- and mid-infrared regimes. The investigations analyse and measure the influence of the different parameters that defines the physical properties of the applied nonlinear optical processes. The emphasis is on how to use the parametric processes as an engineering tool for designing versatile lightsources and low noise detection systems.

The first chapter of the thesis introduces and motivates the work with frequency conversion, sketching the potential of the noise properties for upconversion based detection systems and the increased wavelength availability for parametric light sources. A selection of prior work is presented to give an overview of the focus in the field and to place the thesis in a general context.

The second chapter introduces the basic concepts of nonlinear parametric interaction in the context of this work, where phasematching is a key factor in the work on both light sources and detection systems.

Third chapter presents the work on infrared light sources. An optical parametric generator was constructed, and worked as an optical parametric amplifier for both a near- and a mid-infrared seed. The setups are analyzed spectrally and temporally, and discussed with respect to spectroscopic applications. It is concluded that the light source experiments have provided a solid understanding and experience with parametric processes and key aspects of the choice of light sources. It is furthermore concluded that with the resources and scope of the project it was not feasible to continue with application testing using light sources produced in-house.

Chapter four changes the focus to upconversion based detection systems, where the prior work is sparser. A compact intracavity upconversion module was constructed and described in the context of an efficient and low noise detection system. A special emphasis is on the noise sources that originate from the upconversion process and how these relate to the poling errors in the nonlinear crystal. The poling errors are measured, and a model is constructed to explain the measured noise features and dependencies of the generated noise.

In the fifth and last main chapter, two different upconversion modules are tested as part of a detection system in two different applications for spectroscopic gas measurements. The first test was done at Lund University together with the Combustion Physics Group, where the detection level of acetylene gas in a four-wave mixing setup was improved a factor of 500 compared to previous measurements. The second test was performed at the Atmospheric Physics

Department at the German Aerospace Center in Oberpfaffenhofen. Here the upconversion detector was tested as an alternative to an InGaAs detector in a differential absorption lidar setup for long range measurements of atmospheric CO_2. The test demonstrated great potential for the upconversion system in combination with photomultiplier tubes for the visible region, and revealed special challenges regarding the etendue of long range detection systems based on an upconversion process.
Finally the thesis is concluded with a summary of the major findings together with an outlook sketching the future potential for the application of the upconversion technology within infrared spectroscopic.

Resumé

I denne eksperimentielle og anvendelsesorienterede afhandling, undersøges sum- og differensfrekvensgenerering til konvertering fra et bølgelængdeområde til et andet. De primære anvendelser er kohærent gasspektroskopi i det nær- og midt-infrarøde regime. Undersøgelserne analyserer og bestemmer påvirkningen fra de forskellige parametre, der definerer de fysiske egenskaber for de anvendte ikke-lineære optiske processer. Den primære fokus vil være på hvordan de parametriske processer kan anvendes som et udviklingsværktøj til design af alsidige lyskilder og støjsvage detektionssystemer.
Det første kapitel af afhandlingen introducerer og motiverer arbejdet med frekvenskonvertering og opridser de potentielle støjegenskaber for detektionssystemer baseret på opkonvertering samt den øgede bølgelængde tilgængelighed for parametriske lyskilder. For at give et overblik over feltet og placere afhandlingen i en relevant kontekst præsenteres et udvalg af artikler.
I det andet kapitel introduceres de grundlæggende koncepter for ikke-lineær parametrisk interaktion, indenfor rammerne af dette arbejde, hvor fasetilpasning er centralt i arbejdet med både lyskilder og detektionssystemer.
Tredje kapitel præsenterer arbejdet med infrarøde lyskilder. En optisk parametrisk generator blev konstrueret og fungerede som forstærker for både et nær- og et midtinfrarødt kim. Opstillingerne er analyseret spektralt og rumligt, samt diskuteret med hensyn til spektroskopiske anvendelser. Det konkluderes at eksperimenterne med lyskilder har givet en god forståelse for, og erfaring, med parametriske processer og centrale koncepter i valget af lyskilder. Endvidere konkluderes det at ikke er opnåeligt indenfor projektets rammer og med de tilstedeværende ressourcer at arbejde videre med egne lyskilder.
I kapitel fire ændres fokus til at omhandle opkonverteringsbaserede detektionssystemer, hvor omfanget af tidligere publiceret arbejde er begrænset. Et kompakt intrakavitets opkonverteringsmodul blev bygget, samt beskrevet i forbindelse med et effektivt og støjsvagt detektionssystem. Der bliver lagt særlig vægt på de støjkilder der stammer fra opkonverteringsprocessen og hvordan disse relaterer til polingsfejlene i den ikke-lineære krystal. Polingsfejlene blev målt, og en model blev konstrueret for at forklare sammenhængende mellem de målte støjegenskaber og den generede støj.
I det femte og sidste hovedkapitel blev to forskellige opkonverterings moduler undersøgt som en del af et detektionssystem i to forskellige anvendelser indenfor gasspektroskopiske målinger. Den første test blev udført på Lund Universitet sammen med gruppen for forbrændingsfysik, hvor detektionsniveauet for acetylen blev forbedret 500 gange sammenlignet med tidligere målinger. Den anden undersøgelse blev udført på afdelingen for atmosfærefysik ved det tyske

rumforskningsagentur i Oberpfaffenhofen. Her blev opkonverteringsdetektoren undersøgt i en differential-absorptions lidaropstilling til langdistancemåling af atmosfærisk CO_2, som et alternativ til en InGaAs-detektor. Undersøgelsen viste et stort potentiale for kombinationen af et opkonverteringssystem og et fotomultiplikationsrør, følsomt i det synlige regime, samt afslørede særlige udfordringer med areal-åbningsvinkelproduktet for opkonverteringsbaserede langdistance detektionssystemer.
Endelig bliver afhandlingen konkluderet med en opsummering af de vigtigste opdagelser sammen med en udsigt mod det fremtidige potentiale indenfor anvendelsen af opkonverteringsteknologien til infrarød spektroskopi.

Preface

This thesis presents the outcome of a Ph.D. study performed from 2012-2015 at the Technical University of Denmark at the Department for Photonics Engineering in the Optical Sensor Technology Group. The experimental work was primarily done in the laboratory facilities at Risø Campus, and secondarily at Lund University at the laboratories for the Combustion Physics group, and at the German Aerospace Center (DLR) in Oberpfaffenhofen in the laboratories at the Atmospheric Physics department.
The thesis represents original work done by me unless other is stated. It is a mix of published and unpublished work, which will be noted in the specific sections when suitable. The work is a continuation of my master thesis in the same group, entitled *Infrared Light Generation and Detection Systems Based on Three-wave Mixing* and is financed fully by the basic Ph.D. funding at the Technical University of Denmark.

Acknowledgements

First of all I would like to thank my supervisors Peter Tidemand-Lichtenberg and Christian Pedersen. They have guided me through the project and trusted me when I embarked on my own ideas. Their door was always open and there was always time for a physics discussion or supervision on the solid state lasers in the lab. From the Optical Sensor Technology group I would furthermore thank my friend and colleague Qi Hu for many good discussions, comments, questions and a thorough proofreading. I would also like to thank Jeppe Seidelin Dam for engaging in many of the discussions with good ideas and technical expertise, and for the collaboration with the measurements at Lund University. From the Nonlinear Optics Group at DTU Fotonik, I would like to thank Søren Michael Mørk Friis for the many fruitful discussions on the modeling work. At the Danish Metrology Institute I would like to thank Nikolaj Agentoft Feidenhans'l for the help with the microscope measurements.
From the Combustion Group at Lund University, I would like to thank Anna-Lena Sahlberg and Li Zhongshan for believing in our ideas and helping in their lab with incorporation of the upconversion detector. Lastly, I would like to thank Andreas Fix from the Atmospheric Physics Department at the German Aerospace Center for engaging so full-hearted in the project with testing an upconversion based detector system and for many hours of help in the lab.

- Lasse Høgstedt, December 2015

List of Publications

First Author

1. **Upconversion-based long-range CO_2 DIAL measurements**
   Journal paper
   Lasse Høgstedt, Andreas Fix, Martin Wirth, Christian Pedersen, Peter Tidemand-Lichtenberg
   Optics Express, Volume 24, Number 5, Pages 5152-5161 (2016)

2. **Low-noise mid-IR upconversion detector for improved IR-degenerate four-wave mixing gas sensing**
   Journal paper
   Lasse Høgstedt, Jeppe Seidelin Dam, Anna-Lena Sahlberg, Zhongshan Li, Marcus Aldén, Christian Pedersen, Peter Tidemand-Lichtenberg
   Optics Letters, Volume 39, Number 18, Pages 5321-5324 (2014)

3. **Direct seeded single frequency mid-IR OPA all passive light source**
   Conference paper, award for best poster
   Lasse Høgstedt, Peter Tidemand-Lichtenberg, Christian Pedersen
   Advanced Solid State Lasers, Optical Society of America, JTh2A. 23 (2013)

4. **Upconversion enhanced degenerate four-wave mixing in the mid-infrared for sensitive detection of acetylene in gas flows**
   Conference paper
   Lasse Høgstedt, Jeppe Seidelin Dam, Anna-Lena Sahlberg, Zhongshan Li, Marcus Aldén, Christian Pedersen, Peter Tidemand-Lichtenberg
   SPIE LASE, International Society for Optics and Photonics, 89641H-89641H-6 (2014)

5. **Design of a solid state laser for low noise upconversion detection of near infrared light**
   Conference paper, award for outstanding student poster
   Lasse Høgstedt, Peter Tidemand-Lichtenberg, Christian Pedersen
   Advanced Solid State Lasers, Optical Society of America, AM5A. 6 (2015)

Co-author

1. **Mid-IR Imaging: Upconversion imager improves IR gas sensing**
   Invited paper
   Anna-Lena Sahlberg, Zhongshan Li, Lasse Høgstedt, Peter Tidemand-Lichtenberg, Jeppe Seidelin Dam
   Laser Focus World, Volume 50, Number 11, Pages 53-55 (2014)

2. **Non-collinear upconversion of infrared light**
   Journal paper
   Christian Pedersen, Qi Hu, Lasse Høgstedt, Peter Tidemand-Lichtenberg, Jeppe Seidelin Dam
   Optics express, Volume 22, Number 23, Pages 28027-28036 (2014)

3. **Tunable 1.9 µm laser system for mid-IR upconversion detection**
   Conference paper
   Rasmus Pedersen, Peter Tidemand-Lichtenberg, Lasse Høgstedt
   Advanced Solid State Lasers, Optical Society of America, ATh1A. 8 (2015)

Supervised Master Projects

1. **Numerical modeling of optical parametric frequency conversion**
   (2014)
   Author: Anders C. Bilfeldt
   Supervisors: Peter Tidemand-Lichtenberg and Lasse Høgstedt

2. **1.9 µm laser system for mid-IR upconversion detection**
   (2015)
   Author: Rasmus Lyngbye Pedersen
   Supervisors: Peter Tidemand-Lichtenberg and Lasse Høgstedt

Contents

CHAPTER 1

Introduction

This, first chapter, introduces and motivates the work, and gives a brief introduction to a selection of prior work in the field. Second chapter explains the relevant physics and technology used in the project, as support for the discussions and analysis throughout the following chapters.
Third chapter presents the first phase of the project, where two pulsed mid-infrared (MIR) light sources was constructed and characterized. The fourth chapter presents the parametric upconversion process as a detection technology together with visible light detectors. The constructed upconversion module is presented, and through experiments and simulations it is investigated how noise and efficiency depend on different design parameters.
Chapter five presents two applications of the upconversion technology. First test was conducted in collaboration with Lund University, where the upconversion technology was tested in a setup for detection of low concentrations of acetylene. Secondly a new upconversion system was tested, in collaboration with the German Aerospace Center, as a detector technology for a long range DIAL system for measurement of greenhouse gas concentrations in the atmosphere. The thesis is concluded in chapter six with a summary of the primary findings and a discussion of future improvements for the upconversion technology applied in low noise infrared detector systems.

1.1 Project Goals

The overall goal of the project was to investigate the possibility of using efficient parametric conversion for gas spectroscopy. This materialized into 3 parts, which are reflected by the lightsource, the detector and the application chapter in the thesis.

- Build and test a tunable pulsed light source in the mid-infrared wavelength regime using an PPLN crystal for downconversion.

- Test and optimize an intracavity conversion module in an upcoversion configuration for the use with a visible light detector in a low noise detection system.

- Test the light source and/or detector in a demonstration of remote infrared gas spectroscopy.

1.2 Motivation

The laser was invented in the early sixties, and few years passed before the field of nonlinear optics started to gain speed. In this early period, one of the many phenomena discovered and described for the first time was nonlinear parametric conversion of light. The backbone of the theory was established, and optical wavelength conversion of light between different spectral regimes using a laser and a nonlinear crystal was demonstrated. Some progress was made on parametric light sources and they were readily used in many labs. For the use with detection, however, the scientists were aware of the potential within this area, but twenty years went by, only with little progress, until the technology was ready for a rediscovery of the parametric upconversion. This was a result of general laser technology improvements and a rising need for infrared technology, but the key enabling technology was the discovery of the periodic poling technique. With this technology it became possible to engineer the nonlinear properties of the crystals and provide efficient conversion between the wavelength regimes at the exact wavelength needed for a specific application.
The technology has proved especially valuable to access the infrared wavelength region. The detectors in this region are challenged by thermal noise and require extensive cooling and the design of light sources are challenged by the lack of suitable gain materials. The up- and downconversion process is a technological shortcut that extents the functional region of the best and most optimized detector and light source technologies. An overview of the technologies in the different wavelength regions are given in figure 1.1 and 1.2. In the mid-infrared

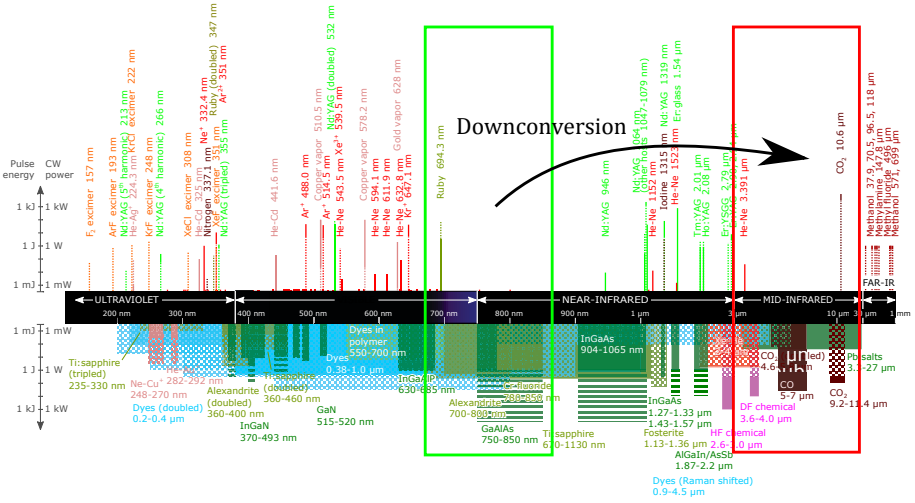

Figure 1.1: Overview of selected commercially accessible laser lines. Reproduced from [1].

region there is access to many important applications. Thermal surveillance and laser cutting are two widespread examples, but it is in the large variety of

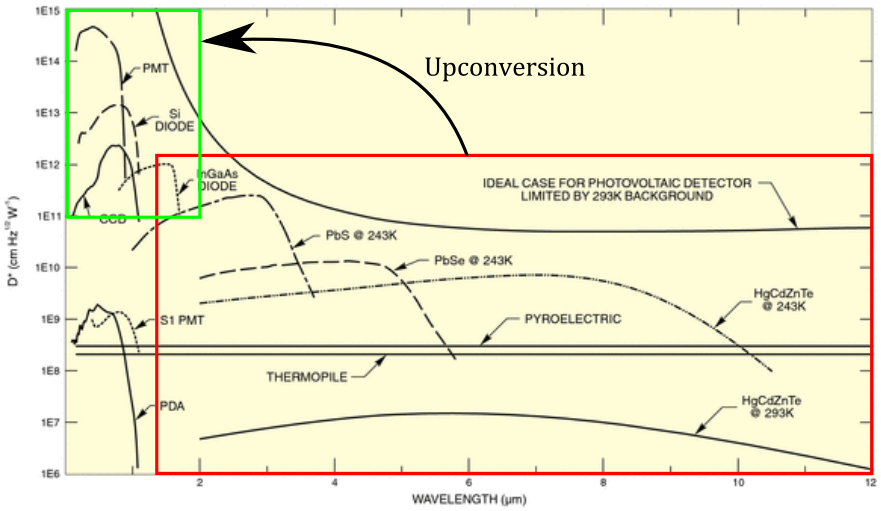

Figure 1.2: Overview of detector technology available for different wavelengths and their specific detectivities. Reproduced from [2].

spectroscopic applications that the parametric technology has the most advantages. Light sources can be downconverted to match inaccessible wavelengths and upconversion allow the use of the low noise uncooled detectors to detect weak signals in the infrared regime. Simply place an upconversion module in front of a silicon detector, and it becomes an infrared detector. This opens up for spectroscopy with a new level of sensitivity, and with this, new applications like long range gas concentration surveillance, early disease checking from breath analysis, and compact spectral imaging systems.
The main reason for changing the signal wavelength to higher energies is to minimize the thermal noise caused by black body radiation. This enters inherently as noise in all photon detectors. Following the Planck curve the amount of emitted photons peaks at 20 μm, at room temperature, and the amount is 40 orders of magnitude smaller in the visible light region. This is a theoretical value and in reality it corresponds to virtually zero photons emitted in the visible range. This show the potential for improved detection by upconversion and this thesis shows that the advantages occur already in the near infrared (NIR) region of light. In the mid-infrared (MIR) region it improves further, and not only giving a substantial decrease in noise, but also removing the need for cryogenic cooling.

1.3 Prior Work

As a background for the discussions in the thesis, and to place the work in a larger content, a brief overview of the work within parametric detector systems and light sources is presented. Additional references will be used throughout

the thesis and there are obviously much more published. A selection of some that are representative and important for this study is presented in this section.

1.3.1 The Pioneering Years

In the first decade after the invention of the laser, the fundamental discoveries within photonics came frequently, and in this period the first measurements and theoretical descriptions of parametric interaction was done. It all started when Franken et al.[3] in 1962 demonstrated second harmonic generation of a ruby laser.
After this case of degenerate parametric upconversion Armnstrong et al. [4] wrote a theoretical paper describing the interaction of light waves in nonlinear dielectrics. Here the nonlinear source terms were derived using quantum mechanical pertubation theory, and in combination with Maxwells equations, the three coupled differential equations for the parametric three wave mixing were derived. An analysis of the phasematch condition and cases with perfect and non-perfect phasematch was presented. Periodic poling was described together with two other methods as possible technologies for obtaining phase matching, see figure 1.3.

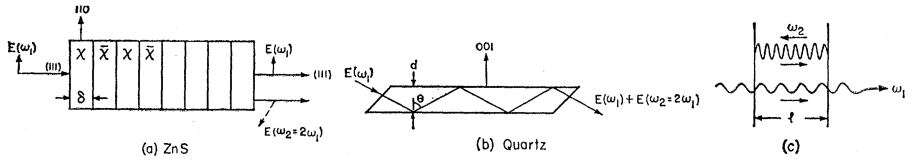

Figure 1.3: a) Inversion of the nonlinear suceptibility. b) Multiple total reflections in crystal with d thickness. c) Phasematching in forward direction with an interferometer cavity. Reproduced from [4]

In 1967 Midwinter and Warner [5] demonstrated 1% quantum efficiency for upconversion of the 1.7072-μ Hg emission line, mixing with a Q-switched ruby laser in a 1 cm long lithium niobate bulk crystal. Temperature sweeping of the phasematch condition was used for measuring the Hg-lamp spectrum and the upconversion technology was discussed for the use as an infrared detector. They concluded that the process showed more noise than theoretically expected.
Part of the process for the unexpected noise was examined further by Byer and Harris [6] in 1968, where an Argon laser was passed through a 1 cm long bulk lithium niobate crystal. Measurements together with the corresponding theory were presented for the generation of spontaneous parametric emission, and both angular and temperature dependencies were investigated. It was proved, that the spontaneously emitted signal power depends linearly on the pump power, the crystal length and the accepted solid angle as [6]

$$P_s = (\beta L P_p/b)\pi\theta^2 \qquad \beta = \frac{2\nu_s^4\nu_i d_{15}^2\hbar n_s}{(2\pi)^2\epsilon_0^3 c^5 n_i n_p} \tag{1.1}$$

where ν_j are the frequencies, n_j the refractive indices, d_{15} the nonlinear coefficient, L the crystal length, P_p the pump power, b a dispersive constant, ϵ_0 the vacuum permittivity, c the speed of light and $(\pi\theta^2)$ the accepted solid angle of the detector.
The full process for the spontaneous parametric noise in the upconversion process was derived quantum mechanically in 1969 by C.L. Tang [7]. He presented the theory for phase matched upconversion of non-phasematched spontaneous parametric downconverted (SPDC) photons and derived an expression for the emitted power in the case of both full and limited detector angle acceptance. Figure 1.4 illustrates the second order parametric process.

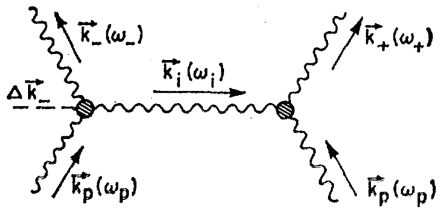

Figure 1.4: Sketch of the combined process for upconversion of spontaneously parametric downconverted photons. Reproduced from [7]

In 1968 [8] Boyd and Kleinman published a theory for the parametric interaction in the case of Gaussian beams. Before that, most calculations assumed plane waves, but for tightly focused laser beams this is not a valid assumption. The paper presented a way to determine the optimal relation between beam waist and crystal length for different parametric processes.
On the application side, much of the early work focused on upconversion detection for infrared astronomical observations. The first demonstration was published by Gurski et al. in 1975 [9]. In 1976, a more thorough theoretical and experimental investigation of the infrared upconversion potential was conducted by Abbas et al. [10], and they concluded that the technology may soon be ready for an efficient imaging upconversion system. However, already in 1977 Boyd closed the astronomical dreams in a review paper, where he concluded that the lasers needed more power, the nonlinear coefficients were too small and the added noise too large [11].
In 1977, intracavity upconversion with $LiNbO_3$ was demonstrated for the first time by Falk and See [12]. In the beginning of the eighties, it was generally accepted that the noise properties and the quantum efficiency of the upconversion based detection was limited by the accessible technology [13] and not advantageous to use in detector systems. More than twenty years passed before the area was rediscovered with the introduction of high quality periodically poled lithium niobate (PPLN) crystals.

1.3.2 Recent Advances Within Upconversion Detection

The research group headed by Marty Fejer published on upconversion detection in PPLN waveguides in 2004 [14]. The purpose was to detect photons at the telecommunication wavelength (1550 nm) with higher quantum efficiency (QE) and lower noise than the existing InGaAs detectors. A QE above >80 % was demonstrated in a single pass configuration using a 4.8 cm long PPLN waveguide, manufactured in-house, with a 1.5 μm signal and an 1.3 μm mixing laser.
It turned out, that the periodic poling had a random duty cycle (RDC) error that increased the amount of generated SPDC noise photons by changing the overall phasematching properties of the crystal. The problem with RDC errors is treated in [15] and [16]. The subject of upconverted SPDC is not investigated further, but in [17] it is mentioned as one of the reasons for changing to a pump at a wavelength longer than the signal. This approach is continued in the Stanford group and the noise has been reduced further by post filtering with a volumetric Bragg grating in 2013 [18]. This low noise and high QE setup has been demonstrated in a test application as an upconversion based long-range micro-pulse lidar at 1.5 µm [19] tested for aerosol detection in China.

An intracavity upconversion setup for low noise detection of 1550 nm photons was reported in 2006 by Pan and Zeng [20]. Figure 1.5 displays the setup and main result. It was concluded, that the main noise source were upcon-

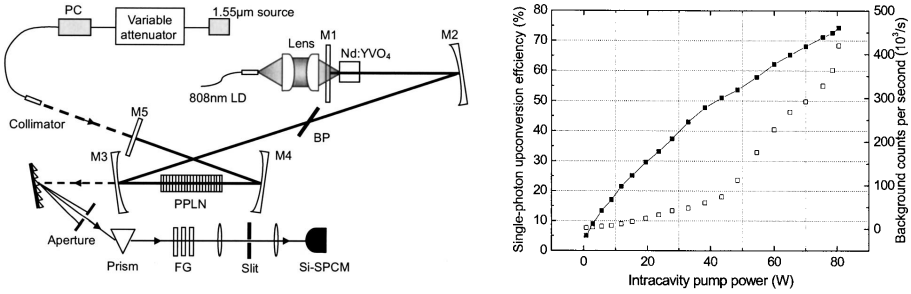

Figure 1.5: Left: Experimental setup of the intracavity PPLN based setup for efficient low noise detectionof 1550 nm. Right: Upconversion efficiency and parametric noise plotted as a function of intracavity pump power. Reproduced from [20]

verted fluorescence or the previously named upconverted SPDC. Both setup and results resemble parts of this thesis, and for some of the results it will be regarded as the nearest prior work.
In 2014, a NASA research group presented a very similar setup for the purpose of CO_2 measurements in the atmosphere around the 2 μm absorption band [21]. The lab demonstration showed high QE and low noise due to a double prism noise suppression setup.
The upconversion technique have furthermore been tested for the use with an astronomical telescope, where the 1550 nm light from the telescope was upcon-

verted in a single pass system with a 1064 nm pump and a PPLN crystal [22].

The Optical Sensor Technology group entered the field of upconversion with the work on incoherent image upconversion at the MIR wavelengths [23] where upconversion imaging was demonstrated for the first time in many years. In 2012, single photon spectral imaging was demonstrated at room temperature [24] in an intracavity setup. The incoherent signal was mixed with the 1064 nm pump in a 20 mm long PPLN crystal and 20 % QE was obtained. This work paved the road for an expansion into the upconversion field. In the recent years, the upconversion technology in the Optical Sensor Technology group have been tested for various applications such as high resolution spectroscopy [25] and hyper spectral imaging [26]. Further tests with concentrations measurements of acetylene gas flows, and long range detection of atmospheric CO_2 is addressed in the application chapter 5 in this thesis.

1.3.3 Light Sources

In the field of light sources, parametric generation is used as a standard method in tunable laser systems. Often it is possible to achieve high output powers, and in spectroscopy systems this is a simple way to overcome the higher noise levels in infrared detectors.
In 1999 Dunn and Ebrahimzadeh published review [27] on "parametric generation of tunable light from continuous-wave to femtosecond pulses". The versatility of the parametric light sources in both the temporal and the spectral domain are presented, and it is concluded that the technology have further potential to widen the spectral coverage, increase the CW capabilities and scale down in size. In 2015, some of that potential was presented in the review paper by Valentin Petrov [28], as an overview of the existing work on parametric MIR light sources, and a collection of important parameters for the nonlinear crystals required to reach the MIR wavelengths. Figure 1.6 shows an overview graph from each of the two review papers.

The Stanford group is also represented with their work on both pulsed and CW optical parametric oscillators, where they demonstrated their poling procedure of lithium niobate for the first time in 1995[29].
Work on seeded optical generators are especially relevant for the light source chapter of this thesis, and examples of Q-switch 1064 nm pumped optical parametric generator setups using PPLN crystal are found in [30, 31]. Both demonstrate how the spectral bandwidth of the output narrows upon NIR seeding and how high intensity narrow band ns-pulses can be created with overall QE's around 40 %.
Powers et al. 1998 [32] demonstrates the same principle in a combined OPG and OPA setup where both stages are PPLN crystals pumped with a pulsed 1064 nm laser. The first stage works as a tunable seed for the second stage through a tunable Fabry Perot interferometer. This result in a mode-hop free tunable light source, suitable for MIR spectroscopy, using only a single pump laser. This is claimed in the paper, but with no temperature tuning of the crystals, the tuning range is limited by the bandwidth of the phasematch condition

for the parametric process.
A more complex approach using two PPLN crystals is demonstrated in [33]. The first master oscillator stage is a piezo controlled OPO, pumped with a single frequency diode laser, that delivers a single frequency seed to a second OPO amplifier stage. This second cavity is piezo controlled and locked to the master oscillator cavity, giving the opportunity for single frequency MIR generation with a high power and spectrally broad 1064 nm pump. The tuning was done by tuning the diode laser pump for the master oscillator. Compared to [32], the increased complexity relaxes the demands for a high quality pump, and thus allows for higher pump powers and potentially higher output energies.
An unseeded, but very compact system for generation of MIR ns-pulses is demonstrated in [34], where a 12 W fiber coupled diode laser pumps an OPG module. This module is 5 cm long and consists of a focusing lens, a passively Q-switched laser and a 13 mm long PPLN crystal. The light source is suggested as a low cost broadband light source for absorption spectroscopy with calculated bandwidths of 250 nm in the MIR regime.
The newest research in the field of parametric light sources are moving towards longer wavelengths as presented by Petrov in [28] and Clement et al.[35]. Clement et al. presents a single frequency tunable pulsed light source based on an orientation patterned GaAs crystal. This light source is built as a dual-cavity parametric oscillator with one of the cavities nested in the other. The cavities share a common mirror and have individual piezo controlled mirrors for each cavity. With the right relation between the cavity lengths, single frequency lasing is obtained. The laser is scanned within the 50 nm phasematch of the crystal and tested for spectroscopy with two MCT detectors that measured the spectra of ammonia around the 10.393 nm peak. The two setups are reproduced in figure 1.7

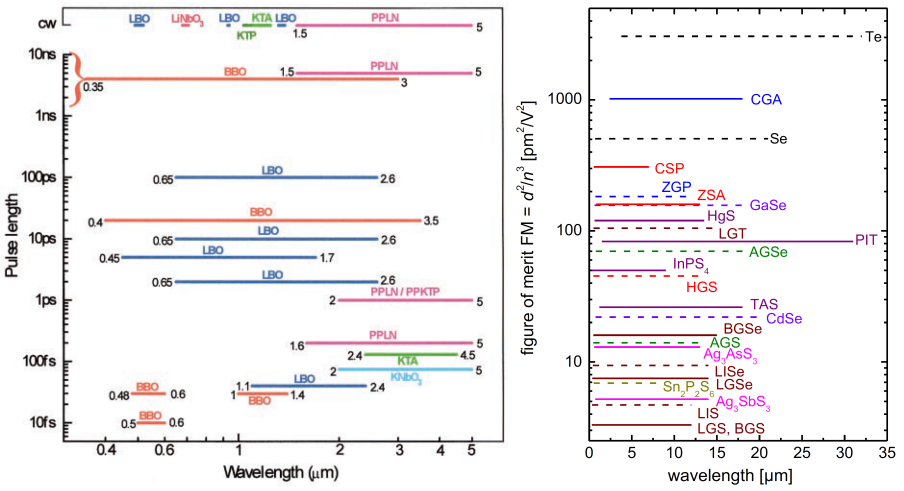

Figure 1.6: Overview of the different nonlinear crystals used parametric light sources reported in literature. Note the difference in y-axis on the two plots. Reproduced from [27] and [28], left and right, respectively.

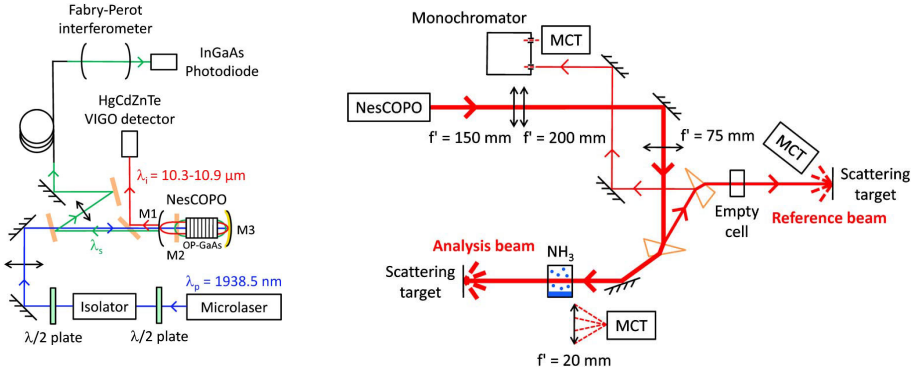

Figure 1.7: Left: Dual-cavity double resonant nanosecond single-frequency nested cavity optical parametric oscillator with emission wavelength around 10 µm. Right: LWIR light source implemented in an absorption spectroscopy setup for detection of NH_4. Reproduced from [35]

CHAPTER 2

Physics and Technology

This chapter gives an overview of the primary physical principles and technologies that form the basis for the analysis and discussions throughout the thesis. First section will describe the nonlinear interaction of the second order parametric processes and the governing equations. The next section goes into depth with the concept of phasematching and field build-up, before the properties, production, and errors of PPLN are presented in the last section.

2.1 Nonlinear Interaction

The interaction between a nonlinear crystal and light can be described as an electric field that excites an oscillation of the electrons in a crystal lattice. In the linear regime, the light is emitted at the same frequency as the incoming light, and the light that exits the crystal is identical to the light that enters. If a high field drives the electronic cloud to larger oscillations, or if the nonlinearity of the crystal is high, the frequency of the emitted light include additional components and higher order terms is required to describe the oscillations.
Second order effects include second-harmonic generation, parametric frequency conversion and the Pockells-effect. The parametric process in the form of both sum- and difference frequency generation describes a process, where energy flows between three different frequencies, defined by the energy conservation of the process. The energy flow is controlled by the phase of the fields and thus the parameters for a specific crystal, such as temperature, angle, and refractive index. The efficiency of the nonlinear interaction depends on the strength of the nonlinear excitation and thereby both the nonlinear coefficient, the intensities of the interacting fields, and the length of the crystal where the fields overlap efficiently.
The equations governing the energy conservation are given as

$$\lambda_{\mathrm{MIR}}^{-1} = \lambda_{\mathrm{mix}}^{-1} - \lambda_{\mathrm{NIR}}^{-1} \quad \text{(DFG)} \tag{2.1}$$

$$\lambda_{\mathrm{VIS}}^{-1} = \lambda_{\mathrm{mix}}^{-1} + \lambda_{\mathrm{NIR}}^{-1} \quad \text{(SFG)} \tag{2.2}$$

defined in terms of the interacting wavelengths.
An example of the parametric processes are displayed in figure 2.1, where both the DFG and the SFG process are included. The second harmonic generation

occurs as a special degenerate case and will only appear as a parasitic effect in this work. In case of backconversion, the energy flow will change direction and the SFG will become a DFG process instead. The given convention in figure 2.1 correspond to the main applications in the thesis, and for the SFG process the mixing laser could as well be summed with the MIR component. This would change the phasematch requirement and the generated visible wavelength.

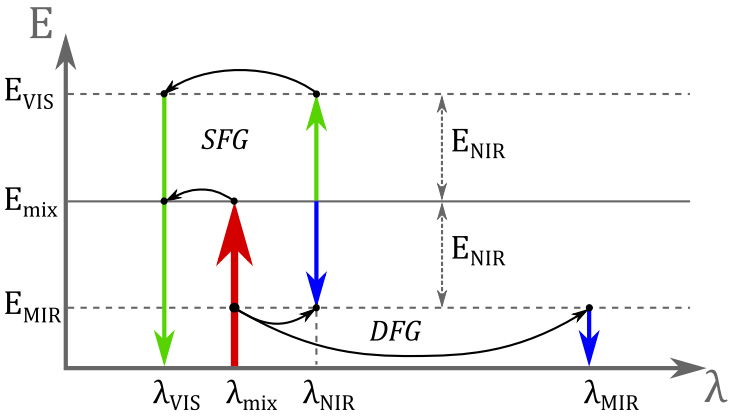

Figure 2.1: Energy and wavelength diagram of the sum and difference frequency processes. The energy flow will shift direction in case of backconversion, i.e. the SFG will become DFG and vice versa. Note that the dashed energy levels are determined by the phasematch condition, if the mixing field is the only field passed through the crystal.

If only one input field is present the dashed energy levels in figure 2.1 will be a continuum of energy levels exited by the vacuum fluctuations as the electronic cloud of the crystal support a continuum of oscillatory modes. In this case the power levels and the spectral width of the output fields from the crystal will be defined by the specific phasematch conditions apparent in the crystal.

If the fields driving the electronic oscillations become very intense they will start to excite oscillations of the atomic structure of the crystal lattice itself. This will result in more direct material interaction and energy will be transferred from the photons to the lattice, as phonons, or in rare cases the other way around. This, third order effect, is called Raman scattering, and a stoke-shift, if energy is lost to the lattice, and an anti-stoke shift if energy is gained. The energy levels are not determined by parameters of the interacting fields, but only by the lattice resonances for the given crystal. In this way the Raman scattering will always result in a generated field at a constant frequency offset with respect to the driving field.

2.1.1 Coupled Field Equations

A common approach for a formalized description of the energy flow between the three fields, in a parametric process, is to construct three coupled photon density equations. This description of the parametric interaction is derived in several textbooks on nonlinear optics, e.g. [36], [37] and [38]. The approach is to derive the nonlinear wave equation from the Maxwell equations, and through several assumptions simplify and rewrite this equation for each of the present fields. The exact formulation of the equations vary for different authors and in this thesis I have chosen to follow the formulation from Saleh&Teich [37]. The differential rate of change for the photon flux is then described as

$$\frac{da_1}{dz} = -iga_3a_2^* \exp(-i\Delta k_{(T,\lambda,\theta)}z) \tag{2.3}$$

$$\frac{da_2}{dz} = -iga_3a_1^* \exp(-i\Delta k_{(T,\lambda,\theta)}z) \tag{2.4}$$

$$\frac{da_3}{dz} = -iga_1a_2 \exp(i\Delta k_{(T,\lambda,\theta)}z) \tag{2.5}$$

where

$$g^2 = \frac{\epsilon_0^{\frac{1}{2}}\mu_0^{\frac{3}{2}}}{n_1n_2n_3}2\hbar d_{eff}^2\omega_1\omega_2\omega_3, \quad I_j = \hbar\omega_j|a_j|^2 \tag{2.6}$$

$$\Delta k = k_3 - k_2 - k_1, \qquad k_j = \frac{2\pi}{\lambda_j}n_{j(\lambda_j,T)} \tag{2.7}$$

and the dependency for the refractive index, n_j, with respect to wavelength, λ_j, and temperature, T is given by the Sellmeier equations described in the experimental paper by Gayer et al. from 2008 [39]. μ_0 is the vacuum permeability, z the crystal position, ω_j the angular frequency and Δk the phasemismatch defining the efficiency of the nonlinear interaction.
The definition of the effective nonlinear coefficient, d_{eff}, is changed to the units of pm/V compared to [37] and thus an extra ϵ_0^2 is multiplied to g^2. In the above formulation of the equations a_3 describe the field with the highest frequency and a_2 and a_1 can be either of the two low frequency components.

To obtain the coupled photon flux equations 2.3-2.5 four assumptions are needed:

Slowly varying envelope approximation Or SVEA is the assumption that the field amplitudes change much slower than the wavelength oscillations of the electromagnetic fields. This approximation may be violated in case of ultrashort pulses.

Monochromatic fields The assumption of monochromatic fields allows the treatment of the energy flow to be split into three separate equations. The assumption is mostly a good approximation due to narrow band widths of the interacting fields. In case of broad band fields, the spectra can be split into sets of monochromatic fields and treated independently.

Plane waves To remove the transverse components in the field equations, it is assumed that the field power is equally distributed over all space in the transverse plane. This is not the case with laser beams, but it is often a good assumption if the Rayleigh length or the confocal parameter of the beam is longer than the crystal length [8]. The efficiency of the energy flow will, however, depend on the focus of the laser beam and the influence is included through the field intensity, I_j.

Photon number conservation or the Manley-Rowe relation states that the parametric transfer of energy from one photon density to another is a reversible process and occurs photon by photon. No photons are lost or gained in other processes. The total number of photons changes throughout the crystal as the energy transfer between the fields, but the rate of change for the three photon densities are kept equal. When the nonlinear process is facilitated by a lithium niobate crystal in the low absorption region it is typically a good assumption that no photons are lost to absorption or scattering.

2.1.1.1 Conversion Efficiency

With further assumptions, it is possible to derive analytical expressions for the energy flow from the coupled equations 2.3-2.5. In the following, the weak and the strong coupling regimes will be treated for frequency mixing and the next section will handle the numerical approach needed to describe three wave mixing in general.

In the weak coupling regime, two of the three frequency components are assumed to be constant, e.g. a constant mixing and signal field for intracavity upconversion (SFG). The three coupled equations reduce to a single equation and the conversion efficiency for the intensity, I_j, is described as [36]

$$I_3(L) = I_1(0)I_2(0)\underbrace{g^2\frac{\omega_3}{\hbar\omega_1\omega_2}}_{\eta_{\text{process}}}\underbrace{L^2\text{sinc}^2\left(\frac{\Delta k(T,\lambda,\theta)L}{2\pi}\right)}_{\eta_{\Delta k}} \Rightarrow \tag{2.8}$$

$$\eta_{1\to3} = \frac{I_3(L)}{I_1(0)} = I_2(0)\eta_{\Delta k}\eta_{\text{process}} \tag{2.9}$$

where the normalized sinc function is used in order to give zero-point values, for integer values of the function parameter. If absorption, scattering, and overlap ratios are included the total conversion efficiency become

$$\eta_{1\to3} = \frac{I_3(L)}{I_1(0)} = I_2(0)\eta_{\Delta k}\eta_{\text{process}}\eta_{\text{overlap}}\eta_{\text{loss}} \tag{2.10}$$

In practice $\eta_{\text{loss}} \simeq 1$, but η_{overlap} only come close to one in systems with good beam scaling design and careful alignment. $\eta_{\Delta k}$ is the phasesmatch dependent conversion efficiency with respect to the perfect phasematched case, and the consequences of this term will be treated separately in section 2.2. Equation 2.8 is valid at low values of $\eta_{1\to3}$, until the signal field starts to deplete and the

process enters the strong coupling regime. The photon number or quantum efficiency is related to the intensity efficiency as

$$QE_{1\to3} = \frac{\omega_1}{\omega_3}\eta_{1\to3} \tag{2.11}$$

The quantum efficiency is limited to a maximum value of unity by the photon conservation, whereas the intensity efficiency for upconversion can exceed unity without obstructing the energy conversion, as energy is transferred from the mixing laser to the signal laser.

In the strong coupling regime, in case of upconversion, the mixing laser is assumed constant, while both signals are allowed to deplete. The coupled equations reduce from three to two (a_1 and a_3) and can be solved analytically in case of perfect phase matching, $\Delta k = 0$. The efficiency of the parametric frequency conversion is then [37]

$$\eta_{1\to3} = \frac{I_3(L)}{I_1(0)} = \frac{\omega_3}{\omega_1}\sin^2\frac{\gamma L}{2}, \quad \gamma^2 = 4g^2\frac{I_2}{\hbar\omega_2} = 8\omega_1\omega_2 I_3 d_{\text{eff}}^2\frac{\epsilon_0^{\frac{1}{2}}\mu_0^{\frac{3}{2}}}{n_1 n_2 n_3} \tag{2.12}$$

where g is defined in equation 2.6. The process begins as a SFG-process and shifts to a DFG-process as back-conversion occurs after depletion of the signal.

If the highest frequency field is assumed constant, back-conversion is not possible and the two other fields will both be amplified throughout the crystal. This case describe the optical parametric amplifier and the three equations are again reduced to two, a_1 and a_2. No frequency conversion occurs and the important process parameter is the gain factor of the nonlinear process. Assuming $\Delta k = 0$ the gain factor for each of the two low frequency fields can be derived as [37]

$$G_{0\to L} = \frac{I_j(L)}{I_j(0)} = \cosh^2\left(\frac{\gamma L}{2}\right), \quad \gamma^2 = 4g^2\frac{I_3}{\hbar\omega_3} \tag{2.13}$$

where $j = 1$ or $j = 2$. This expression can be used to predict the output from a OPA if the seed is known, or to compute the amount of virtual seed from the vacuum fluctuations in an OPG, if the output is measured.

If none of the fields can be assumed constant and if $\Delta k \neq 0$ there is no analytical solution. A numerical solver is then needed to compute how energy flow between the three fields throughout the crystal.

2.1.1.2 Numerical Implementation

The numerical implementation of the coupled equations 2.3-2.5 is applied to support the analysis in several chapters: For a computation of an OPG field evolution in the light source chapter, an investigation of the importance of RDC errors in the detector chapter, and a calculation of the upconversion acceptance angle in the application chapter. Depending on the specific configuration, three

different methods may be applied as the numerical solver. All of them solves the equations step-by-step throughout the full length of the crystal. The chapter on the Runge-Kutta method in [40] is used as basis for the implementation.

Build-in Matlab solver This method implement one of the functions ODE23 or ODE45, that is examples of build-in solvers that are both fast and accurate. They allow the user to control the accuracy, the step number, but not the exact step size. Neither is it possible to solve the set of equations for a range of parameter values at the same time. This method is applied for fast single output value computations with regular grating structures, e.g. the field build-up in an OPA.

First order Runge Kutta (Euler) method This is the simplest possible numerical solver for differential equations. It computes the values of the differential step by step in sufficiently small steps. The solver is slow, compared to both the build-in solver and the fourth order method, but due to the simplicity it is very fast on a single iteration level. In case of a simulation including random errors in the poling structure, the step size have to be small enough to resolve the errors within each domain. With a strict demand for a large step number the Euler method is superior in speed, compared to the fourth order method.

Fourth order Runge Kutta method In case it is necessary to solve the coupled equations for a whole range of values the fastest implementation is to vectorize the input. This is possible with a Runge Kutta solver where each operation can be performed on a whole range of values, e.g. wavelengths or angles. The fourth order method specifically compute several intermediate steps in each iteration and allow for a reduction of the overall step number and computation time, while retaining the same level of accuracy.

Periodic poling of a nonlinear crystal can be implemented in all of the above methods as a z-dependent sign shift for the nonlinear coefficient. This is convenient for an investigation of the microscopic structure of the parametric process. If the interesting results is on the macroscopic scale, e.g. the final power levels, a significant speed up can be obtained by assuming a perfect grating structure throughout the crystal. In this case the effective nonlinearity is reduced by a factor of $2/\pi$ [41], and the step size for each iteration can be increased above the domain length. This reduces the number of total iterations for a full length computation significantly. The effective nonlinearity is implemented in the build-in solver and the fourth order Runge Kutta, and not the first order solver, that is only used if the poling structure cannot be assumed perfect.

2.1.1.3 Gaussian Beam Considerations

The parametric processes treated in this thesis describe the interaction in between laser beams operating in close estimations of the fundamental mode. From the assumptions in section 2.1.1 the plane wave approximation is valid

for a confocal parameter, or Rayleigh range, larger than the crystal length, i.e. the wave vectors are required to be collinear over the crystal length to be phasematched. In section 2.1.1.1 it was derived that the conversion efficiency is proportional to the intensity. To maximize the QE without violating the plane wave approximation the optimal focus should intuitively be close to the point where the confocal parameter and the crystal length match. With fields of different wavelengths the overlap of the mixing and the signal field will depend on the focus as well and a more thorough analysis is required to obtain the exact relation.

The optimal relation between the confocal parameter and the length of a nonlinear crystal is derived by Boyd and Kleinman in 1968 [8] for a range of parametric processes. For SFG and DFG with non-critical phasematching and no walk-off, it turn out that the optimal size of the confocal parameter is one third of the crystal length and that the optimal conversion is achieved when the confocal parameter for all the interacting fields are equal. A reduction in efficiency resulting from Gaussian beam divergence will thus influence both the parametric and the overlap efficiency and in many experiments this is part of the explanation why the overall QE does not reach unity.

Simulations with a full field description is included in the master thesis by Anders Bilfeldt [42] and by Buchhave and Tidemand-Lichtenberg in [43], to describe how parametric conversion can couple energy between different spatial modes of the Gaussian beam. This is important for light sources that operates in the strong coupling regime and require control of the spatial output distribution.

2.2 Phasematching

The phasematch concept is one of the most essential concepts when designing parametric systems. It is required to obtain efficient conversion and depends on several physical parameters. The phasematch dependent term for the efficiency is stated in equation 2.8 and depends on the crystal temperature, the specific wavelengths, and the angles of the interacting fields. From the sinc-function this can be translated to a bandwidth for each of the three parameters. This is displayed in figure 2.2, where the general case for the ΔkL-dependency is displayed together with wave vector diagrams of the non-phasematched process in both the colinear and non-colinear case. The full width half maximum (FWHM), included in the plot, is the general phasematch acceptance. Specific plots and computations as a function of the temperature or the wavelength can be made using the Sellmeier equations for the refractive indices. In the case of non-collinear phasematching, the FWHM of the angle acceptance can be estimated analytically. Following the vector diagrams in figure 2.2, the non-collinear mixing is introduced as the projections of the k-vectors onto the collinear direction and equation 2.7 transform to

$$\Delta k = k_3 - k_2 \cos(\theta_2) - k_1 \cos(\theta_1) \tag{2.14}$$

where

$$\theta_2 = \arcsin\left(\frac{k_1}{k_2}\sin(\theta_1)\right) \approx \frac{k_1}{k_2}\theta_1, \quad \text{for} \quad \theta_1 \ll 1 \tag{2.15}$$

and for small angles, equation 2.14 can further be Taylor expanded to second order as

$$\Delta k \approx k_3 - k_2\left[1 - \frac{1}{2}\left(\frac{k_1}{k_2}\theta_1\right)^2\right] - k_1\left(1 - \frac{\theta_1^2}{2}\right) \tag{2.16}$$

If $\delta\Delta k$ denote the difference between the collinear and non-collinear expression, i.e. equation 2.14 subtracted equation 2.7 the collinear terms are eliminated. A simple expression for the angle dependent phasematch bandwidth can then be derived as

$$\delta\Delta k = \Delta k_\theta - \Delta k_{\text{collinear}} = \pm\frac{1}{2}\theta_1^2\left(\frac{k_1^2}{k_2} + k_1\right) \tag{2.17}$$

which is valid only within the center lobe of the sinc-function. The general FWHM for a normalized sinc-function squared is 0.443. In combination with equation 2.17 the specific FWHM, with respect to the internal acceptance angle can be estimated as

$$\text{FWHM}_{\theta_1} = 2\sqrt{4\pi \cdot \frac{0.443}{L}\left(\frac{k_1^2}{k_2} + k_1\right)^{-1}} \tag{2.18}$$

which is still dependent on crystal length, and both wavelength and temperature through the refractive through the specific k-values. To get FWHM_{θ_1} in terms of the external acceptance angle the expression should be corrected by the interface relation between the refractive indices.

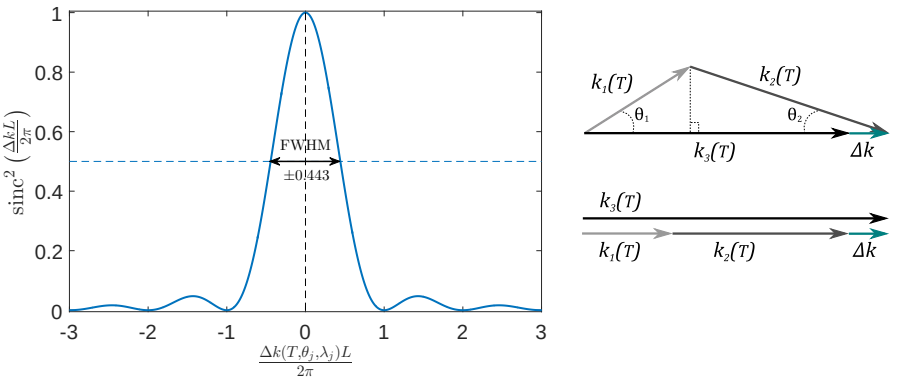

Figure 2.2: Left: Plot of the normalized sinc-function. Right: Wave vector diagrams of a collinear and a non-collinear parametric process with a phasematch discrepancy on Δk.

The specific term phasematching is formally defined as the matching of the wavevectors or the impulse of the photons in the parametric process, but physically the term covers the fact that three different wavelengths are in phase

throughout the nonlinear crystal. Not directly, but through the material interaction. Each of the fields are in phase with a oscillation of the electronic cloud in the material and the specific phase difference from the parametric interaction in each step, match the required phase delay in the next step. If this continues throughout the crystal each of the propagating fields will interfere constructively with each of the generated fields and result in a coherent summation of each of the interacting fields. When this happens the process is said to be phasematched. From this perspective the energy always flow between the fields in case of high intensities or high nonlinearities, but it is only in cases of phase matching that the fields build up and result in a generated signal at the end of the crystal.
In the case where the process is not phasematched the fields add constructively within the half a coherence length of the process defined as

$$l_{coh} = \frac{2\pi}{\Delta k} \tag{2.19}$$

and after half this length the propagating field will interfere destructively with the generated fields, and after a full coherence length the field will be back to zero. In this case the output will vary from maximum to minimum depending on the exact crystal length. In practical situations the field build-up over half a coherence length is negligible and the typical crystal is many hundreds or even thousands of coherence lengths long. If the process is closer to phasematch the coherence length increase and the destructive interference occur later in the crystal giving field oscillations with both larger periods and amplitude. Examples of perfect phasematching, partly phasematching and zero phasematching are displayed in figure 2.3 as a function of half the coherence length or $\Lambda/2$ for a specific parametric process.

2.2.1 Quasi-phasematching

When designing a nonlinear parametric system, it is often desired to propagate along the crystal direction that has the highest nonlinear coefficient while avoiding walk-off. That is propagation off all the interacting fields along the same axis in a birefringent crystal, also called non-critical phasematching. This is typically only possible at very specific wavelengths and temperatures for a given crystal. If the parametric process should be applied for the conversion of application specific wavelengths it is necessary to include a parameter that can engineer the phasematch condition. This can be done by quasi-phase matching, where the length of a poling period is introduced as a tunable parameter. The poling period, Λ, describes a set of two domains with opposite sign of the nonlinearity as illustrated in the inset in figure 2.3.
Field build-up in a quasi-phasematched (QPM) process is fundamentally different from classic phasesmatching, where the mutual material response difference (phasemismatch) is synchronized continuously to generate a coherent field build-up. In the QPM process it is a discrete correction of the accumulated phasemismatch that allow a coherent field build-up. This discrete correction

occurs if the sign of the crystal polarization is inverted at the exact position, where the accumulated phase difference would otherwise result in back conversion of energy, corresponding to half a coherence length of a given parametric process. This is illustrated in figure 2.3, where the field build-up is computed as a function of the crystal length, given in discrete steps of half the coherence length i.e. the domains of the 1D lattice defined by the sign inversion for the crystal polarization.

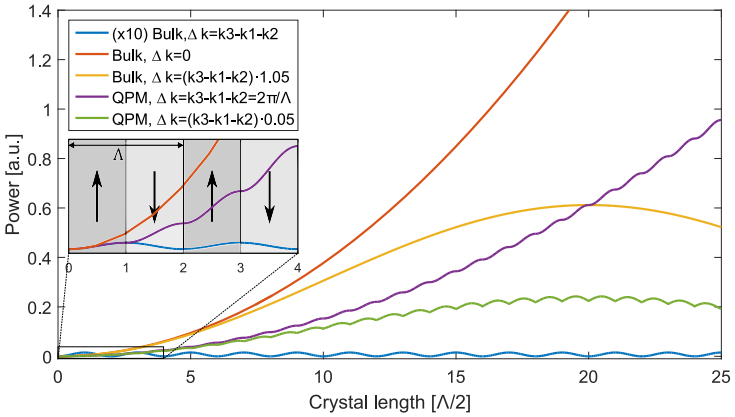

Figure 2.3: Computation of the field build-up as a function of crystal length given in discrete steps of half a coherence length for a specific parametric process. Three examples of classic phasematching and two with QPM are included to show how the energy flow evolve depending on the mutual phase delay of the fields. A typical crystal would include hundreds or thousands of coherence lengths and the small segment is chosen to illustrate how the classic phase match procedure build-up continuously and that the QPM build-up step-by-step match the discrete correction of the continuously accumulated phasemismatch. Inset show details on the relation between the QPM process and the periodic poling.

When $l_{coh} = \Lambda$ the inversion boundaries of the crystal polarization will match with the positions of parametric energy flow inversion, and the most efficient field build-up is achieved. Compared to the classic phasematch procedure the QPM efficiency is reduced by a factor of $2/\pi$ [41], but it allow for direct control of the phasematched wavelengths through the period of the polarization inversion. In this work a parametric process is defined as phasematched even though it is only quasi phasematched, and the polarization inversion will be referred to by the typical term periodic poling. Formally, the QPM can be introduced to the momentum conservation equation 2.7 following the typical crystal theory approach, that crystals or lattices have a pseudo-momentum or crystal momentum. The momentum conservation mismatch or phasemismatch in the case of a 1D poling structure is then

$$\Delta k = k_3 - k_2 - k_1 \pm \frac{2\pi}{\Lambda} = k_3 - k_2 - k_1 \pm k_{qpm} \tag{2.20}$$

where the plus/minus sign describes how the crystal momentum can represent both a positive or negative correction of the mutual phase delay for the parametric process. With k_{qpm} included, the QPM process can be treated exactly like the classic phasematch procedure with a reduced efficiency, and in the case where $\Delta k \neq 0$ the energy flow will behave similarly with an efficient coherence length defined by the new Δk-value. This is illustrated in figure 2.3 with a 5% deviation from optimum both for a QPM (green curve) and a bulk case (yellow curve). A description of the poling structure in the k-space is included in the next section, and the practical details on the production of crystals with periodic poled structures is treated in section 2.3.

2.2.2 K-space Approach to Phasematching

An alternative approach to describe the quasi-phasematching procedure is the k-space or Fourie transform approach, e.g. described by Somekh et al. in 1972 [44] and Fejer et al. in 1992 [41]. With this method, the cumbersome slab-by-slab approach presented in the previous subsection is replaced by a Fourie transform of the whole grating, giving a quick overview of the phasematch properties in a single operation.
Being a phase sensitive process the quasi-phasematching is defined from the relation between the wavevectors or k-vectors. The Fourie transform of the grating describes the distribution of spatial frequencies, and thus the phase response. If the main resonant peak, i.e. the first spatial harmonic, matches the $\Delta k-$value of a given process, the crystal supports first order quasi-phasematch. Other non-resonant frequencies display no significant response for a perfect grating, but with random duty cycle (RDC) errors, a response floor several orders of magnitude higher appears. See figure 2.4 for an example of a FFT of a perfect grating and one simulated with a 12% RDC-error.

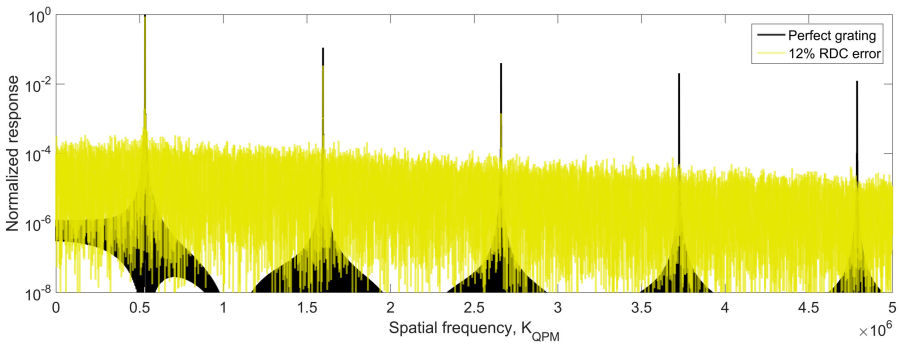

Figure 2.4: Fast Fourie transform of a perfect grating structure and one with a 12 % random duty cycle error. The y-axis is normalized to 1 for the perfect grating and represents the response of the poled grating for a given spatial frequency. The spatial frequency for the first resonant peak equals the phasemismatch or Δk-value in case of a phasematched parametric process

Following same general approach as [41] this section will show how the nonlinear conversion efficiency are related with the Fourie transform of a poled grating. Assuming no depletion of the mixing field and low conversion efficiency, i.e. low QE, the three coupled equations 2.3-2.5 reduce to

$$\frac{da_{\mathrm{VIS}}}{dz} = -iga_{\mathrm{MIX}}a_{\mathrm{NIR}}\exp(idkz) \tag{2.21}$$

with the solution

$$a_{\mathrm{VIS}} = -ig'a_{\mathrm{mix}}a_{\mathrm{NIR}}\int_0^L dzd(z)\exp(idkz), \quad g' = \frac{g(z)}{d(z)} \tag{2.22}$$

where the integral is recognized as the Fourie transform, except for the finite boundaries. It is normalized and for a perfect grating as

$$\int_0^L dzd(z)\exp(idkz) = d_{eff,ideal}L \tag{2.23}$$

where $d_{eff,ideal}$ is the effective nonlinearity for a perfect grating. The grating with errors, $d'(z)$, is included as

$$d'(z) = \frac{d(z)}{d_{eff,ideal}} \tag{2.24}$$

The reduction of the efficiency from the grating errors is convenient to write as a normalized scaling factor for the efficiency with respect to the perfect grating case. The transformation is convenient to work with as a normalized fast Fourie transform, $\overline{\mathrm{FFT}}$, and together with the scaling factor the expression for the photon flux becomes

$$a_{\mathrm{VIS}} = -ig'a_{\mathrm{mix}}a_{\mathrm{NIR}}Ld_{eff,ideal}\overline{\mathrm{FFT}}(d'(z)) \tag{2.25}$$

Converted to intensity the expression translates to

$$I_{\mathrm{VIS}} = \frac{2\omega_{\mathrm{VIS}}^2\epsilon_0^{\frac{1}{2}}\mu_0^{\frac{3}{2}}}{n_{\mathrm{VIS}}n_{\mathrm{mix}}n_{\mathrm{NIR}}}d_{eff,ideal}^2L^2I_{\mathrm{mix}}I_{\mathrm{NIR}}\left|\overline{\mathrm{FFT}}(d'(z))\right|^2 \tag{2.26}$$

$$\Rightarrow \ \eta_{\mathrm{NIR}\to\mathrm{VIS}} \propto \left|\overline{\mathrm{FFT}}(d'(z))\right|^2 \tag{2.27}$$

which demonstrates how the FFT of a normalized grating structure can give an overview of the conversion efficiency for the given crystal. For a more thorough derivation of the transform theory refer to [41].
With respect to the practical efficiency for a parametric process defined in equation 2.10, the FFT of the grating only describes $\eta_{\Delta k}$ and only with respect to a specific perfect grating. However, to get an overview of the performance of a specific grating and to explain the upconverted SPDC noise, it is a useful tool.

2.3 Periodically Poled Lithium Niobate

PPLN crystals with a 5% MgO doping supplied from Covesion Ltd. is used for the parametric processes described in this thesis. The MgO doping is included to reduce the photorefractive effect [45] and thereby increase the power stability for the parametric processes. Each of the crystals are custom poled in 5 different 1 mm x 1 mm channels, and four different sets of crystals are available, ranging from 11.8 µm to 31.59 µm in irregular steps. In appendix B all the periods are included and an example of a crystal datasheet.
The crystals is anti-reflective coated to reduce the loss with intra-cavity use, and lengths of 10 mm, 20 mm and 40 mm are used. Lithium niobate have been chosen due to the high nonlinearity on 25 pm/V (effectively 14 pm/V for QPM), good availability, a temperature dependent refractive index that allow for phasematch tuning, low absorption in the visible, NIR and MIR regime, good thermal properties, and a high intensity damage threshold. Details on the PPLN crystals are found in the support material at the Covesion guide to PPLN [46] and in the review paper by Arizmendi [45].

2.3.1 Poling Procedure

The poling procedure for lithium niobate crystal is described in [47] and the four main production steps are depicted in figure 2.5. Each domain in the poled structure is defined by a volume, where the polarization of the electronic cloud dipoles around the atoms in the crystal lattice is reversed, compared to the neighboring domain. This is possible because the lithium niobate crystal is a ferroelectric material, where a stable dipole inversion can be induced using high voltage.
In figure 2.5, it is described how the poling pattern is transferred to the crystal by photolithography, and how the high voltage field from the patterned electrodes induce a polarization reversal. Both the photolithography and the domain inversion can cause stochastic errors on the domain positions, described in the next section.
The nature of the domain reversal limits the thickness and the lateral dimensions possible for poled structures. If the domain structures is too small or the voltage too high the current will spark through the crystal across several periods, and if the crystal is too thick the voltage may not be high enough for a complete domain reversal. In standard commercially available crystals the poling period go down to approximately 5 µm with a channel thickness on 1 mm, but Ishizuki et al. has demonstrated crystals with poled structure thicknesses >5 mm [48].

2.3.2 Types of Poling Errors

The periodic poling in a lithium niobate crystal is typically assumed to be a perfect grating with an exact poling period. In reality the poling structure that

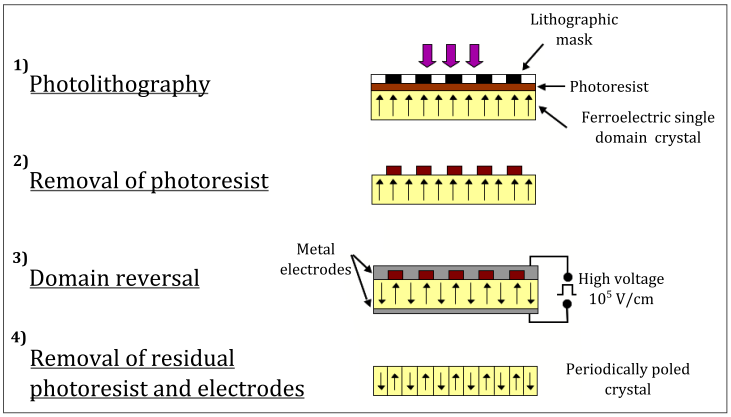

Figure 2.5: The four main productions steps in the poling procedure for the production of periodically poled nonlinear crystal for quasi phasematching. Reproduced from `https://fr.wikipedia.org/wiki/Oscillateur_param%C3%A9trique_optique`

defines the gratings are not perfect, and five of the possible errors is illustrated in figure 2.6 together with the case of a perfect grating. The theory of poling errors and the influence on second harmonic generation is described in great details by Fejer et al. [41].
The error type named random period error is only found in periodic crystals produced slab by slab either by bonding or growth. In this case, each layer will introduce a random error in the thickness and the error from each layer will accumulate throughout the crystal as a random walk. It is important to stress that the boundary position itself is strictly given by the grating period, but the error compared to the ideal grating evolves like a random walk, i.e. the crystal grow like random walk with a constant bias offset. As the interacting fields evolve through this grating, the synchronization with the phase of the light drift and the overall efficiency drops significantly. In the case with random duty cycle (RDC) errors, the overall efficiency drop is not as critical. In this case the grating/phase synchronization is retained throughout the crystal, and it is only within each domain pair that the conversion efficiency may be degraded. The RDC errors emerge in the lithography production method, where the production mask and the microstructured electrode itself may be assumed ideal. In the domain reversal process, it is the extent of the electric field that defines the domain boundaries, and this introduce a random error on the duty cycle within each domain pair, but it does not propagate along the crystal due to the strict control from the periodic electrodes.

If the production mask is not perfect, the error will propagate directly to the poling structure. Poling period offset and missing reversals are the cause of production mask and production mask transfer respectively. The poling period offset arises from the limitations in the tolerances for the production mask and will only cause an offset in the phasematch condition and not degradation in conversion efficiency. The offset is not a practical problem as the

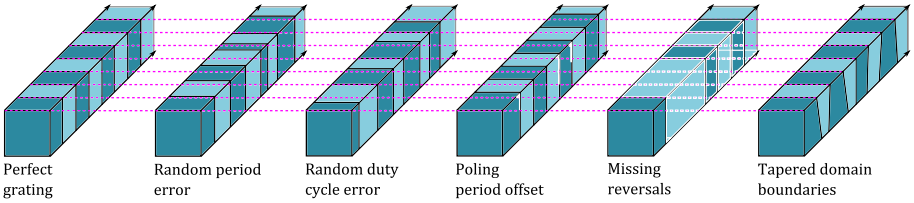

Figure 2.6: Five different examples of possible errors in the poling structure in nonlinear crystals. The first crystal are a reference with perfect poling and the typical poled crystal include several of the different error types at the same time. Only the first few periods out of many are illustrated.

phasematch is typically optimized with respect to temperature or angle. The missing reversals occur as the mask is transferred to the crystal surface through photolithography, and some of the domains are not etched all the way through to the crystal surface and thus still isolate when the electrode layer are added. Missing reversals inherently causes equal domain polarizations in sets of three and is thus not changing the overall phase synchronization. It will cause decreased conversion efficiency, but only take out few domain contributions out of thousands, and the effect may typically be ignored.
A general assumption in the crystal structures described above is that the top position of the domain boundary is retained throughout the full thickness of the crystal and that the poled crystal in that way can be considered as a 1D system. In reality the poled crystal is a 3D structure and errors can occur in all three dimensions. Surface plane errors, perpendicular to the grating, can be observed in the final crystals and may cause variations in the random duty cycle error across this dimension. In the depth of the crystal it is not possible to observe the final poling result, but as the boundary is defined by the electrical field some variation along this dimension is also expected. This is illustrated as a linear taper in figure 2.6 and may also cause variation in the random duty cycle error along this dimension.
A crystal may have RDC errors, poling period offset, missing reversals and tapered domain boundaries at the same time, but with high quality crystals none of this will affect the overall efficiency or phasematch conditions in setups based on parametric processes. The change in phasematch condition from the RDC errors will, however, influence the upconverted SPDC noise, being the main noise challenge for sensitive upconversion detection. The origin of the RDC error is inherent in the creation of the crystals and a discussion of a possible reduction is out of the scope for this work, but the magnitude and influence of the RDC errors is a key point in section 4.3.2 on the specificity of the noise.

CHAPTER 3

Light Source Configuration

This chapter describes the work on downconversion based light sources. It started as a continuation of the work with a CW tunable mid-IR lightsource, presented in [49]. The next step was to make a pulsed version and investigate its use for long range gas spectroscopy. The first section describes the design of the parametric module used throughout the thesis.
The next section describes the construction of a mid-IR optical parametric generator (OPG) and characterize it in the temporal and the spectral regime. Third section investigates the OPG as an optical parametric amplifier (OPA), with two different input seeds, and the last section discuss the possibilities for long range spectroscopic applications.

3.1 Cavity Design of The Parametric Module

In an efficient parametric process a nonlinear crystal and a high intensity mixing laser field are required. For many applications this means mixing powers above 50 W and preferably in a TEM_{00} mode. To access such high laser powers efficiently and safely, the nonlinear crystal is placed inside a high finesse laser cavity, where the circulating field can be three orders of magnitude higher than the output field. A simple version of such a cavity was used as a frequency downconverter in the CW light source characterized by Høgstedt et al. [49]. From that specific design it was experienced that both the power and the spatial mode of the generated IR light was unstable. From the work presented in [24] the experience was that a mechanically compact and fully integrated cavity could be a high stability solution. It was thus decided to continue the mid-IR light source project by building a new compact and mechanically stable cavity specially designed to support efficient up- and downconversion of coherent infrared light. The requirements and implementations are presented in the following list and a sketch of the setup is displayed in figure 3.1.

High intensity mixing field The cavity was designed to have two beam waists. One inside the PPLN crystal on 48 µm and one on 170 µm inside the laser crystal. This in combination with high reflectivity mirrors and a 3 W diode pump made it possible to achieve mixing fields above 700 kW/cm^2. The finesse of the cavity is 393 with 16 surfaces for one

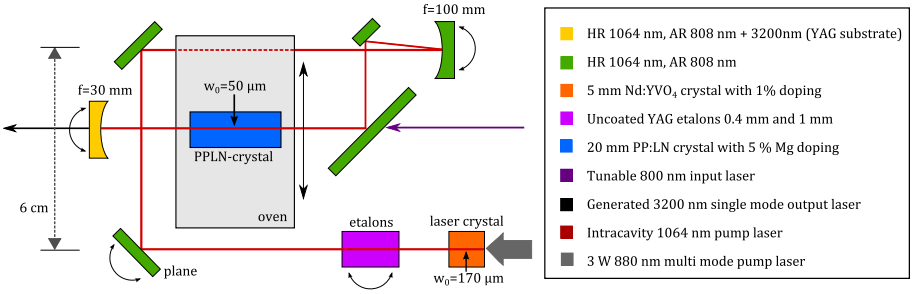

Figure 3.1: Design of the compact high finesse cavity designed for tunable high efficiency parametric conversion of coherent light. The laboratory setup is assembled on a custom made bottom plate with a matching protection lid. Coating syntax: AR: Anti-reflection coated and AR: High-reflection

round-trip and an average loss assumed to 0.1 % for all optical surfaces in the cavity. The mirrors are specified to higher reflectivities, and for perfect alignment of the 45°-mirrors the finesse could be higher.

Tunable phasematch condition The phasematch can be tuned by changing the poling period, the angle between the interacting fields or the temperature. The poling period and the temperature are adjusted by a motorized oven, that can shift between different poling periods inside the mixing laser beam while adjusting the temperature to match the specific wavelength configuration.

Mechanically stable design Based on previous experiences in the research group, it was known that a cavity with all components mounted on a single baseplate can give a stable system. For the first prototype the baseplate was 3D printed in ABS plastic together with a lid for dust protection.

Efficient coupling of signal In order to have the highest versatility of the system, the cavity is designed with small distances from the nonlinear crystal facets to the outside of the cavity. The last 45°-mirror before the PPLN crystal is a 1” mirror to allow for larger angle coupling.

Compact and suited for transportation The requirements on double beam-waists and tight focusing in the PPLN crystal entailed a long linear cavity. To make the system compact and suitable for transportation and application testing the cavity is designed as a linear cavity, folded around the PPLN crystal. The specific cavity design was performed using the commercial software Intarsia. An example of the cavity design is given in appendix C.

Single mode capability Due to spatial hole burning a cavity of this length will support a multitude of frequency modes within the gain spectrum. To achieve stable and efficient nonlinear interaction a narrow band mixing laser is preferred and to have that opportunity a mount for etalons is

incorporated in the cavity. It is positioned right after the laser crystal at the first beam waist in order to be within a plane wave approximation and such that the mount can hold a support-mirror for initial cavity alignment.

Symmetric beam profile in TEM_{00} If the mixing laser is operating in the fundamental Gaussian TEM_{00} mode, the parametric process is easiest to align efficiently and predict theoretically. This is achieved through careful alignment of the cavity, but the basis are given by a Gaussian stability close to zero and a cavity design that supports symmetric modes. The stability and ellipticity are optimized using Intarsia. To obtain symmetric modes the cavity should be designed with incident angles close to normal incidence on the curved mirrors. This in combination with the strict demand to stay within the tolerances for the reflectivity of the 45°-mirrors, limits the freedom for the cavity design.

The alignment procedure of the cavity is found in appendix D. In the process of designing the cavity it was decided to implement a 880 nm pump diode. This wavelength is more favourable for upconverted MIR signals that end up close to the typical pump wavelength at 808 nm. An extra advantage with the shift to a lower energy is a $\sim 5\,\%$ reduction in heat absorption in the laser crystal. With the whole cavity assembled, including the PPLN crystal, the laser power characteristics turned out as presented in figure 3.2. Due to thermal lensing in the crystals and local heating of the 880 nm pump diode the power dependency on pump power is not linear. The driving temperature is optimized with the diode running on maximum current and thus at maximum local heating. This will result in suboptimal temperatures at lower drive currents and a nonlinear behaviour of the curve as observed in figure 3.2.

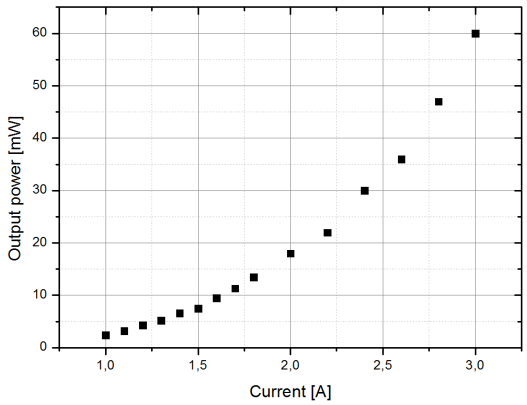

Figure 3.2: L-I characteristic of the parametric module cavity, measured by the leak from the f=30 mm mirror. Calibration show a ratio on 1:1187 between this leak and the intracavity field.

3.2 Design and Test of a MIR Optical Parametric Generator

An optical parametric generator was built as the first step towards the seeded mid-infrared optical parametric amplifier. The setup is included in figure 3.3 and the basic principles are the same as in the parametric conversion module. The key element is a nonlinear crystal, and to achieve maximum interaction the mixing intensity needs to be high. This is done with a pulsed laser in a single pass setup with a 40 mm long PPLN crystal. The poling structure is designed to match the DFG of the 1064 nm mixing laser and either a NIR or a MIR signal to generate the other. This is done with periods around 30 µm and the five exact periods are included in figure 3.3.
As pump laser, a passively Q-switched laser emitting at 1064 nm is used. The compact laser system are borrowed from an earlier project described in [50]. The typical average output power at 1064 nm is 300 mW and the pulse FHWM is 7 ns with a repetion rate of 5 kHz. This translates to a pulse energy of 60 µJ and a peak power of 8 kW. The mixing laser is focused to a beamwaist on 35 µm, measured with a pinhole placed at the PPLN crystal position. This gives a peak intensity in the PPLN crystal on 208 MW/cm^2 or more than 200 times higher than the intracavity mixing field in the parametric module in section 3.1. At these intensities, a powerful output is generated from the amplification of spontaneous parametric fluorescence alone, and the output is characterized both spectrally and temporally in the next two subsections.
The guiding mirrors and scaling optics in figure 3.3 are crucial for aligning and optimizing the OPG performance. The output from the Q-switched laser is down-scaled by a 4f configuration to increase the intensity inside the PPLN crystal, and the guiding mirrors ensure that the mixing field pass through the 1 mm×1 mm channel along the whole crystal length.

3.2.1 Temporal Pulse Distortion

To investigate the temporal pulse shape of the OPG output, the setup in figure 3.3 was applied. The depletion of the mixing laser pulse was recorded with a fast detector at position 1 and 2 to record a leak from the signal before and after the 40 mm PPLN crystal. No fast detector for the MIR signal was available and the parametric conversion module was applied as a upconversion module, shifting the MIR pulses down to the visible, where a SI-APD, at pos. 5, then recorded the pulse shape of the MIR OPG output. The result of these measurements are presented in figure 3.4, where the initial mixing pulse are plotted together with the residual mixing pulse and the upconverted MIR pulse for increasing levels of average mixing power.
All the measurements are representative single shot measurements, as the stability was not good enough to resolve the temporal variations with averaged measurements. The pulse measurements were trigged to the leak of the initial mixing pulse, and to avoid depletion in the upconversion module the peak power of the MIR signal was attenuated well below the depletion level. The

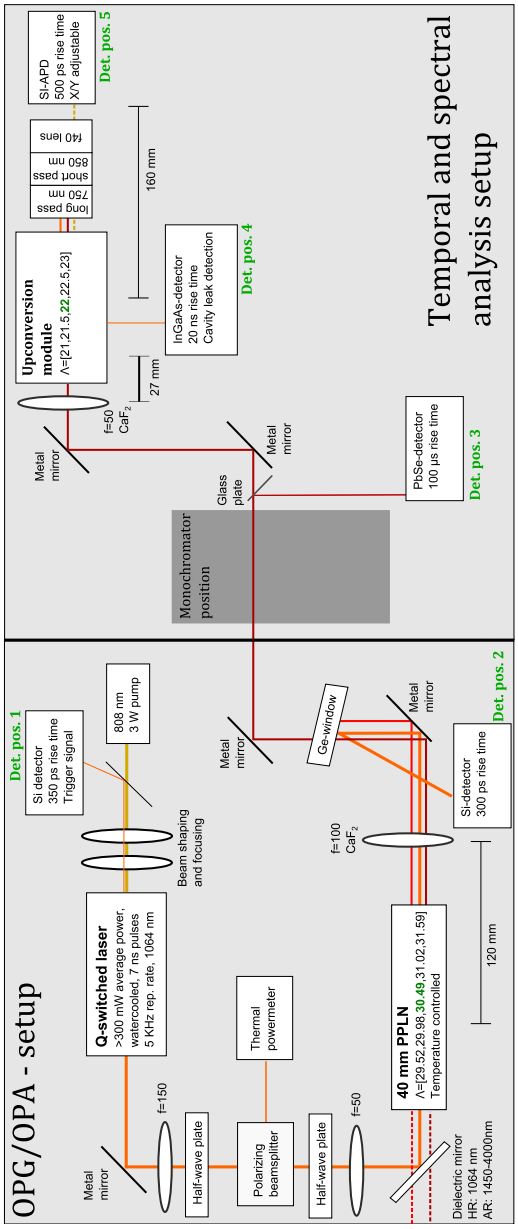

Figure 3.3: Combined setup of the optical parametric generator and amplifier together with the setup for spectral and temporal analysis. The monochromator is included for the spectral analysis measurements and the seed through the dielectric mirror in the lower left corner is applied for the OPA measurements.

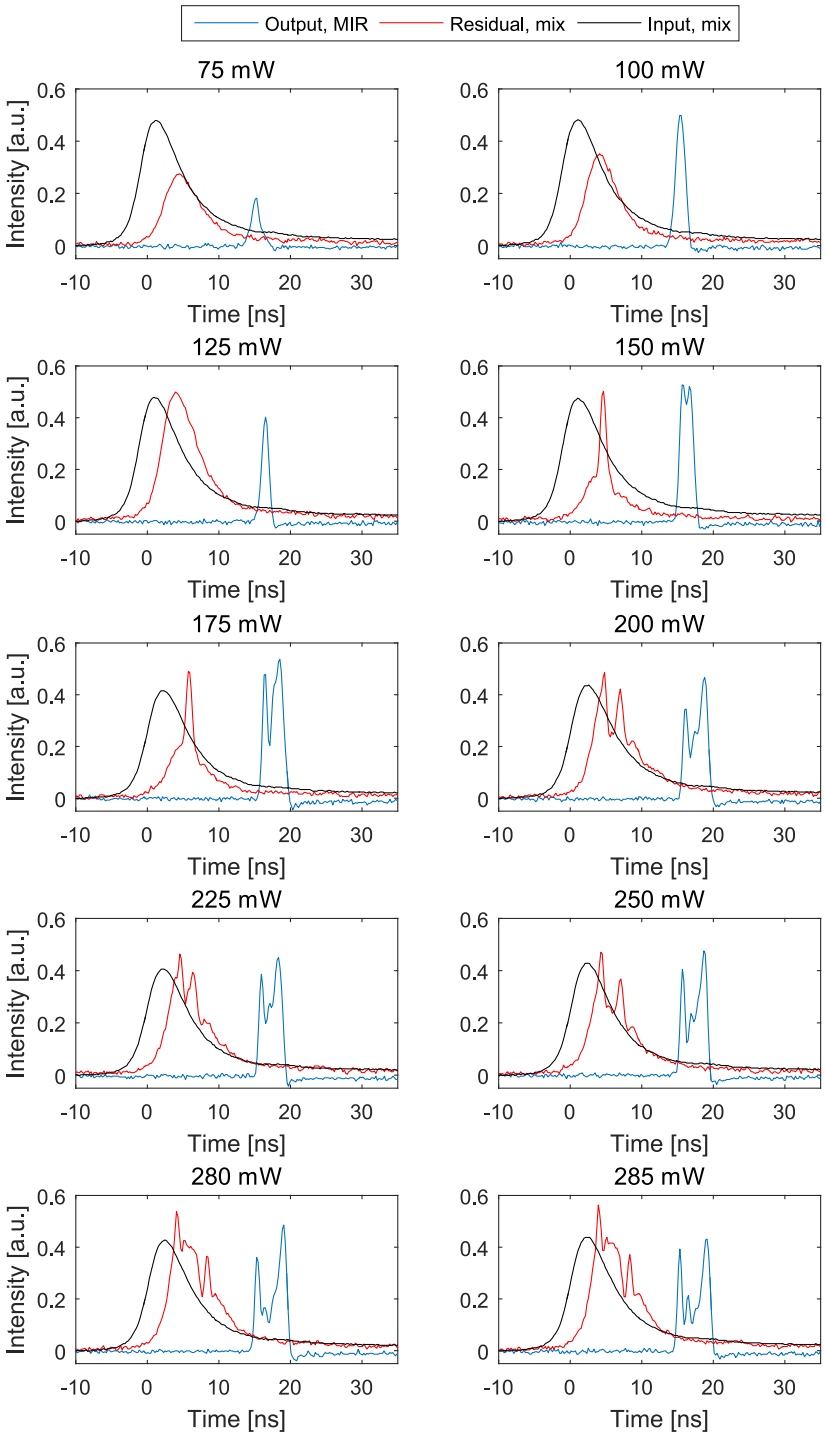

Figure 3.4: Measurements of the OPG mixing laser pulse before (*black*) and after (*red*) the PPLN crystal together with the upconverted MIR pulse (*blue*) generated in the OPG process. The measurements are triggered to the input mixing pulse and recorded as representative single shots due to power fluctuations.

challenge with high power upconversion detection is analysed in section 3.2.1.2 The average mixing power is varied with a halfwave-plate and recorded with a thermal power meter as displayed in figure 3.3. This ensures that the average power and the peak power remain at a constant ratio, given by the pulse length and the repetition rate. If the average power of the Q-switched laser was adjusted by the current for the 808 nm pump diode it would be the result of a change in both peak power and the repetition rate.

The first three of the ten plots in figure 3.4 display the pulses in the nondepleted regime. The next to be expected would be a dip in the center of the mixing pulse where the intensity is highest. This is not observed and it is not until the 200 mW frame, where the center of the peak is strongly depleted. Going to higher powers the center part of the mixing pulse is expected to backconvert and increase the power in the central part again. This tendency is seen towards the last frames and in the last three frames it is clear that both the mixing pulse and the output pulse become fragmented, and that the shape are influenced strongly by both depletion and backconversion. An overall tendency through all the frames for the MIR signal pulse is the pulse splitting that increase for increased mixing fields. This is explained by the nature of parametric generation. After the signal is amplified to the point, where the mixing laser is fully depleted, the back conversion set in and deplete the signal to near zero field value before it start to build up again. The conversion of power back and forth is periodical, but the strong interaction zones are separated by longer intermediate zones in the nondepletion regime. This mechanism delays the return of center part of the pulse as the mixing power increases and cause pulse splitting. A simulation of the periodic back and forth conversion is illustrated in figure 3.6 in the next section.
It is not simple to predict the temporal pulse shape without a full model including the spatial distribution of the pulse. The pulse deplete not over the full area at the temporal defined maximum, and not over the full pulse duration at the spatial defined maximum. These complications might be part of the reason, why the frames in figure 3.4 does not align completely with the expected behaviour. Another reason for the discrepancy could be the instability on the measurements, originating mainly from the pulse-to-pulse peak power fluctuations from the Q-switched laser. These fluctuations that translate into output fluctuations through the high, and mixing field dependent, gain. On a shorter timescale the stochastic nature of the vacuum fluctuations will cause further instabilities. Starting a parametric process with a stochastic seed in a high-gain medium, like a 40 mm PPLN crystal, give rise to a stochastic output with large power fluctuations. The fluctuations from the stochastic seed is expected to happen on a very fast time scale, given by the crystal material and it is expected to be averaged out by the detectors.

As a special feature in the OPG process, the pulse shape of the output is strongly defined by the gain throughout the crystal. The output power is built up from vacuum fluctuations, constant in space and time, but only amplified where a mixing field is present.
The intensity dependent gain tend compress a pulse both spatially and tem-

porally as it develops throughout the nonlinear crystal. Assuming a Gaussian distribution in both space and time and powers in the non-depleted regime it is possible to calculate the exact gain induced width of the generated MIR pulses. Equation 2.13 for the non-depleted optical parametric amplification can be approximated to

$$\begin{aligned} I_{\mathrm{MIR}}(L,0)\frac{1}{2} &= I_{\mathrm{MIR}}(0,0)\cosh^2\left(\frac{\gamma(t)L}{2}\right) \approx I_{\mathrm{MIR}}(0,0)\exp\left(\gamma(t)L\right)\frac{1}{4} \\ \gamma(t) &= \gamma(0)\sqrt{\exp\left(-t^2\frac{4\ln(2)}{\mathrm{FWHM}_{\mathrm{mix}}^2}\right)} \end{aligned} \tag{3.1}$$

assuming that $\gamma L \gg 1$ and that the intensity is Gaussian distributed both temporally and spatially. $\gamma(t,r)$ is the gain dependent on either the time or the radial position in the crystal, $I_{\mathrm{MIR}}(Z,0)$ is the photon flux density at a given crystal length in the crystal for the center of the power distribution in either time or space and L is the length of the crystal. After some rearrangements the following expression for the full width half maximum (FWHM) is reached

$$\mathrm{FWHM}_{\mathrm{MIR}} = \frac{\mathrm{FWHM}_{\mathrm{mix}}}{\sqrt{2}}\sqrt{-2\ln\left(1-\frac{\ln(2)}{\gamma(0)L}\right)} \tag{3.2}$$

where $\mathrm{FWHM}_{\mathrm{MIR}}$ is defined as the difference between the two temporal or radial values, where the intensity distribution for the generated MIR pulse has reached half its peak value. Similar to the expression obtained in [51], and by insertion of real life numbers corresponding to the measurements in the first three frames in figure 3.4, the FWHM values compare as 2.2 ns/1.3 ns, 2.1 ns/1.6 ns and 2.0 ns/1.1 ns for calculated and measured respectively. The discrepancy is expected as the result of the pulse to pulse fluctuations on the mixing laser and the uncertainty of the mixing field intensity defining the γ-value in equation 3.2.

Equation 3.2 is a general relation describing the width of the mixing field distribution in both the temporal and spatial regime. In the non-depleted regime, the beam waist of the generated signal is expected to focus at rate corresponding to the temporal compression.

In the depletion region, the gain induced shape distortion of the generated signal pulses will influence how the intensity of the fields evolves in time and space and add to the final shape as exemplified in the last frames of figure 3.4. A closer look on the shift between depletion and non-depletion is found in figure 3.5, where the average generated MIR power is plotted for varying average mixing power levels together with the peak level of the detected pulse. The pulse peak values are computed from the maximum value on average oscilloscope readings of 100 pulses translated to MIR peak power from the average power detected with a thermal power meter inserted directly after the OPG. This method gives rather crude estimations of the absolute peak power values, but the tendencies should be reliable. The average power rises for higher mixing fields without any drop off, translating to a non-stop increase in the total pulse energies. The peak power, however, experience a saturation at 200 mW average mixing power, corresponding to the start of the depletion region. The

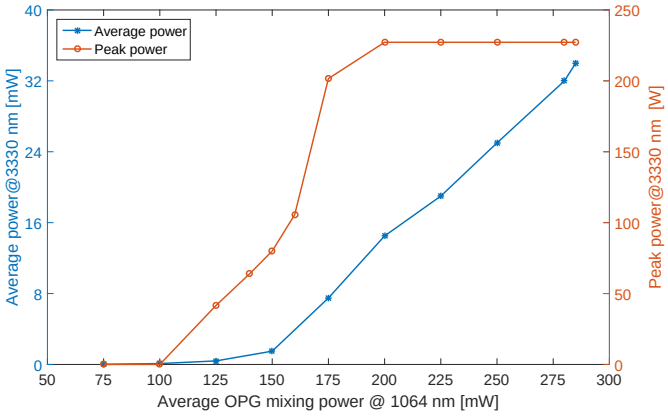

Figure 3.5: Measurements of the average OPG output power at the MIR wavelengths compared with the estimated pulse powers for a range of average powers for the OPG mixing laser. The average power measurements and the calculated pulse powers are not obtained simultaneously but for matching power levels.

flat peak level continues as other part of the pulse reaches the same saturation level for higher mixing powers. Comparing this with the corresponding pulse plots in figure 3.4, there is a discrepancy as the temporal pulse shapes indicate a transition to the depletion regime already around 150 mW. This indicates that the off-center parts of the pulse rise to higher levels than the center value, which is explained by the area distribution of power. There is, however, a shift in the slope for the average power at the 150 mW and after this point it remains constant. This correspond to a saturation of the pulse-to-pulse QE, indicating that there is two depletion regions, a temporal defined at 150 mW and a spatial defined at 200 mW.
Pump depletion in OPG's is observed experimentally in [52] and the theory on depletion in parametric processes are treated in [43] and [53]. For pulses in the nanosecond regime, all physical considerations assume a quasi-CW behavior, but for pulses in the ps-regime or faster, it is necessary to take the dispersion properties of the crystal into consideration. This will result in further pulse splitting as the different wavelengths run away from each other throughout the crystal. It is investigated numerically in [54] and [42].

3.2.1.1 Vacuum Fluctuations as OPA Seed

The distinction between an OPA and an OPG is defined by the presence of a seed, but as discussed earlier the OPG can be described as an OPA with a stochastic seed defined by the vacuum fluctuations existing at all times and all wavelengths. This seed is not directly measurable and contains no energy, it can however stimulate the parametric process that splits one high energy photon into two with lower energies. From the measurements of MIR output power, pulse width and input mixing power, it is possible to estimate how many photons per second the vacuum fluctuation seed correspond to. In the

non-depleted regime, e.g. frame 3, in figure 3.4 the gain can be calculated from the mixing power. When the gain and the output photon flux is known the corresponding input photon flux can be computed from equation 3.1 as

$$\phi_{\mathrm{MIR}}(0,0) = \phi_{\mathrm{MIR}}(L,0)\cosh\left(\frac{\gamma L}{2}\right)^{-2} \tag{3.3}$$

where $\phi_j = \frac{I_j}{\hbar\omega_j}$. The peak mixing power at an the average mixing power of 125 mW is 3.4 kW giving $\gamma L = 25$. The corresponding average MIR output is measured to 0.4 mW and with the pulse width from equation 3.2 this gives a peak power of 47 W. Following equation 3.3 this corresponds to an input field of $\phi_{\mathrm{MIR}}(0,0) = 1.1 \cdot 10^{20}\,\mathrm{photons/s/m^2}$ or 2 nW peak power if focused to a beam waist of 10 µm, scaled according to equation 3.2. This should be compared with the theoretical value, calculated from the number of vacuum states and the detected bandwidth of the output signal. A description of the theory and corresponding measurements are found in [55], where the spontaneous fluorescence background is investigated and quantified. Following their principles the vacuum fluctuation equivalent photon number is given as

$$\phi_{\mathrm{MIR},calc}(0,0) = 2\frac{n^3}{2\pi}\Delta\omega_{\mathrm{MIR}} = 1.6 \cdot 10^{22}\,\frac{\mathrm{photons}}{\mathrm{s}\cdot\mathrm{m}^2} \tag{3.4}$$

where $\Delta\omega_{\mathrm{MIR}}$ is computed from a measured spectral FWHM at 10 nm, section 3.3. A comparison of the calculated number of seed photons from the theory and from the measurements show a large discrepancy. In the paper by Homann and Riedle [55] the theoretical value corresponds very well with their measurements, indicating that the computation based on the measurements at hand might be too low. The major uncertainties associated with the calculation in equation 3.3 is the measurement of the MIR output power, done with a thermal power meter, and the pinhole measurement of the beam waist in the PPLN crystal. Furthermore the plane wave assumption is violated with a confocal parameter at 8 mm, and with a 10 order of magnitude gain small uncertainties translate to large changes in the calculate number of seed photons.
The calculated numbers may seem like a large input seed from vacuum fluctuations alone, but for a single pulse in the crystal the calculation from the measurement only corresponds to 53 photons and the theoretical value corresponds to $8{\cdot}10^3$photons.

With the mixing laser as the only input, it is possible to simulate the output power of the OPA system with the right amount of vacuum fluctuations as seed. This is done in figure 3.6 using a MIR seed on $1.6 \cdot 10^{20}\mathrm{photons/s/m^2}$. The simulations are built on the coupled equations presented in section 2.1.1 by using a build-in Matlab solver. It is clear to see how the parametric process change between the depleted and the non-depleted regime. For higher mixing or seed intensities, the periodic back and forth conversion pattern would be compressed and occur over a shorter crystal range.
From figure 3.4 in frame 285 mW, it would be expected that the MIR signal had been backconverted in figure 3.6. This discrepancy support the conclusion that the seed calculated from the measurements in equation 3.3 is too low.

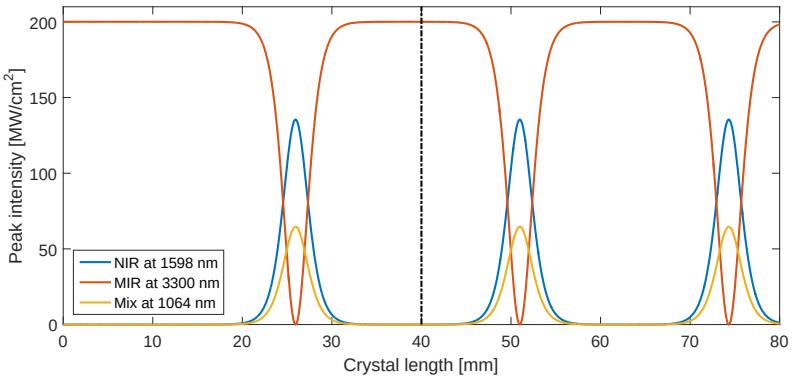

Figure 3.6: Simulation of the output peak power for the OPG with vacuum fluctuations applied as seed, 40 mm PPLN crystal, 35 µm beamwaist and a average mixing power at 285 mW converted to peak intensity. The simulation is done for intensities to account for the different sizes in beam waist for the different wavelengths.

3.2.1.2 Depletion in the Upconversion Process

It was mentioned in section 3.2.1 that the output from the OPG in the temporal analysis was attenuated to a level well below depletion in the upconversion module. The attenuation unit is not included in figure 3.3, but consist of a number of calibrated pieces of glass placed in the beam path from the OPG to the upconversion module. At the time of the measurements the upconversion cavity ran at an intracavity field level around 25 W and this defined the limit for the peak value of the incoming signal to be upconverted.
To investigate the possible depletion of the upconversion module, the attenuation of the MIR signal was removed and the intracavity field of the upconversion module was monitored for different currents for the pump diode in the intracavity mixing laser. The leak was tapped from the last reflection in the upconversion cavity, before the light returned to the gain medium, see figure 3.3 (det. pos. 4). The measurements of the relaxation oscillations are plotted in frame 1-11 in figure 3.7 together with the input mixing laser pulse for the OPG as trigger signal.

All the measurements experienced the same input signal with peak powers much higher than the intracavity field, and the depletion should thus be more or less the same in all the measurements. This is however not the case, and this variation could be a result of changes in mode structure or size upon mixing power variations. Only an incoming signal that extends over the whole mixing field at power levels higher than the intracavity field can display 100 % depletion. In this way the depletion only reflects the actual quantum efficiency in case of perfect overlap. The measurements show a maximum of 90 % depletion, indicating that the incoming laser beam might be focused a bit too hard, aligned off axis with the mixing laser or have a different spatial shape.
The relaxation oscillations are clearly observable in all the frames, and both the amplitude and the frequency rise for larger field intensities. The phenomenon is a consequence of the dynamics in the four level ND:YVO_4 laser crystal and oc-

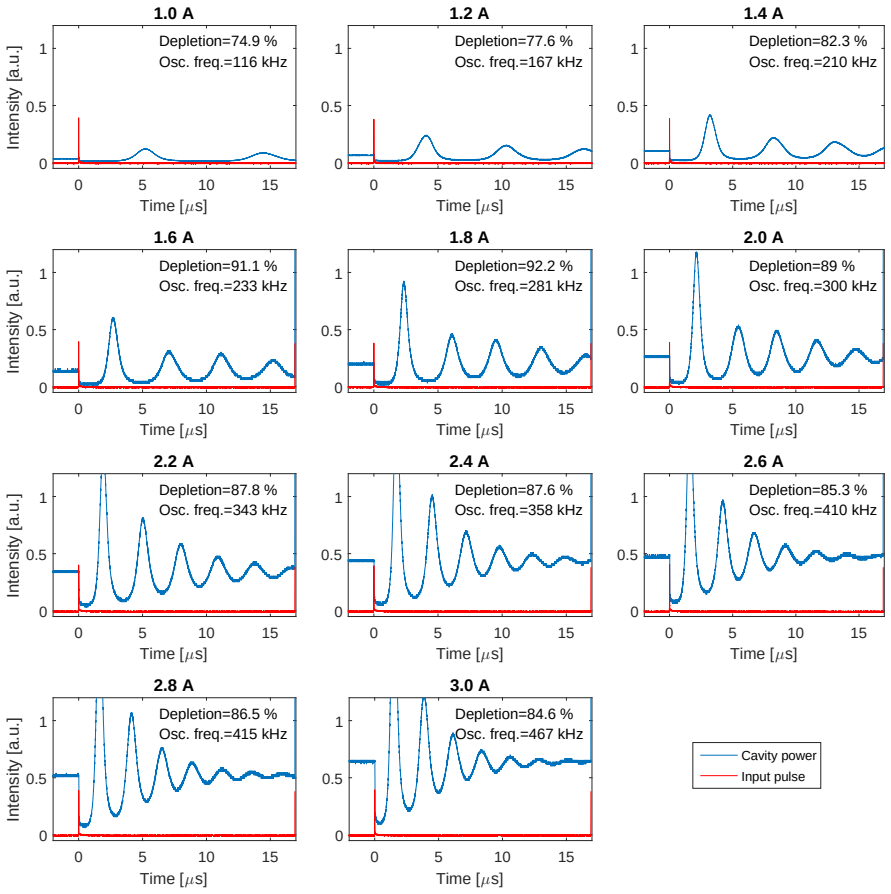

Figure 3.7: Measurements of the leak power from the laser cavity in the upconversion module showing relaxation oscillations as the field is depleted by the incoming MIR pulse. The relaxation frequency is found by an FFT analysis of the oscilloscope traces and the depletion level is computed from the first step in the cavity power.

curs when the incoming laser field depletes the intracavity field. This disturbs the balance in the energy level populations, and allow for an excess build-up in the upper state which causes an intracavity field higher than the steady-state value. This oscillating mechanism continues until the dampening of the cavity loss brings it back to steady state. As the pump field increases in the laser crystal the filling rate of the population follows, giving the observed magnification of the dynamic behavior. Similar results are often observed e.g. in [50] and a more rigorous and quantified treatment using rate equations is found in [56]. In an upcoversion module for detection the relaxation oscillations is obviously a problem. However the application is typically low power or even few photon detection with high intracavity fields, and in this case the issue with relaxation oscillations is not a problem.

3.2.2 Spectral Output Characteristics

The spectral content of the OPG output was measured with a Newport Cornerstone 130 1/8m implemented as sketched in figure 3.3. The monochromator output is transmitted to both the combined upconversion/SI-APD, pos. 5, and a conventional PbSe detector, pos. 3, measuring on a small reflection from an uncoated glass plate placed in the beam. The monochromator is configured with a 300 lines/mm grating and a minimum of 10 µm slit width. With an incoming beam diameter of 1 mm, the resolution of the monochromator output is computed to 0.2 nm at the MIR wavelengths. The data acquisition was automated such that the grating position of the monochromator was synchronized to the oscilloscope read from the two detectors. The monochromator swept with steps of 0.5 nm in the spectral response and each acquired oscilloscope read is an average of 10 sweeps. In the signal processing, the peak value of the oscilloscope traces was plotted as a function of the grating position, translated to the transmitted wavelength. Figure 3.8 (a-c) display the output data from the script for three different phasematch configurations of the combined OPG and upconversion setup. The choice of crystal temperatures and poling periods for the three center wavelengths are stated in table 3.1.

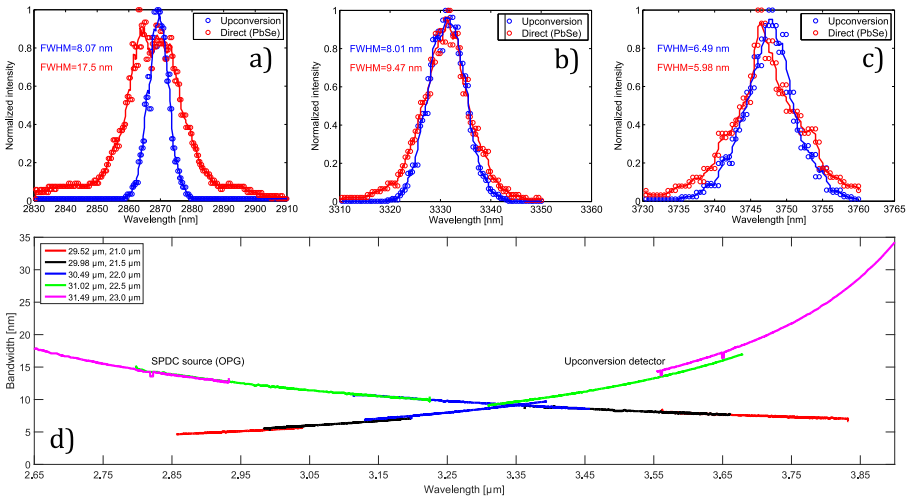

Figure 3.8: a),b),c) Monochromator measurement of OPG spectra for three phasematching conditions. The solid lines are a running average included to guide the eye. d) Computation of FWHM spectral bandwidth for the SPDC and upconversion process based on colinear phasematch condition and material dispersion properties. SPDC is computed for 40 mm PPLN crystal and upconversion for a 20 mm PPLN crystal.

From the measurements in figure 3.8, it is clear that the PbSe and the upconversion detection have different spectral response. Both the PbSe and the SI-APD can be assumed to have a flat spectral response in the applied region, meaning that the spectral limitation must originate from the phasematch constrains in the upconversion process. This is confirmed by the plot

Table 3.1: Phasematch configuration parameters

	SPDC		Upconversion	
λ_c [nm]	T [°C]	Λ [µm]	T [°C]	Λ [µm]
2870	157.4	31.02	33.8	21.00
3330	80.1	30.49	165.8	22.00
3748	57.3	29.52	98.4	23.00

(d) in figure 3.8 where the FWHM of the wavelength acceptance bandwidth is computed for both the SPDC and the upconversion process. The computation assumes colinear phasematch and follows the principles described in section 2.2. A comparison of the calculated and measured bandwidth displays an overall agreement with respect to the expected bandwidth of the two processes, and explains the differences in the recorded spectra. However, there are small discrepancies for the acceptance bandwidth. For the shortest center wavelength, a), the measured bandwidth is smaller than expected, for the middle wavelength, b), they are approximately the same, and for the longest wavelength, c), the measured bandwidth is somewhat smaller than expected.
Part of the discrepancy can be explained by general uncertainties in the measurements, due to pulse energy fluctuations from the Q-switched pump, but part of the explanation can be found in the angular spread of the generated light. The computation is done for plane waves and colinear phasematching. This tends to underestimate the actual bandwidth, if all angles are passed through the system. It can be assumed that the mixing laser for the OPG process is Gaussian, and the generated beam will thus also be Gaussian. The divergence angle of a Gaussian beam is proportional to the wavelength of the light, and this might explain why the underestimation is detected only at the shorter wavelengths.

An application for a broadband light source in the MIR range, like the OPG, could be single shot spectroscopy with an output covering the whole spectral band of interest. With a 10 nm PPLN crystal the bandwidth at 3 µm would increase to 50 nm, and the pulse-to-pulse instability could be solved by pulse power monitoring or with an active Q-switched laser.
Another advantage with a broad spectral output is the possibility to generate ultrashort pulses. This is demonstrated in [57] where a ≈800 nm broad output is demonstrated in 3-4 µm range. The full setup including two cascaded aperiodic PPLN crystals followed by a non-collinear pumped PPLN crystal generates 44 fs pulses with an energy of 21.8 µJ. Another approach to MIR broadband parametric light sources is demonstrated in [58] where a 5 W CW output is demonstrated with a spectral width from 3400-3500 nm. This is achieved in a single resonant oscillator and a broadband pump configured to a phasematch condition with low variation in Δk and thus broad acceptance bandwidth.

3.3 OPA Measurements

In this section the OPG is operated with an input seed and referred to as an OPA. With a pulsed mixing laser for the OPA, a CW seed is convenient to avoid timing issues. If the CW laser is single frequency and tunable then the output from the OPA will have the same characteristics. This is a convenient way of constructing a light source for long range gas spectroscopy as OPA's are simple high gain devices and the single frequency tunable lasers typically have low output powers. The work in this chapter was presented at the ASSL conference in Paris 2013 and summarized in [59]. The poster is included in appendix E.

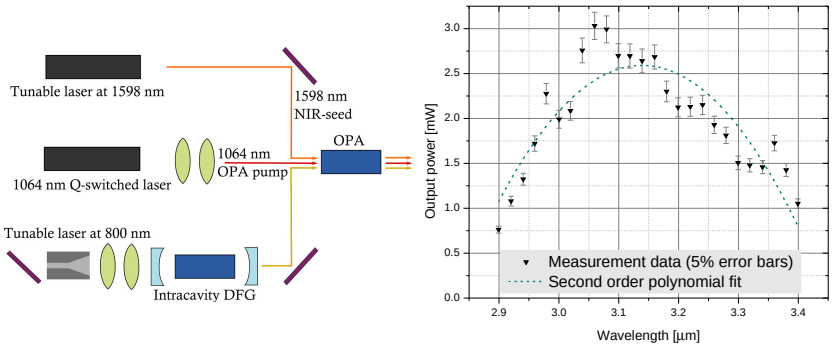

Figure 3.9: Left: Overview of the different seed configurations for the OPA. In the real setup the beam combining is done with a dielectric mirror and a flip mirror selecting either the NIR or the MIR seed. Right: Measurement of the single frequency output power from the tunable MIR seed. Reproduced from [49].

Figure 3.9, left, shows, conceptually, how the different laser setups are combined to a setup where the spectral influence of the NIR and the MIR seed can be investigated. The NIR light source is a commercial tunable laser (Ando AQ4321D). The OPA is described in section 3.2 and the CW MIR light source is described in [49], where the bread board setup has been replaced with the compact module described in section 3.1. An example of the CW MIR tuning is given in figure 3.9, right, and with the compact down-conversion setup output powers above 5 mW was achieved. This tuning range is transferred through the OPA process as the tuning curve for the pulsed MIR seeded light source. The beam combination is done with a dielectric mirror as displayed in figure 3.3.

In the combined setup three different output configurations was possible: Unseeded, NIR seeded or MIR seeded. Table 3.2 lists the different output powers at the corresponding wavelengths, and figure 3.10 presents the three different outputs in frame d-f and the corresponding mixing and seeds in frame a-c. All spectra are measured with an Ando AQ-6315E OSA and the calculated MIR spectrum is the convolution of the spectrum from the tunable 800 nm laser

and the paramteric module mixing laser. The wavelength axis was scaled following the energy conservation and the two spectra is found in the poster in appendix E.
With no seed the output spectrum from the OPA is broad, figure 3.10 e). With the NIR seed in d) the spectral characteristics from the seed are transferred to the output and with the MIR seed in f) it is the spectral characteristics from the mixing laser that are transferred to the output spectrum. This implies that there are two ways to obtain single frequency operation in the MIR regime. Either a single frequency seed can be combined with a multimode mixing laser as in the current setup, or a single frequency mixing laser can be combined with a single frequency NIR seed, thus giving single frequency operation in both the NIR and the MIR regime.

Table 3.2: Seed and OPA - Power levels

$\lambda_c = 3190\,\text{nm}$	
MIR seed only	1 mW
OPA mix only	22 mW
With NIR seed	27 mW
With MIR seed	25 mW
$\lambda_c = 1598\,\text{nm}$	
NIR seed only	0.1 mW
OPA mix only	55 mW
$\lambda_c = 1064\,\text{nm}$	
OPA mix only	370 mW

From table 3.2 the 1064 nm mixing laser and the seeded MIR output can be converted to pulse energies and from figure 3.4 it is clear that the OPA is in the depletion regime where the output pulse shape is distorted both spatially and temporally. It is thus only the overall pulse-to-pulse efficiency that can be computed. With a repetition rate at 5000 the pulse energies is $E_{1064} = 74\mu\text{J}$ for the mixing laser and $E_{3190} = 5\mu\text{J}$ for the output with MIR seed. This translates into a pulse-to-pulse quantum efficiency at 20 %. The power levels are measured with a thermal power meter and different filter configurations. The actual quantum efficiency might be different due to different transmission losses.
From figure 3.5 it was learned that the pulse-to-pulse QE was constant for average mixing powers above 150 mW, for a specific choice of pulse width, focus and crystal length. Further investigations are required to optimize the maximum QE, but it is limited inherently by the lower gain at the slopes of the mixing laser, and it is not possible to operate the OPA with 100 % pulse-to-pulse QE.

In an OPA with a mixing laser that can drive the generated signal pulse to the depletion regime from vacuum fluctuations alone, the power of the input seed only needs to be on a comparable level. Using the theoretical value from

section 3.2.1.1 this translates to 0.3 μW and even if the seed has to be ten times this value to be dominant, the CW MIR seed is still three orders of magnitude too high.
Comparing a MIR seed with the build-up from vacuum fluctuations, the MIR seed is single frequency, tunable, and stable in power, whereas the vacuum fluctuations provide a broad band stochastic input level. A MIR seed is thus crucial if the output from the OPA needs to be controlled, and the important

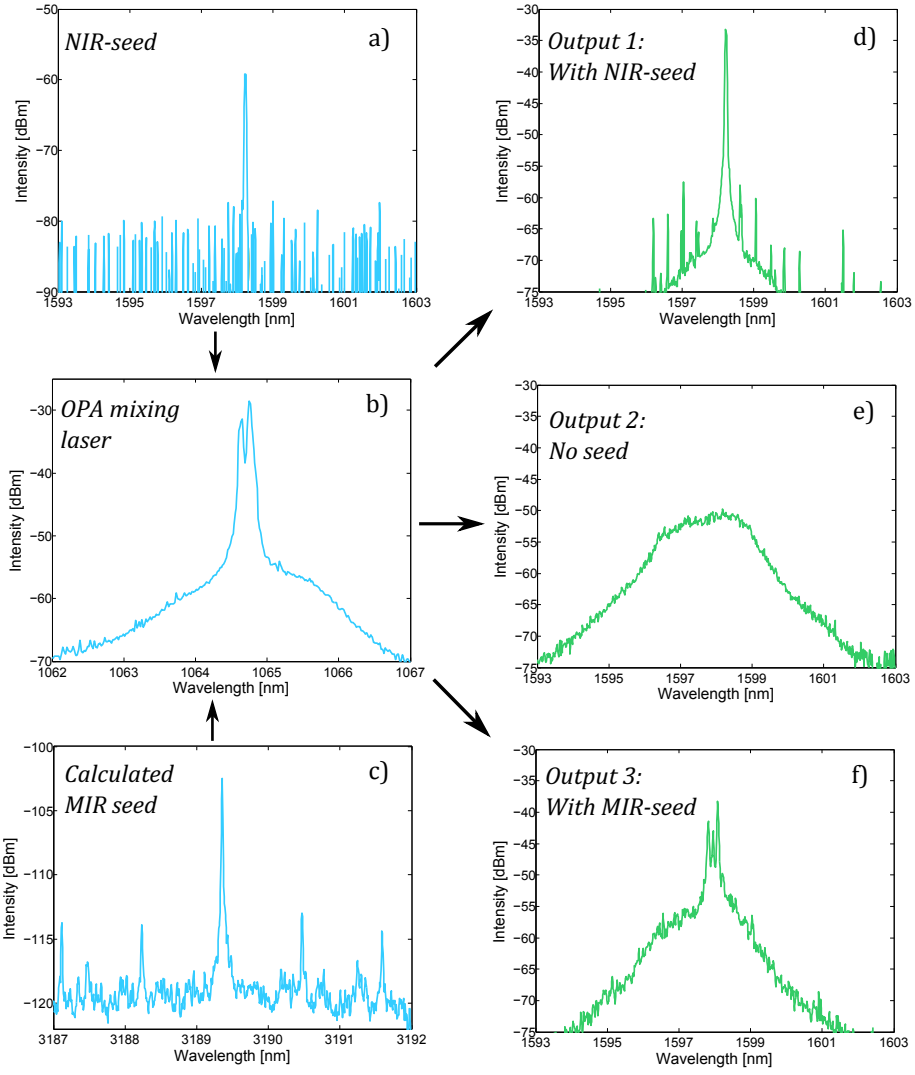

Figure 3.10: OSA measurements of the spectra for the OPA mixing laser b) and the NIR and MIR seed in a) and c) respectively. Frame d)-f) display the output from the different configurations of the OPA seed. The calculated MIR seed is the measured output spectrum from the tunable diode laser at 800 nm convoluted with the spectrum for mixing laser in the parametric module.

parameters are the spectral width and the tunability.
An analysis of the lower limit for OPA seeding based on the measured and simulated amount of vacuum fluctuations is given by Homann and Riedle in [55].

3.3.0.1 Pulse Duration with Seed

The pulse duration of the generated MIR output from an OPA is defined fundamentally different from the width of an OPG, computed in section 3.2. If the applied seed is much larger than the vacuum fluctuations, the output width in the temporal and the spatial regime is defined by the time and area where the seed and mixing field is confined, and not by the gain as in equation 3.2. The width of an OPA output can then be computed if the width of the input is known following the relation defined in [60]

$$\frac{1}{w_{\mathrm{mix}}^2} = \frac{1}{w_{\mathrm{NIR}}^2} + \frac{1}{w_{\mathrm{MIR}}^2} \tag{3.5}$$

$$\frac{1}{\mathrm{FWHM}_{\mathrm{mix}}^2} = \frac{1}{\mathrm{FWHM}_{\mathrm{NIR}}^2} + \frac{1}{\mathrm{FWHM}_{\mathrm{MIR}}^2} \tag{3.6}$$

and originate from the fact that the parametric process effectively act as a convolution of the involved fields.

3.4 Choice of Light Source Technology for Remote Detection

The overall goal for the light source part of this work was to investigate the construction of a light source suitable for long range gas detection. Such light sources need to be:

- Pulsed to do range gating and have sufficient power levels.
- High power, such that the amount of return photons from the usual low backscattering are enough for detection.
- Either emit single frequency on/off resonance for the specific absorption line or a broadband signal over the range of interest.
- Stable in both power and frequency to avoid confusion between system fluctuations and actual variations in concentration levels.

Semiconductor and parametric based technologies have the possibility of emission wavelength engineering from choice of design, materials and operating temperatures. The semiconductor technology is, at the present time, not developed to sufficiently high powers, at single mode and single frequency operation, and some sort of parametric process is typically involved in the high power spectroscopic light sources.
Based on the requirements for the ideal light source and the experimental results presented in this chapter, an OPG light source is not suitable for long

range gas detection as the spectral power fluctuates stochastically and both the temporal and spatial pulse shape is distorted for large output powers. The MIR-CW source used as a seed in section 3.3, is not suitable either, but in combination with an OPA it could be a viable solution. The problem with the MIR-CW source at hand is mostly that the tuning capability is limited by mode hops [49] and a minor issue is the over dimensioned output power. Another viable approach could be to use a single frequency tunable NIR light source together with a single frequency mixing laser.
Taking all the details above into consideration, a recommendation for a possible solution would be to use an OPA, similar to the one described in 3.3 in combination with a single frequency tunable quantum cascade MIR laser. This would reduce the complexity by removing the downconversion unit and even though semiconductor lasers are still hard to get in the MIR region some commercial products are available, e.g. TLS-41000-MHF from Daylight Solutions. The Q-switched laser should be upgraded with a more powerful pump to give higher pump powers for the OPA and allow for a larger amplification within the non-depletion region, that is preferred for long range operation. With DIAL measurements there would be a challenge with the pulse-to-pulse stability in the passive Q-switched mixing laser. This can possibly by circumvented by pulse-to-pulse calibration and the stability can potentially be optimized down to a few percent root-mean-square for both the amplitude and the width variation [61].
A conceptual sketch of the a possible long range spectroscopic setup is given in figure 3.11. The selection of quantum cascade lasers are larger at longer wavelengths and the concept could be extended to reach the long wave infrared region by changing to an $AgGaS_2$ based OPA pumped by a Q-switched Tm:YLF laser at 1.9 µm. This would open for long range detection of explosives or other compounds with spectral features in the long wave infrared region.

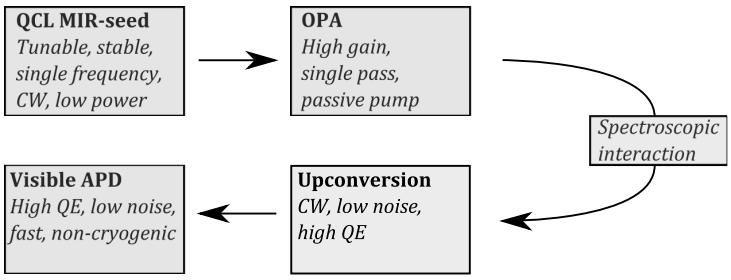

Figure 3.11: Possible setup for a long range gas spectroscopy system based on parametric technologies.

CHAPTER 4

Detector Configuration

This chapter describes the part of the project targeted the use of parametric processes for detection purposes. Sum frequency generation is applied to upconvert incoming infrared photons to the visible regime where highly efficient low noise detectors exist. The goal was a high QE and low noise conversion process for coherent point detection of collinear signals. Changing the parametric module to detector configuration is only a question of changing the applied context. The module itself is inherently configured to support both DFG and SFG from the energy relations and the phasematch conditions, described in section 2.1. It is a mere question of which fields that are present and if all three fields are present it is a question of the mutual phase relationship.

This chapter describes how a second version of the parametric conversion module was designed and how the module is specified in a detector context. A major part of the chapter will describe the noise properties of the upconversion process, and how the process that should be essentially noise free turned out as a major noise challenge. This is investigated through simulations and measurements. In the last part of the chapter it is presented how to optimize a detector module with respect to signal-to-noise ratio (SNR). Either by optimizing the mixing field intensity, choosing the right crystal or circumvent the noise more fundamentally through long wavelength mixing.

4.1 Upconversion Module as Detector

Using an upconversion module for detection purposes induces some constraints for the detector system. The following paragraphs give an overview of the possibilities and limitations defined by the nonlinear process.

Angle The angles accepted by the phasematch conditions for the upconversion process is limited by the length of the crystal, and the specific temperature, and wavelength. Through the whole chapter, the process will be assumed collinear unless stated otherwise, and the non-collinear case will be treated in the application chapter, 5.

Power For small signal detection, the incoming signal is much lower than the intracavity mixing field, and the upconversion module will operate within the non-depleted regime. The upconversion process will, however, get close to 100 % in quantum efficiency and it will be necessary to treat the signal in the strong coupling regime described in section 2.1.1.1. The signal may thus experience backconversion for high mixing field intensities, following the sinusoidal pattern defined in equation 2.12. At high quantum efficiencies, the power efficiency can go above 100 %, as a result of the energy added by the mixing laser, and following the energy relation for the process.

Wavelength Upconversion based detector systems differ from most other detectors by the parameter dependent spectral response. It is governed by the phasematch condition through the wavelength dependent refractive index, and can be controlled by the temperature or the poling period. If all poling periods and/or temperatures are available, all wavelengths within the transparency window for the nonlinear crystal can be reached. The range of poling periods is limited by the available crystals, and for the upconversion process two set of five poling periods are used in our systems. One for NIR detection, ranging from 11.8 µm to 15.8 µm in 1 µm steps, and one for MIR detection, ranging from 21 µm to 23 µm with 0.5 µm steps. An overwiev of the phasematch availability and the corresponding spectral bandwidth for the upconversion process are computed in figure 4.1 and 4.2 for the NIR and MIR wavelength region respectively.

Temperature As the other dependent parameter for the refractive index, the wavelength and temperature dependency are intertwined. For a given poling period and mixing wavelength, the temperature and signal wavelength form unique pairs. Theoretically, each temperature correspond to a pair of phasematched wavelengths following from the general phasematch relation stated in section 2.1. For most situations the long wavelength phasematch will be situated outside the transparency of the crystal, but an exception is found in figure 4.2 for the longest poling period. A more practical concern for the temperature parameter is a general recommendation to stay below 200°C to avoid damage of the crystal coatings, and above room temperature to avoid condensation.

Figure 4.1 and 4.2 display to the left a map of the phasematch dependent efficiency for the upconversion process as a function of both wavelength and temperature. The index values is the squared sinc term in the QE-expression, equation 2.8, and range from 0 to 1. Each line represents a specific poling period in the nonlinear crystal, with the shortest at the top in both cases. In between the lines the QE is around five orders of magnitude lower and unusable for detection. In the right, of the overview plots, the FWHM of each acceptance line are computed and plotted with respect to the signal wavelength. The few outliers on the graphs represent numerical errors in the FWHM computation and physically the change in acceptance bandwith are smooth and continuous.The squared sinc behavior is recognized on the insets, that display zoom

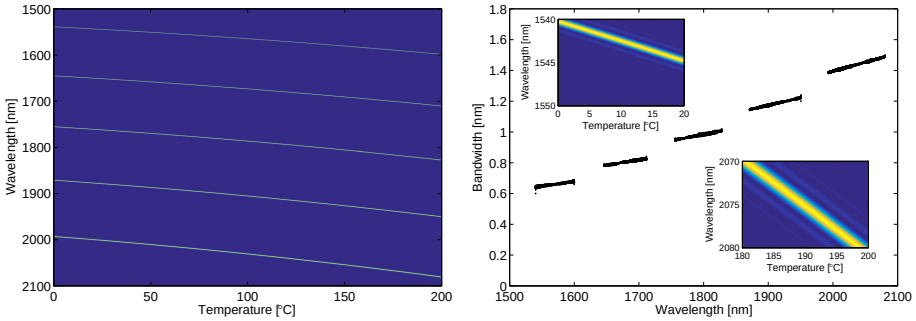

Figure 4.1: Left: Map of the phasematch dependent efficiency for the upconversion process as a function of both wavelength and temperature. Each line represents a specific poling period ranging from 11.8 µm in the top to 15.8 µm in bottom with 1 µm step. Right: FWHM for the wavelength of the acceptance curves in the left plot as a function specific wavelength. The two insets show selected zoom windows of the left plot.

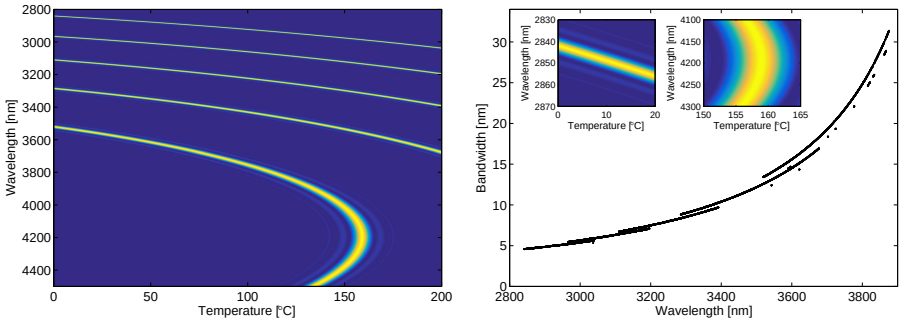

Figure 4.2: Left: Map of the phasematch dependent efficiency for the upconversion process as a function of both wavelength and temperature. Each line represents a specific poling period ranging from 21 µm in the top to 23 µm in bottom with 0.5 µm. Right: FWHM for the wavelength of the acceptance curves in the left plot as a function specific wavelength. The two insets show selected zoom windows of the left plot.

windows of selected areas of the left map.

Several differences is apparent on the wavelength acceptance map for the NIR and MIR regions in figure 4.1 and 4.2. In the MIR region the poling periods allow for a an overlapping spectral coverage continuously tunable by adjusting the temperature. In the NIR region the dispersion variation is significantly smaller and the width of spectral coverage is prioritized above accessibility to every single wavelength. From the right plots, it is observed that the spectral response of an upconversion detector changes for different wavelength regions. The range of converted wavelengths for a given temperature reach from sub-

nanometer bandwidth just around the telecom band up to several hundreds of nanometers at the turning point for the phasematch curve centered at 4100 nm. In the case of a monochromatic signal wavelength, e.g. for spectroscopy with a tunable laser, the narrow bandwidth is an advantage and act as an inherent bandpass filter, but if a super continuum lightsource is used for the spectroscopy the broad acceptance at 4100 nm would be preferred.

4.1.1 Second Generation Module

In connection with the change to detector system configuration with the parametric conversion module it went through minor revisions on the cavity design and major revisions on the thermal management and the mechanical stability. It turned out, that the passive cooling of the pump diode module was insufficient without a bottom plate as heat sink. Active air cooling was tried but caused both cavity instability and an increased amount of dust particles on the mirrors. The new bottom plate was thus produced in aluminum.

The power stability in the first generation have not reached a satisfactory level compared to the expected improvement in the shift from bread board to integrated modules. To improve the mechanical stability in the second version, all the optical mounts in the module was upgraded to double mechanical fixation. The f100-mirror in figure 3.1 proved to be the most sensitive in the cavity and was upgraded to an extra stable mount. The 3D model of the second generation parametric module is displayed in figure 4.3 and an image of the assembled module without the lid is presented in 4.4. The module is designed with an option for operation with a larger beam waist in the PPLN crystal. This is interesting for image upconversion or long range detection and is implemented by replacing the two curved mirrors to some with different radii.

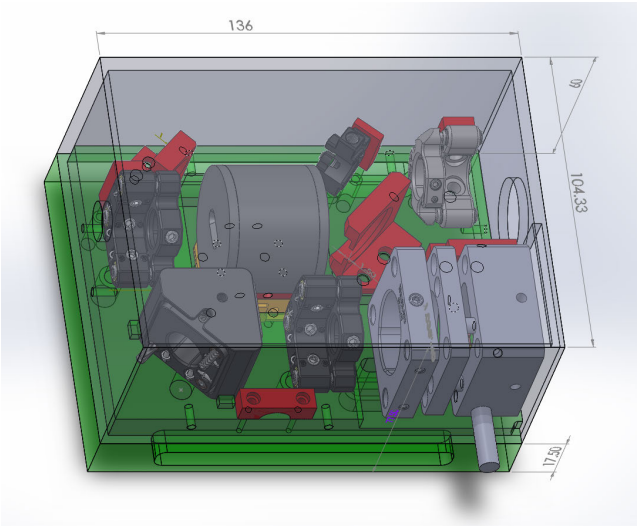

Figure 4.3: 3D model of the second generation parametric conversion module. Red and green color mark the custom parts produced in aluminium. The lid is reused from the first generation printed in ABS plast. The diode pump module is designed in the group for the use in compact parametric modules and the rest is of-the-shelf components.

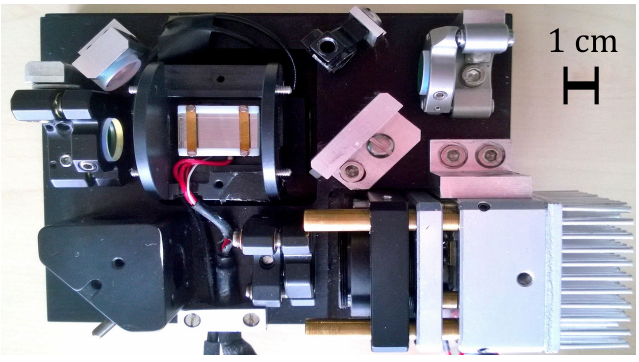

Figure 4.4: Image taken from above of the assembled parametric conversion module, without the lid. The original, Covesion, brass crystal holder is replaced with a custom made of Teflon for passive gradient experiments.

4.2 Upconversion Noise

The key assumption for the advantage of upconversion based detector systems is an efficient and noise free upconversion process. With the tightly focused intracavity upconversion module high efficiency is generally not a problem and quantum efficiencies above 80 % has been measured. It turned out, however, that a high intensity mixing field induces several parasitic nonlinear effects in the crystal. This limits the SNR and in this section the different noise terms will be analyzed and discussed from prior work, measurements and simulations.

The foundation for the noise considerations is a spectral measurement of the output from the upconversion module with no input signal applied, i.e. a 1064 nm laser entering a PPLN crystal in a zero degree incident angle as sketched in figure 4.5, left. Even though the setup is simple, at least six different components contribute to the noise spectrum displayed in 4.5, right. All of the contributions are CW as the mixing laser, and filtering has to be done in either the spatial or the spectral regime. The upconversion module is configured with a 20 mm crystal in the 11.8 µm channel at a temperature of 139.9°C, and an intracavity mixing power on 62 W in a 48 µm beam waist inside the nonlinear crystal. The measurement is done with an Ocean Optics QE6500 spectrometer with a 5 s integration time in a single lens free-space coupling geometry behind a 1064 nm/532 nm bandstop filter. Each of the noise components are described in the following.

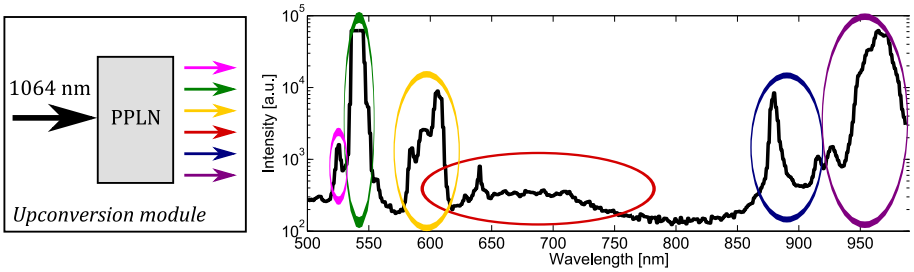

Figure 4.5: Left: Conceptual sketch of the noise measurement setup. A mixing laser at 1064 nm enters the periodically poled lithium niobate crystal and six different noise contributions are generated. Right: Measured spectrum of the noise output alone. *Magenta*: 2^{nd}-harmonic generation *Green*: Raman scattering *Yellow*: Unknown *Red*: Upconverted SPDC noise *Blue*: Pump diode residual and laser crystal fluorescence *Purple*: Upconverted thermal radiation

2^{nd}-harmonic Generation (*Magenta*) With a 1064 nm mixing laser there will be a small part of green light present from the second harmonic generation. Even though this process is not directly phasematched there will be a small conversion from poling errors and birefringent phasematching. The 532 nm light overlap spatially with a collinear signal, but can be removed by a simple long-pass filter and typically it serves as a convenient visible marker for the infrared beam.

Raman scattering (*Green***)** The refractive index and the nonlinear properties of the crystal are determined by the response from the electron cloud in the crystal structure. This response is disturbed by molecular vibrations in the crystal lattice and can be described as a photon/phonon interaction called Raman scattering [36]. If energy is lost from the photon to the lattice it is called a Stoke process and if the energy is gained from it is anti-stoke. The Stoke process will dominate and result in photons emitted at longer wavelengths. In lithium niobate two of the main Stoke peaks are found at $255\,\mathrm{cm}^{-1}$ and $600\,\mathrm{cm}^{-1}$ [17, 62] and the Raman spectra change not significantly with the 5 % MgO doping [63]. The Raman scattering overlap spatially with a collinear signal, but can be filtered away by a short pass filter. The second harmonic of the Raman shifted mixing laser will overlap with the Raman shiftet second harmonic and the peak 546 nm peak appear more powerfull than the main second harmonic peak due to the 532 nm bandstop filter. There should be a peak at 570 nm for the second Raman peak, but it is not observed.

Unknown (*Yellow***)** Several smaller unknown noise contributions have shown up along the way and specifically in the 11.8 µm channel a significant peak around 600 nm is observed. In appendix G data is given for the noise in different poling periods and a multitude of peaks show up. The peaks show up at different wavelengths for different poling periods and some measurements show that the peaks change with temperature, and in the opposite direction as the signal peak. These features indicate that the noise peaks are phasematch dependent and originate from parametric processes.
It could possibly be a Raman shifted mixing field that upconverted the noise at different wavelength or it could be a direct generation of Raman shifted features with respect to the phasematched wavelength as demonstrated by Okishev and Zuegel in [64]. Another possibility could be that it resulted from Raman shifted features that matched the conditions for semi-simultaneous phasematching to be described in section 4.2.1.1 and was thus amplified efficiently throughout the crystal. The many unknown features require further investigation, but if it is any kind of Raman scattering or semi-simultaneous phasematching they are fundamentally limited from overlapping spectrally and can thus be filtered away.

Upconverted SPDC noise (*Red***)** Spontanously parametric downconverted noise photons are generated in a difference frequency generation process stimulated by vacuum fluctuations, where the mixing photons split into two lower energy photons. Following the nature of the vacuum fluctuations the process is stochastic and independent of phasematch. The phasematch is, however, crucial for the amplification of the generated noise photons and thus the amount of noise photons at the output crystal facet. In a perfect poling structure optimized for a SFG process, the generation of SPDC noise photons is insignificant, but due to duty cycle errors in the poling structure there is significant conversion efficiency for all wavelengths. This result in a spectrally broad pedestal of noise photons, described in [15, 16, 65] and discussed further in the following sections. With a broad pedestal of downconverted noise photons some of

them will be at the exact signal wavelength for the optimized upconversion process. Even with a narrow phasematch bandwidth, this results in an efficient upconversion of noise photons coincident in the spectral, the spatial, and the temporal domain. Figure 4.6 demonstrates how the upconverted SPDC (USPDC) noise photons follow the phasematch condition for changing temperatures similar the signal peak would change.
The center wavelength of the peak does not fit with the theoretical prediction for this temperature, but it was verified with a known input signal that the USPDC noise peak indeed overlaps with the signal peak. The reason for the wavelength off-set is probably a result of the free-space coupling to the spectrometer that allows the spectrum to shift towards longer wavelengths for changing input angles.

Pump diode residual and laser crystal fluorescence (*Blue***)** The pump diode residual peak is centered at 880 nm and in the ideal case described in figure 4.1, left, it would not be present. In a real world intracavity setup the pump diode residual is, however, always present to some extent. It is already reduced greatly from the five passes on AR coated mirrors in the cavity and the rest can be filtered by a short pass filter. At 914 nm the fluorescence from the Nd:YVO_4 laser crystal results in a small peak that can be filtered aways as well.

Upconverted thermal radiation (*Purple***)** At 139.9°C the Planck curve describing the black body radiation from the crystal peaks at 7 µm and the second phasematch in the specific configuration peaks at 9.08 µm where the thermal radiation is still significant. This corresponds to 923 nm and 952 nm respectively and fit well with the observed noise peaks in the spectrum. The amount of emitted thermal photons depends on the specific emissivity and thus the absorption for the crystal. As 9 µm is outside the transparency region, black body radiation is emitted in a region of for efficient upconversion. The specific transparency spectrum together with the Planck curve and the phasematch values will determine the exact shape of the upconverted thermal radiation noise peaks. All of the thermal radiation can be filtered away by applying a short pass filter.

From the above descriptions of the different noise contributions it can be concluded, that the USPDC noise stands out as the only one not possible to filter away from an upconverted signal. The following subsection will focus on this noise source specifically.

4.2.1 Upconverted SPDC Noise

The combined process of upconversion of SPDC noise is described quantum mechanically by Tang in 1969 [7] and the importance of the RDC-errors are mostly treated by the Fejer group at Stanford, but the influence on RDC-errors on the USPDC noise have not been treated. The USPDC was mentioned as a reason for changing to a long wavelength pump scheme in [17], but further

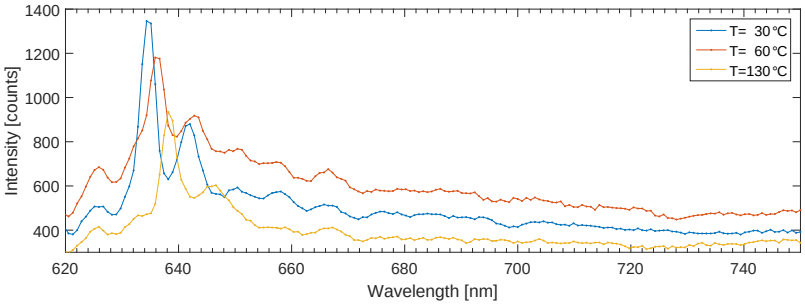

Figure 4.6: Spectral noise measurements at different temperatures for the 11.8 µm period poling channel to illustrate how the USPDC shift with temperature following the phasematch conditions. The change in intensity is assumed to be a result of the individual RDC-errors on the poling structure described in further details in section 4.3.2.4.

details are not treated.
In the case of upconversion of SPDC noise photons, two parametric processes occur simultaneously throughout the PPLN crystal. The first process is the SPDC that generates noise photons from splitting of the mixing laser photons following the energy conservation requirements of the DFG process. The spontanous process can be described as a regular DFG process seeded by a continuum of vacuum fluctuations described as a quasi-continuum of photons with stochastic phase and magnitude. An ensemble of the stochastic photons at each specific energy will average to zero in magnitude, as it is not possible to extract energy from the vacuum fluctuations. The laser analogy is to consider the mixing laser as the exited laser state and the vacuum fluctuations as seed photons for the spontaneous decay to a continuum of ground states. The same approach is used in the description of an optical parametric oscillator, where the intracavity field build up similar to the laser, but with the nonlinear crystal as gain medium. In the case with the upconversion of SPDC noise, no cavity support the modes of the generated photons, and the process remain below threshold. Similar to amplified spontaneous emission in laser gain media the SPDC noise photons are amplified coherently throughout the crystal.
If the SPDC process is phasematched, the device would be considered an OPG, similar to the one described in section 3.2. For the detector purposes, however, the crystal parameters are tuned to support the upconversion process and the amplification efficiency are determined by one of the lopes far away from the main peak in the K-space. In the case of a poling structure with RDC-errors the far away lope will be 2-3 orders of magnitude higher than with a perfect grating, see figure 2.4.
From the SPDC process, there is a spectrally broad noise signal both at MIR and NIR wavelengths, simultaneously growing throughout the crystal with relative low intensity. At the same time, the crystal is optimized to sustain an upconversion process with an efficiency four orders of magnitude higher. This mean that even with no input signal there is generated a peak exactly at the upconverted phasematched visible signal wavelength as observed in figure 4.5.

4.2.1.1 Simultaneous Phasematch Noise Enhancement

The amount of upconverted SPDC noise can be greatly enhanced, if the two parametric processes are simultaneously phasematched. Either semi-simultaneously, where the phasemismatch from the SPDC process is exactly counteracted by the phasemismatch from the upconversion process, or in the super/simultaneous phasematch form where the phasemismatch is zero for both processes.
In the collinear case simultaneous phasematching cannot occur in the applied upconversion configuration, but it have been demonstrated with an ammonium dihydrogen phosphate (ADP) crystal by Andrews et al. in 1970 [66]. The same paper mention the opportunity for collinear simultaneous phasematching in lithium niobate as well, and exactly in the combined 1064 nm, 1550 nm, 3150 nm case, but for *ooe* phasematching type and not *eee* as required with the periodic poled crystals.
In more recent times, the combined phasematch have been investigated with respect to the influence on light sources based on optical parametric oscillators (OPO's). Husam H. Abu-Safe [67] named the parametric processes, resulting from the combined phasematch or higher order phasematch, for multiconversion and measure 5 significant peaks in the output spectrum from a PPLN-based OPO. Another example of multiconversion in OPO's is presented by Köprülü et al. [68] where a single KTP crystal sustain both the spontaneous parametric generation and the subsequent upconversion. This paper include furthermore a simulation of the combined process based on 5 coupled differential equations that fits the picosecond pulsed measurements well, but the exact amount of noise seed is not treated. In 2014 Figen [69] demonstrated a seeded optical parametric generator using an aperiodic PPLN crystal generating mid-IR light enhanced by a simultaneous phasematching scheme.

With a model that includes non-collinear phasematching as displayed in figure 4.7, it is possible to compute the requirements for semi-simultaneous and super phasematch for the combined SPDC upconversion process. In this

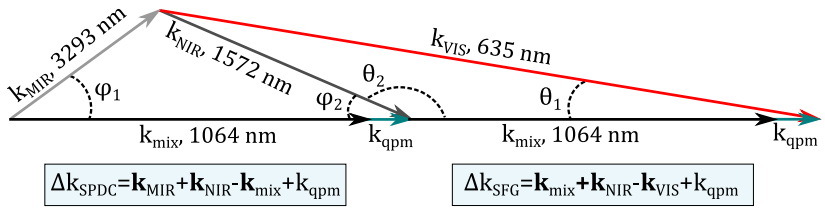

Figure 4.7: Vector diagram of the k-vectors or photon momentum for the combined phasematch process in the case of non-collinear simultaneous phasematching. The wavelengths are included as an example for one of the tested configurations. θ_1 is the controlling angle for the considerations in this section and all angles are internal crystal angles and exaggerated for visibility.

case the individual and combined phasematch are given as

$$\Delta k_{\mathrm{UP}} = k_{\mathrm{NIR}} \cos\varphi_1 + k_{\mathrm{mix}} - k_{\mathrm{VIS}} \cos\theta_1 - k_{\mathrm{qpm}} \tag{4.1}$$

$$\Delta k_{\mathrm{SPDC}} = k_{\mathrm{MIR}} \cos\varphi_2 - k_{\mathrm{mix}} + k_{\mathrm{NIR}} \cos\varphi_1 - k_{\mathrm{qpm}} \tag{4.2}$$

$$\Delta k_{\mathrm{UP}} + \Delta k_{\mathrm{SPDC}} = -2k_{\mathrm{qpm}} + 2k_{\mathrm{NIR}} \cos\varphi_1 - k_{\mathrm{VIS}} \cos\theta_1 + k_{\mathrm{MIR}} \cos\varphi_2 \tag{4.3}$$

following the definitions in figure 4.7 and with the internal angle of the visible light, θ_1, as the controlling angle the other relevant angles are given as

$$\theta_2 = \pi - \mathrm{asin}\left(\frac{k_{\mathrm{VIS}}}{k_{\mathrm{NIR}}} \sin\theta_1\right) \tag{4.4}$$

$$\varphi_1 = \pi - \theta_2 \tag{4.5}$$

$$\varphi_2 = \mathrm{asin}\left(\frac{k_{\mathrm{NIR}}}{k_{\mathrm{MIR}}} \sin\varphi_1\right) \tag{4.6}$$

where equation 4.4 is altered by π, due to the ambiguous triangle case and the actual Matlab implementation. For a specific set of upconversion parameters, with a poling period of 11.8 µm and a temperature of 140°C, the above equations visualize to the phasematch maps in figure 4.8. Frame 1 and 2 display the individual phasematch conditions, where a zero-value correspond to phasematch. In frame 3 and 4 the conditions for semi-simultaneous and super phasematch are shown respectively and it is noticed how this only occur at relatively large angles, that will be scaled by a factor of 2.1 when going to external crystal angles.

The super phasematch are expected to give much higher signal levels than the semi-simultaneous phasematch process, and in order to use the upconversion process for low-noise detection, the detected angles should be kept below the phasematch angle for both processes over the whole spectral range of interest. In figure 4.8 this limits the visible output angle to $\theta_1 = 50$ mrad, corresponding to a NIR signal input angle of $\phi_1 = 118$ mrad, internal angles.

To confirm the calculations of the super phasematched noise a simple experimental setup was build, see figure 4.9 A), where the output of the upconversion module was measured with no input signal. The signal was limited to the spectral region from 600-700 nm with bandpass filters and a 12 mm objective collected the noise to a EM-CCD chip. Positions from 0-30° was measured and a distinct signal showed only at 15°. This is displayed in C) and represents a small fraction of the full noise circle expected from the super phasematched noise, where the width represents the angular acceptance angle for this specific process. In figure 4.8 the expected angle is 69 mrad at 140°C and the measurement is performed at 30°C, but the computation predict an angle variation over the 110°C that is below 0.5 mrad and as this is within the uncertainty of the measurements. 69 mrad is thus the expected angle for the measurement of the super phasematched noise at 30°C. This angle is scaled as sketched in figure 4.9 B), first by the refractive index change in the crystal-air interface, and next by the focusing of the 30 mm concave cavity end-mirror. This scaling results in an expected detection angle at 258 mrad or 14.8°, corresponding to the position of the measured noise signal.

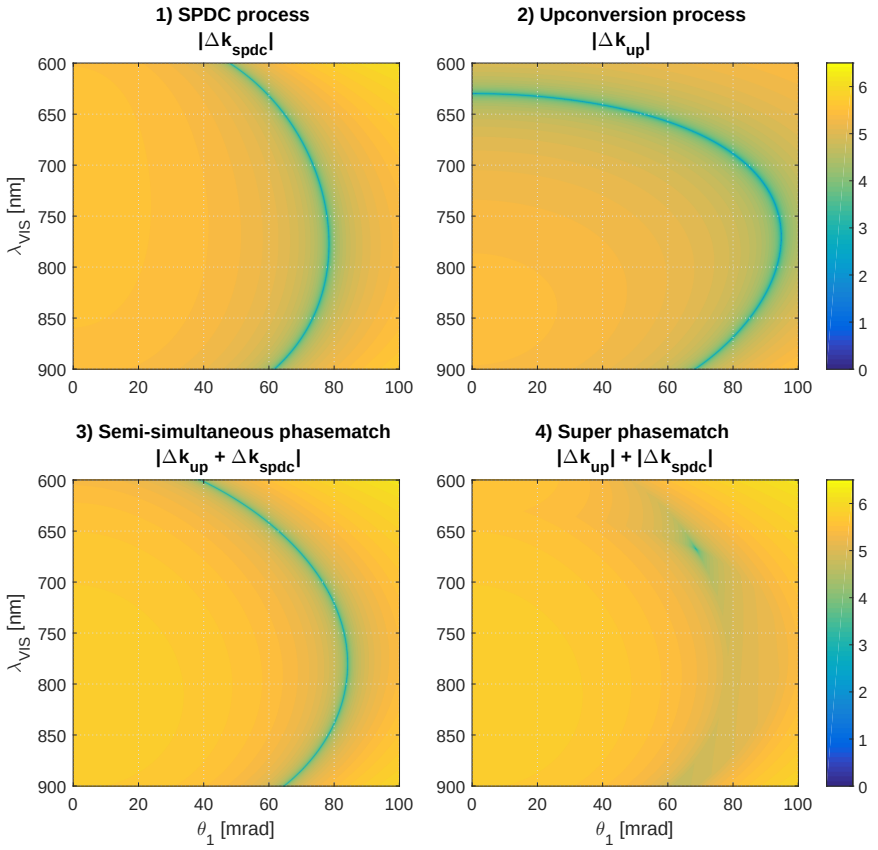

Figure 4.8: Overview of the phasemismatch for the individual DFG (SPDC) and SFG process and the combined processes both in the case of quasi-simultaneously phase match and super phasematch where both processes are required to be phasematched in one point. The computation is run for a 11.8 µm poling period and a temperature of 140°C. All frames maps the logarithmic of the phasesmismatch value in order to enhance the visibility.

Still at 15°, the EM-CCd was now replaced with a grating spectrometer and the spectrum of the noise signal was measured to 669 nm as displayed in figure 4.9 D). It turns out that the wavelength of the super phasematched noise changes with temperature and from computations, similar to 4.9, the wavelength should shift to 679 nm at 180°C, which is confirmed by the spectral measurements in figure 4.9 D).
The intensity of the semi-simultaneous and the superphasematch processes are difficult to compare by use of the spectrometer as the free-space coupling might vary. With the EM-CCD the continuous nature of the semi-simultaneous process complicates a quantitative measurement.

Given the large angles of the super phasematched noise it will not have any practical implications on the detector use of the current upconversion module. An investigation of the other periods in the PPLN crystal for NIR upconversion shows that the poling period 15.8 µm has collinear semi-simultaneous phasematching, but also confined to be at large angles at the signal wavelength. In general the nature of the simultaneous phasematching will allow for angular or spectral filtering of the noise. For other configurations of parametric processes, the angles may be small enough to represent a limitation for low-noise detection, and the conditions should be checked when designing an upconversion module.

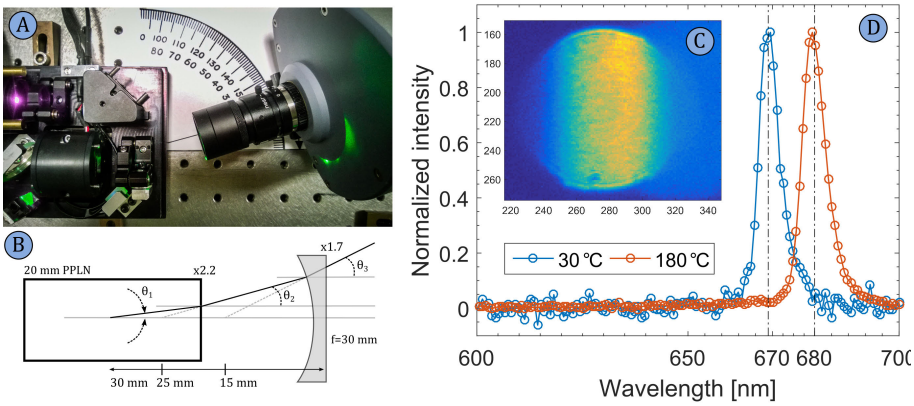

Figure 4.9: A) Measurement setup for detection of the position for simultaneous phasematching. Camera at 15° B) Sketch of the dispersion for the noise generated in the PPLN crystal. C) Small part of the noise ring at 15°, detected by a EM-CCD after a 12 mm objective and a long pass 600 nm, a short pass 700 nm and a Semrock 532/1064 nm bandstop filter. D) A spectrometer was placed instead of the camera and the spectral content of the noise was measured.

4.3 Signal-to-noise Ratio Optimization

With the USPDC noise identified as the main noise source overlapping with the signal, this section will describe the different possibilities to limit its influence on the SNR for an upconversion detector system. The only known way to avoid the noise is to move the mixing laser wavelength to a lower energy than the signal wavelength, and the initial work for this solution is presented in 4.3.3. Optimization by balancing the QE and the generated noise are investigated in the first of the following sections and the possibility for cherry-picking crystals with low SPDC at specific wavelengths are analyzed and discussed in the last sections.

Narrow band filtering is not treated here, but have been demonstrated as a way to increase the SNR in upconversion detector systems [18]. Filtering

cannot remove the noise completely, and the SNR improvement depends on the difference in spectral width between the incoming signal and the generated noise peak. In the case demonstrated with a volume Bragg grating in [18], the filter bandwidth was FWHM=32 pm for the upconverted wavelength at 709 nm.

SNR, NEP and D* Many different terms are being used in the description of detector performance, and it is often complicated to do a correct comparison based on the numbers only. The best way to compare two detectors is to measure and compare the SNR. For the upconversion detector system, the influence on the SNR is twofold; the signal will be influenced by the QE of the nonlinear process, whereas the shift to a detector optimized for shorter wavelengths will decrease the noise. For the initial considerations of detector systems design and performance analysis, the terms noise equivalent power (NEP) and normalized detectivity is often used and both expressions relate directly to the SNR as [70]

$$\mathrm{SNR} = 1 = \frac{\mathrm{NEP}}{\mathrm{Noise}}, \quad D = \frac{1}{\mathrm{NEP}} \quad \text{and} \quad D^* = \frac{\sqrt{A_d \Delta f}}{\mathrm{NEP}} \tag{4.7}$$

where the normalized detectivity, D^*, is included for a comparison that is independent of the detector area, A_d, and the electrical bandwidth of the detector, Δf.

4.3.1 Intensity Optimization

The reasoning behind intensity optimization relies on the fact, that the upconverted SPDC noise are proportional to the squared mixing laser intensity, whereas the QE for the upconversion have a linear dependency for small intensities and converge towards unity for higher intensities. In order to confirm these relations and investigate an optimum point for the SNR, a simple upconversion detection setup was built and a sketch is displayed in figure 4.10. The setup was automated by LabView in order to acquire corresponding measurements of the intracavity leak and the EM-CCD signal, with and without an incoming signal, for varying diode pump currents. The work with intensity optimization is reported to the OSA topical meeting ASSL 2015 in Berlin [71] and the poster is included in appendix F.

The results for one of the measurements series is displayed in figure 4.11. Each data point is the accumulated value for the pixels covering the detected signal, and is obtained as an average over 100 frames, each with an exposure time of 1 ms. The photon number are estimated from a calibration of the EM-CCD counts with respect to the gain factor, the QE, and the well-depth of the specific chip. The output noise rate was further calibrated with respect to the measured transmission of the out-coupling mirror in the upconversion cavity. This mirror was calibrated with a HeNe laser at 632.8 nm and showed a transmission in the order of 40 %.

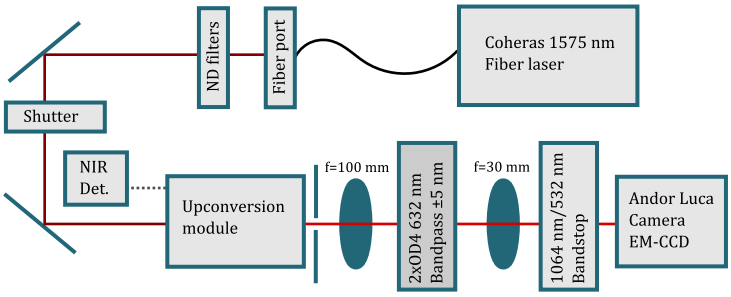

Figure 4.10: Setup for SNR measurements with the upconversion module. The shutter and the camera are synchronized to measure the output, with and without input signal for varying levels of mixing power inside the upconversion module. The NIR detector monitors the cavity leak, i.e. the mixing field intensity. The 1064nm/532nm filter are included mostly to protect the EM-CCD from high intensity laser light under setup arrangement.

It is verified by the data in figure 4.11 how the upconversion noise grows quadratically with intensity and how the QE depletes for high intensity mixing fields. The measurements are consistent with a QE calculation, not using fitting parameters, but experimental parameters. It should, however, be stressed that the measurements are normalized to one, as depletion is clearly observed. This corresponds to a measurement of the internal QE and the overall QE for the upconversion was lower in this specific measurement. In other measurements an overall QE$>$ 80 % have been confirmed. Similar measurements have been presented by Langrock et al. [72] in an investigation of noise properties of long and short wavelength pumped upconversion in bulk and waveguide based systems.
The SNR is included with three different definitions in order to investigate the optimum mixing field intensity. SNR_1 is the direct implementation as the relation between the mean signal and the mean noise, in this case the relation between the signal and no-signal case. SNR_2 is the relation between the variance of the signal and the noise. SNR_3 is defined as the relation between the signal with the noise subtracted and the standard deviation of the mean for the signal. This is also defined as the inverse of the *coefficient of variation*. All the SNR-definitions are included below.

$$\mathrm{SNR}_1 = \frac{\sigma^2_{signal}}{\sigma^2_{noise}}, \quad \mathrm{SNR}_2 = \frac{\langle signal \rangle}{\langle noise \rangle}, \quad \mathrm{SNR}_3 = \frac{\langle signal \text{ - } noise \rangle}{\overline{\sigma}_{signal}} \tag{4.8}$$

From the plot of the different SNR's in figure 4.11 it is seen how the SNR_1 and SNR_2 are limited by the high average value on the noise, whereas SNR_3 benefits from the stability of the noise and exploits the background measurement. With SNR_1, there is an optimum as expected from measurement A) and B), and for SNR_2 the values levels out without dropping for higher intensities. This can be explained if the noise level average rise, but the relative variation falls off, due to the stochastic noise average over a large ensemble.
From a practical perspective, however, SNR_1 reaches an optimum at more or less the same value as SNR_3, as the price and complexity continues to rise for

higher intensities, but the SNR levels out. The value at 300 kW/cm^2 can thus be regarded as the optimum intensity for an upconversion module with a short wavelength mixing field and a 20 mm long PPLN crystal. The dependency on the crystal length may be estimated from equation 2.8, where the efficiency scales with the length squared and with a crystal of twice the length the optimal intensity is then reduced to 75 kW/cm^2.

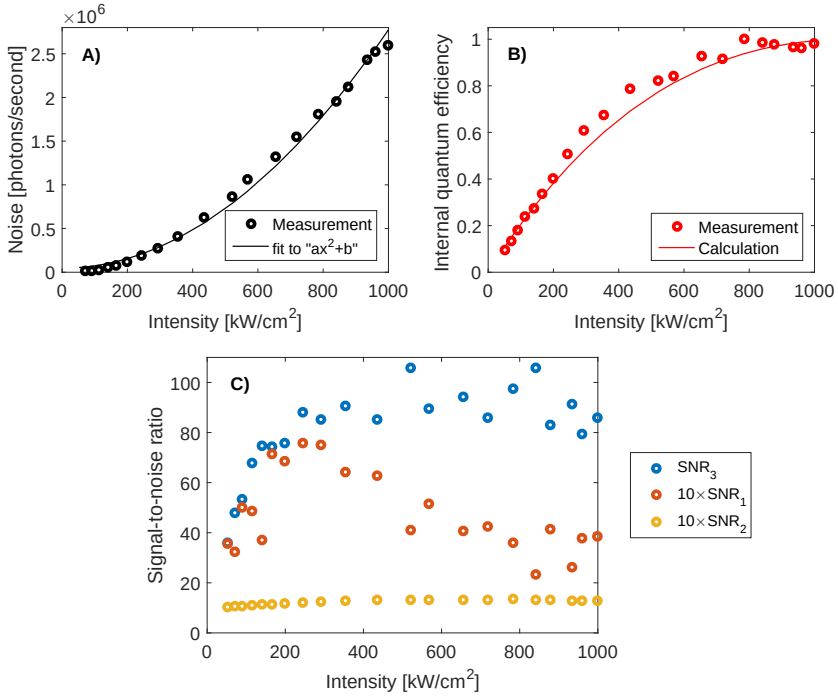

Figure 4.11: Corresponding measurements of noise, QE and SNR with respect to the mixing field intensity at the beam waist inside the PPLN crystal. The measurements are done with a 50 µm beamwaist and the intensity are changed by varying the diode current for the mixing laser. The input signal are approximately 12 pW at 1575 nm. A) Measurement of the noise with no input signal plottet with a second order fit. B) Upconverted output plotted, normalized to one and plotted as internal QE to show saturation, and for comparison with the calculated value for the QE, using experimental values from the system. C) The signal to noise ratio calculated with from three different definitions and scaled for comparison.

4.3.2 Investigation of the USPDC Grating Specificity

In the previous sections, it has been qualitatively established that the USPDC noise is significantly higher when RDC-errors are present in the poled grating structure. This section will first quantify this dependency from grating measurements, and secondly use two numeric models to investigate how the amount of USPDC vary for different sets of RDC-errors. The goal is that an understanding of the RDC-error dependency will allow for selection of low noise PPLN crystals for specific low-noise applications.

4.3.2.1 Measurements of the RDC-errors on the Poled Grating

In order to get a better understanding of the actual grating structures in the crystals used for the different parametric processes, four crystals was selected for measurement. With an automated confocal microscope (Sensofar PLu Neox), borrowed at Danish National Metrology Institute (DFM), the surface of one poling channel for each of the four crystals was mapped out with a resolution of 0.66 µm in both the lateral and downward dimension. The actual poling is not possible to measure, but to mark the crystals the surface have been etched in the same pattern used to define the microelectrodes. An example of a measured crystal segment is given in figure 4.12, displayed both from above and in an averaged cross sectional view. The duty cycle errors and missing reversals are immediately visible, and so is a small variation of the poling period in the surface plane. It was only possible to map around 90 % of the crystal length due to a steep rise of the surface near the two ends.
To continue the analysis the grating measurement was converted to a vector of alternating zero and ones. From here a $|\mathrm{FFT}|^2$ was performed and the result is displayed in 4.13, together with the $|\mathrm{FFT}|^2$ of a simulated grating with 12 % RDC error, and one of a perfect grating.

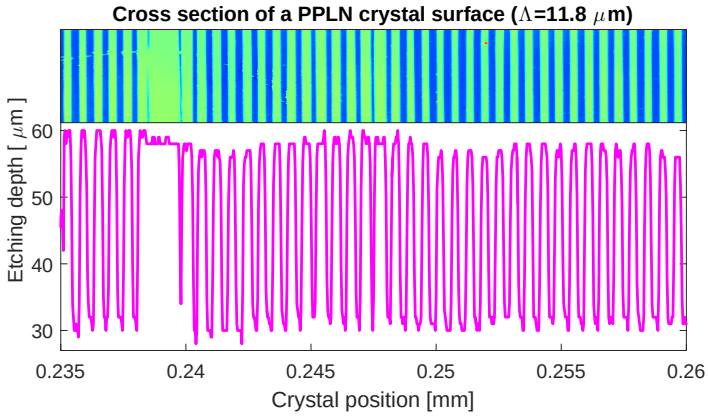

Figure 4.12: Example of a subdivision of the measurement data obtained with a confocal microscope. The section is selected to show missing reversals, lateral tapering and duty cycle errors.

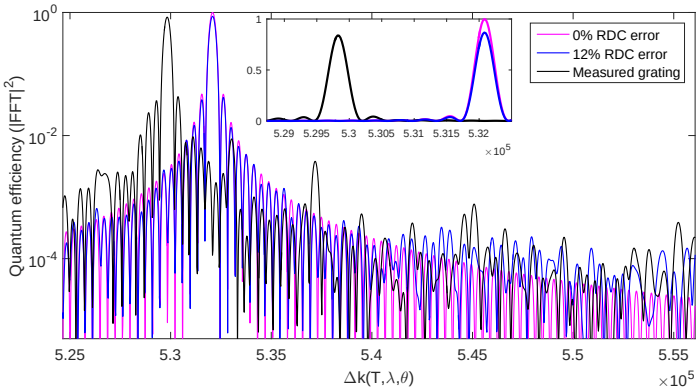

Figure 4.13: Close up on the first resonant peak for the $|\mathrm{FFT}|^2$ of the measured grating, a simulated perfect grating and a simulated grating with 12 % RDC error. The axes are labelled with Δk and QE respectively for illustrative reasons. By changing the angle, the temperature or one of the wavelengths for the parametric process the grating response will result in different QE values. Insert plotted on linear scale for peak height comparison and the ΔK-difference in the peak positions corresponds to 5 nm change in the phasematch.

A comparison of the measured grating with the simulated gratings displays that the drop in conversion efficiency and the overall structure correspond to a RDC error of around 12 %. Furthermore it is visible that the crystal grating has an offset in the poling period compared to the specified value on 11.8 µm in this case. The effect of the RDC errors and the results corresponds fine with similar data demonstrated in [15].

A statistical analysis of the poling periods is displayed in the histograms in figure 4.14, where the distribution of high and low domains are computed together with a Gaussian fit. The exemplified crystal is specified to a period of 11.8 µm. A few outliers where multiple missing reversals occur are removed for visibility of the main distribution, and the skewness of the distributions may be due to inclined walls from the etching procedure and does not necessarily represent an actual skewness in the poling domain distribution. From the Gaussian distribution fit, the size of the high and low domains are 6.0 ± 0.7 µm and 6.0 ± 0.6 µm respectively, where the uncertainty is defined by the standard deviation of the respective distribution. The standard deviations thus corresponds fine with the 12 % RDC-error estimated from figure 4.13.
The accuracy of the statistical analysis are limited by the spatial resolution of the measurements, and the standard deviation on the domain width corresponds to approximately one pixel, but even with the uncertainty the period are larger than specified.
Measurements on two crystals with a poling period specified to 22 µm was also done and they showed the same tendencies for regular distribution of error and missing reversals. The statistics on these gratings showed that the absolute error was approximately the same or even smaller. This results in a relative error

on 4-5 % and indicate that the problem with RDC-errors generally is worse for small period structures. The statistical data for all the crystals are found in appendix H.

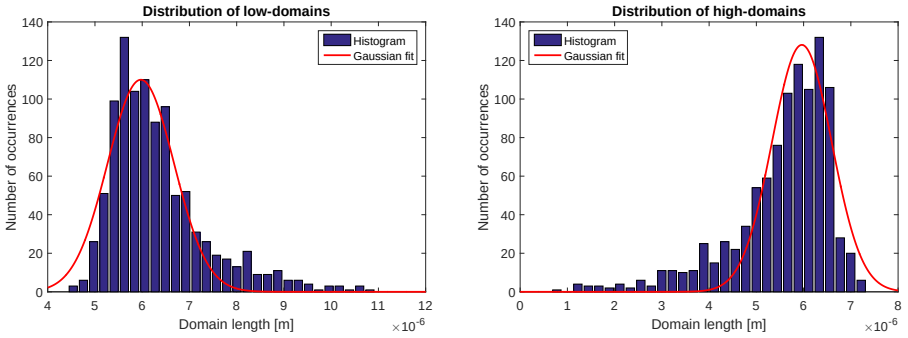

Figure 4.14: Distribution of the high and low patterns in the etched pattern that represent the poled grating in crystal 2 with $\Lambda = 11.8\mu$m. It is not known what polarization each of the high and low level corresponds to. Each histogram are fitted to a Gaussian distribution in order to get statistical information of the measured distribution. A few outliers with multiple missing reversals are removed, and the skewness may be due to inclined walls from the etching procedure and not actual skewness in the poling domain distribution.

4.3.2.2 FFT Based Simulation

As a tool for further investigation of the USPDC noise a simple quasi co-linear FFT-based model was built using the theory for spontaneous parametric fluorescence explained by Yariv [73] in combination with the general equations for upconversion efficiency presented in section 2.1.1.1. The model assumes that crystal can be divided in two regions. One where the SPDC is generated and one where it is upconverted, see figure 4.15.

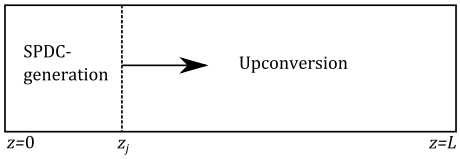

Figure 4.15: Moving boundary principle for the FFT-based USPDC model.

To included that the two processes happens simultaneously in a physical system, and that both are length dependent, the calculation is done for several divisions and averaged. The model expression in equation 4.9 is a multiplication of the generated SPDC power and the upconversion efficiency. The typical sinc-function dependency is replaced by a $|\mathrm{FFT}|^2$ of the poled grating, to allow for implementation of grating errors.

$$P_{\mathrm{USPDC}} = \frac{1}{N_z} \sum_{1}^{N_z} P_{\mathrm{proc.}}^{\mathrm{SPDC}} \eta_{\mathrm{proc.}}^{\mathrm{up}} \eta_{\Delta\mathrm{k}}^{\mathrm{SPDC}} \eta_{\Delta\mathrm{k}}^{\mathrm{up}} \tag{4.9}$$

where

$$P_{\mathrm{proc.}}^{\mathrm{SPDC}} = \frac{-\hbar\omega_{\mathrm{MIR}}\omega_{\mathrm{NIR}}^4 n\omega_{\mathrm{NIR}} d_{\mathbf{eff}}^2}{\pi^2 c^5 n_{\mathrm{MIR}} n_{\mathrm{mix}} \epsilon_0} L^2 P_{\mathrm{mix}} d\omega_{\mathrm{NIR}} \varphi_2 d\varphi_2 \tag{4.10}$$

and $\eta_{\mathrm{proc.}}^{\mathrm{up}}$ is the upconversion efficiency stated in equation 2.8. Following section 2.2.2, $\eta_{\mathrm{proc.}}^{up}$ and $\eta_{\Delta\mathrm{k}}^{\mathrm{SPDC}}$ is the respective $|\mathrm{FFT}|^2$-values corresponding to the Δk-values for each of the modelled wavelengths. $d\omega_{\mathrm{NIR}}$ is defined by the step size of wavelength vector in the model, φ_2 is defined from the convention in figure 4.7 and $\varphi_2 = d\varphi_2$ in the quasi-co-linear model.
All the terms in 4.9 is dependent on temperature, wavelength, crystal length and angle. Except for the angle, all the dependencies are included in the model. More specifically, the angular dependency is only included through the definition of the divergence of the SPDC in equation 4.10 and the variation from the phasematch is ignored. This seems reasonable for small angles that is typically covered within the acceptance bandwidth of the parametric process. The angular dependency could be implemented by an extra for-loop for large angle investigations, but it would increase the computation time significantly. The model can inherently predict the case of co-linear super phasematch, but semi-simultaneous phasematch and Raman scattering is not included.

Figure 4.16 presents a comparison between the amount of generated USPDC noise photons with and without RDC errors, on the poling structure. This indicate that there are typically two orders of magnitude more noise generated with the RDC errors compared to a process with a perfect grating. This predicts a large potential for optimized poling procedures, even though it might be fundamentally limited by the current poling procedure described in section 2.3.
In the case with an RDC error on 12 %, corresponding to the measured values in section 4.3.2.1, the modelled peak value of the generated noise varies significantly for different sets of RDC-errors. 100 different gratings was simulated and the mean spectra is plotted together with the worst and the best case scenario in figure 4.16. The mean value was 1278 counts/s±67 %, where the variation is specified as a single standard deviation. From the worst case to the best case, there was more than an order of magnitude difference in the amount of generated noise, indicating that it might be beneficial to cherry-pick, or at least check the crystals for use in upconversion based detection systems designed for specific wavelengths.
In real detector systems, the collected noise is not limited to the peak value, and all photons within the spectral band of the applied filters is collected. Furthermore the peak value in the simulation is affected by the $\Delta\lambda$ in the model and it is best to compare with experiments with summed intervals. Comparing with the system used in section 4.3.1 the detected photons should fall within the region from 627 nm-637 nm and for a mixing field intensity at 637 kW, as applied in the simulation, the measured number of noise photons per second was detected to $\sim 1.5 \cdot 10^6$ photons/s. This is compared with the summed value from the simulation at $2.2 \cdot 10^5$ photons/s for the mean case and $3.1 \cdot 10^4$ photons/s and $9.4 \cdot 10^5$ photons/s for the minimum and the maximum case respectively. This show good agreement between the simulation and the measurements, when the uncertainty on the measurements and the unknown grating is taken into consideration, as well as the uncertainty on the amount of generated SPDC noise photons in the model.
Following from the several measured noise effects not included in the model, it is expected that the noise level predicted by the model is lower than measured. The critical point for this simulated number of noise photons is the choice of the collection angle, ϕ_2 in equation 4.10. It is chosen to be the largest angle that can pass through the mixing beam over the full crystal length. It have to be within the beamwaist limit and at the same time stay within the detection angle defined by the pinhole diameter in front of the detector.

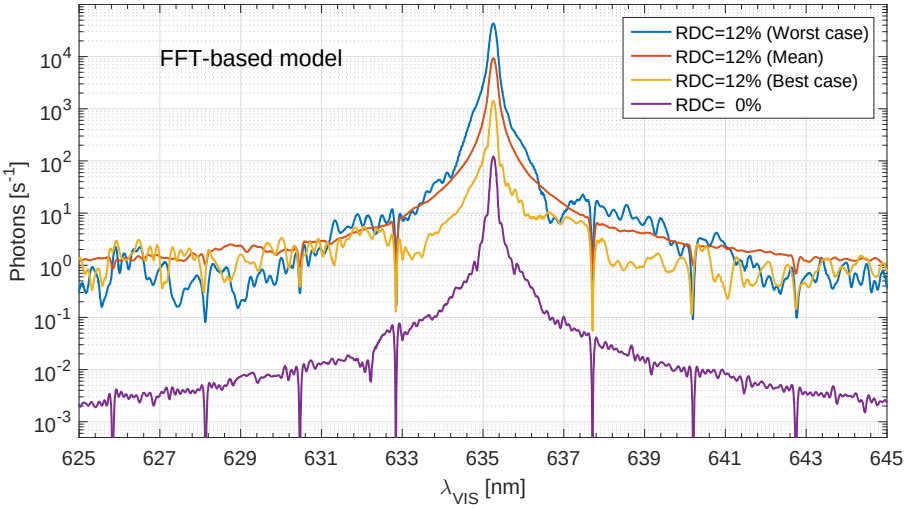

Figure 4.16: FFT-based simulation of the generated USPDC noise photons in a 20 mm PPLN crystal in the 11.8 µm poling period at a temperature of 130°C with a 637 kW mixing field intensity. The mean, worst and best case sceneries is based on simulations of 100 poling structures each with a different set of RDC-errors.

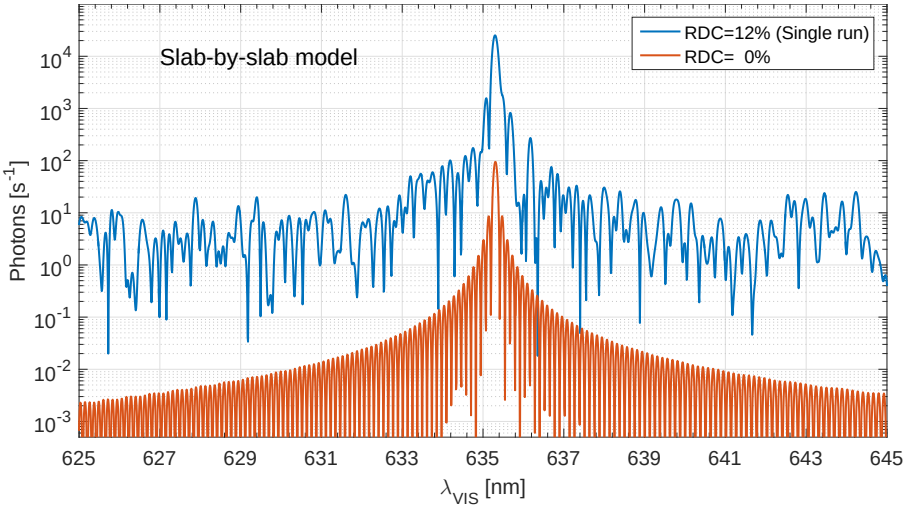

Figure 4.17: Slab-by-slab simulation of the generated USPDC noise photons in a 20 mm PPLN crystal at a temperature of 130°C with a 637 kW mixing field intensity.

4.3.2.3 Slab-by-slab Simulation

Another model based on the coupled equations presented in equation 2.3-2.5 was implemented to verify the FFT-based model. This model solves the simultaneous and coupled DFG and SFG process slab-by-slab throughout the crystal. Equal to the first order Runge-Kutta described for a single parametric process in section 2.1.1.2. To include an extra parametric process the number of equations is extended to four and two coupling terms are introduced to give

$$\frac{da_{\mathrm{NIR}}}{dz} = -ig_{\mathrm{SPDC}}a_{\mathrm{mix}}a^{*}_{\mathrm{MIR}}\exp(-i\Delta k_{\mathrm{SPDC}}z) \tag{4.11}$$

$$- ig_{\mathrm{up}}a^{*}_{\mathrm{mix}}a_{\mathrm{VIS}}\exp(-i\Delta k_{\mathrm{up}}z) \tag{4.12}$$

$$\frac{da_{\mathrm{MIR}}}{dz} = -ig_{\mathrm{SPDC}}a_{\mathrm{mix}}a^{*}_{\mathrm{NIR}}\exp(-i\Delta k_{\mathrm{SPDC}}z) \tag{4.13}$$

$$\frac{da_{\mathrm{mix}}}{dz} = -ig_{\mathrm{SPDC}}a_{\mathrm{NIR}}a_{\mathrm{MIR}}\exp(i\Delta k_{\mathrm{SPDC}}z) \tag{4.14}$$

$$- ig_{\mathrm{up}}a^{*}_{\mathrm{NIR}}a_{\mathrm{VIS}}\exp(-i\Delta k_{\mathrm{up}}z) \tag{4.15}$$

$$\frac{da_{\mathrm{VIS}}}{dz} = -ig_{\mathrm{up}}a_{\mathrm{mix}}a_{\mathrm{NIR}}\exp(i\Delta k_{\mathrm{up}}z) \tag{4.16}$$

where g and Δk is implemented following equation 2.7 and 2.6. A similar simulation approach to a dual simultaneous parametric process is described by Köprülü et al. [68] for the case of five interacting pulses.
On the input side a mixing laser is applied together with an amount of virtual MIR seed defined by the vacuum fluctuations. In this case a single photon in each possible mode in the k-space for the specific process. The mode density and the resulting seed is defined following [73] as

$$a^{\mathrm{seed}}_{\mathrm{MIR}} = \sqrt{\frac{ck^{2}_{\mathrm{MIR}}dk_{\mathrm{MIR}}\varphi_{1}d\varphi_{1}}{4\pi^{2}n_{\mathrm{MIR}}}} \tag{4.17}$$

where φ_1 is defined from the convention in figure 4.7, $\varphi_1 = d\varphi_1$ in the quasi-co-linear model, and dk_{MIR} is defined from the vector of modeled wavelengths. Both the angle and the wavelength vector is defined equally to the FFT-model. The seed could alternatively have been simulated by half a photon in each mode for both the NIR and the MIR wavelengths. This results in direct upconversion of the virtual photons and is not physical at low output powers. The process of the field build-up in the first few slabs is sketched in figure 4.18.

The results is presented in figure 4.17. Compared to the FFT-based model results in figure 4.16 the peak level of the single run with RDC errors fit within

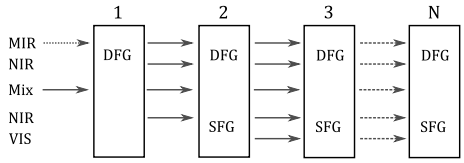

Figure 4.18: Amplification and seed concept for the slab-by-slab model.

the expected values of the FFT-model. For the same grating, exactly, there is only a small discrepancy in the generated noise spectrum, see appendix I. In the case with no RDC errors the SBS-model fit with the spatial frequency structure in figure 2.4. This indicate that the FFT-model predict too many noise photons in case of a perfect grating. The difference in the fine structure on the flanks in figure 4.17 and 4.16 require further investigations, but will only cause little effect on the total number of generated noise photons.

Compared to the FFT-based model the slab-by-slab approach is more intuitive, and it includes coherent amplification directly, however, to include the semi-simultaneous phasematch an extra exponential term have to be included for the combined phasematch condition. This was not necessary in the current case, but is optional for future investigations. The SBS-model has to step through all the steps required to resolve the RDC errors on the grating and in its current form is 30 times slower than the FFT-model. As they give approximately the same results the FFT-model is the simple choice for most investigations. In the process of selecting the right crystal, the models could be used to investigate a measured grating structure, if direct noise measurements is not possible.

4.3.2.4 Temperature Dependence of Upconverted SPDC Noise

To investigate the noise further, the temperature dependent noise output was measured in different filter configurations. The measurement setup consisted of the upconversion module, where the noise was collected by a EM-CCD camera and the leak power from the cavity was recorded simultaneously with the noise measurement. The setup is sketched in figure 4.19 and is fully automated and computer controlled. The temperature controller starts a well-defined sweep and with regular time intervals, a measurement of the leak power and a number of frames from the EM-CCD is recorded. A sweep rate at 0.1°C/s was used, the aperture was limited to 4 mm in diameter and the lens was a 30 mm lens placed in a 2f distance from both the crystal center and the EM-CCD.
The results of several sweeps are presented in figure 4.20 where the photon

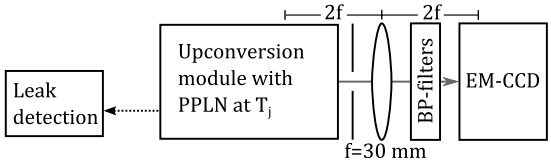

Figure 4.19: Setup for measurement of the upconversion module noise as a function of the temperature.

counts are estimated following the same procedure as the data in figure 4.11. The two sweeps with the broad transmission window display very good consistency indicating that the noise is indeed deterministic. Comparing with the measurements done with the narrow band filters the overall noise level is reduced significantly, but several features can be recognized, which is surprising

when the spectrum in figure 4.5 is taken into consideration. Here a peak is centered around 600 nm, which should be excluded with the narrowband filters. The measurements in figure 4.20 indicate that there are some spectrally broad features on top a constant offset only varying slowly with temperature. A comparison including the measurement with a different poling error indicates, that both the offset value and several of the features are specific for each set of RDC-errors on the poling structure.

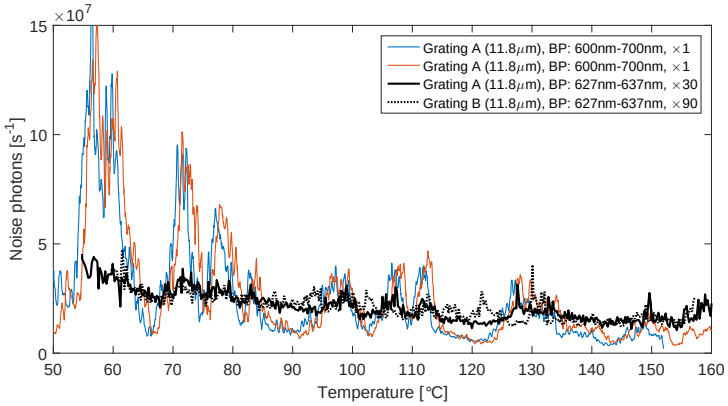

Figure 4.20: Noise photon output from the upconversion module at 417 kW/cm^2 mixing field intensity with respect to the PPLN temperature. Measured for two different crystals, A and B and two different filter configurations. The intensities are estimated values calibrated with respect to mirror transmission, EM-CCD QE, exposure time and the amount of electron multiplication in the given measurement series.

Figure 4.21 is included to confirm the conclusions from the 11.8 µm measurements. It is measured in a transmission region from 650 nm-700 nm and in a 13.8 µm poling period channel, where the phasematch fall within this wavelength region for the measured temperature range. A check of the spectrum in this transmission window, showed no distinct features neither in high or low noise regions, but the sweep still shows large variations and distinct features. Comparing the measurements from crystal A with the sweep for another crystal B, in the same poling period, it is interesting to see that the large feature at 75°C is reproduced, but shifted a few degrees. This indicates that not all the features are poling error specific. Furthermore, there is a consistent dip in the cavity leak power exactly matching this feature. A dip should however induce a dip in the noise as well, and further investigations is needed to explain this. The features at 125°C and 140°C is on the other hand only present for one set of poling errors and the overall offset variation was not observed for these specific sweeps.

The measurements confirm the potential for cherry-picking of low noise crystals for specific wavelengths. Further investigations are needed to see if tuning of the mixing wavelength would be another way to avoid the largest

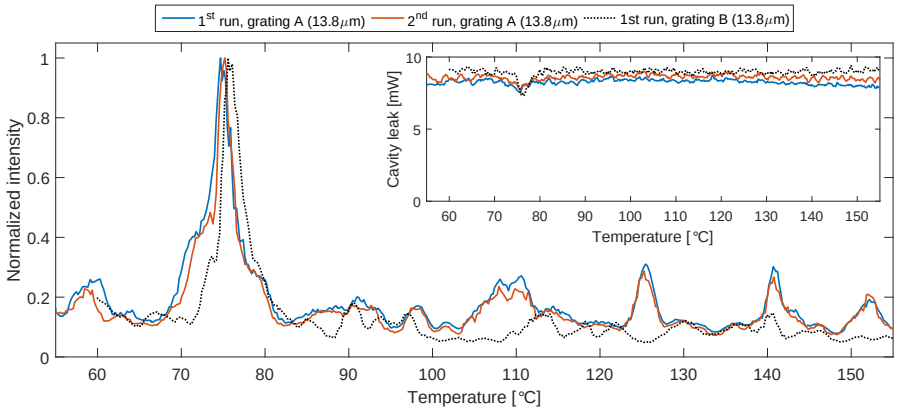

Figure 4.21: Noise photon output from the upconversion module at $\sim$ 400 kW mixing field intensity with respect to the PPLN temperature. Measured for two different crystals, A and B and a 650 nm-700 nm bandpass filter configuration. The intensities are estimated values calibrated with respect to mirror transmission, EM-CCD QE, exposure time, and the amount of electron multiplication in the given measurement series. The cavity leak to intracavity field ratio is 3850.

RDC induced noise features. These investigations should be done with narrow band filters, preferably tunable, and a spectrometer with a better spectral resolution.

In figure 4.22 a temperature sweep is simulated using the FFT-based and the SBS model. Except from an intensity difference the simulations agree qualitatively on the temperature dependence of the noise. It is assumed that the discrepancy rises from the very different nature of the two models and that the slab-by-slab model is closest to the real values expected within the assumptions.

In the measured sweeps in figure 4.20 corresponding to the model in figure 4.22, the features much narrower and peak-like. This supports the analysis, in section 4.2, that Raman scattering may add significantly to the total noise count. The slow variation in the simulation might cover the offset in the sweeps, and further investigations could show that this is the only significant feature if very narrow band filters are used. A further investigation should however be performed in order to explain the discrepancy between theory and measurements.

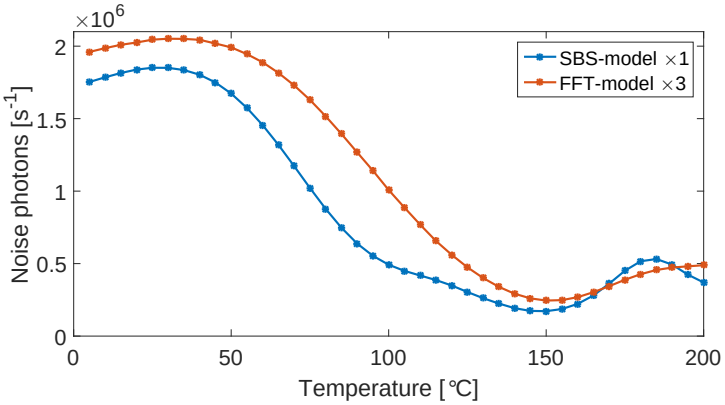

Figure 4.22: Simulation of the temperature sweep for both the SBS model and the FFT based model. The FFT model is scaled a factor of three for shape comparison, and the parameters for the model are similar to the ones used for figure 4.16 and 4.17

4.3.3 Long Wavelength Mixing

A proved solution to the problem with USPDC noise is to shift the mixing wavelength to be longer than the signal wavelength. This is described in e.g. [17], [72] and relies on the principle of energy conservation that only allows the spontaneous parametric fluorescence at downconverted wavelengths.
The long wavelength solution requires an efficient mixing laser available at longer wavelengts than the signal and that the SFG of the signal end up in a region where the detector noise improvement is still beneficial. In the case of upconversion for MIR applications it would be complex to use a longer mixing laser and the SFG of the signal will not reach the region of silicon detectors.
Previously the long wavelength mixing have been performed in single pass systems using PPLN waveguides, and in order to investigate the possibilities to apply the principles with the intracavity and bulk crystal approach a 1.9 m Tm:YLF laser system was built and tested. The work was primarily done as the master thesis project by Rasmus Lyngbye Pedersen, supervised by Lasse Høgstedt and Peter Tidemand-Lichtenberg [74]. This chapter will summarize the main conclusions relevant for the use of upconversion detection and all figures is reproduced from the master thesis. The work was presented by R. Pedersen at ASSL Berlin 2015 [75].

The advantage of long wavelength mixing is often explained in diagrams similar to figure 4.23, where it is clear why the USPDC is a problem and how it can be avoided by a change of mixing wavelength. In this case the Tm:YLF laser was selected as a good candidate for a polarized, tunable, and potentially high power solid state laser. The final Tm:YLF laser configuration for long wavelength pumped upconversion is presented in figure 4.24. Several earlier iterations of the cavity is described in the master thesis along with optimization issues regarding the choice of prism, the mirror configuration, the alignment procedure, and diode pump configuration, where a setup with dual pumping was demonstrated to increase the intracavity mixing field. The mirrors in the setup are highly reflective in the region around 1.9 µm, and at the signal wavelength at 685 nm it was not possible to find a transmissive mirror that was available from any supplier within the time frame of the project. The solution with the prism coupling was chosen instead of the standard procedure in the

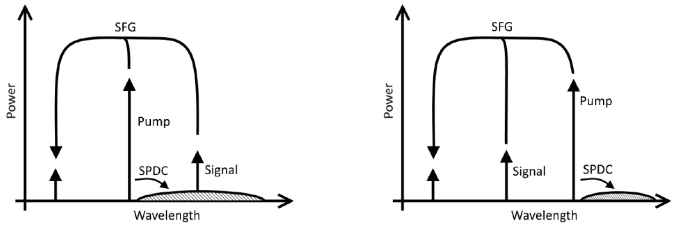

Figure 4.23: Left: Short wavelength pumping scheme with unavoidable SPDC noise at the signal wavelength. Right: Long wavelength pumping scheme with no SPDC noise at the signal wavelength.

short wavelength pumped upconversion module described in this thesis. The prism configuration, furthermore, allowed for tuning of the mixing laser wavelength by adjustment of the cavity feedback through angle of the M8 mirror. An intracavity field at 13 W was achieved without PPLN crystal placed intracavity and 9 W including the crystal. The tuning capability is demonstrated in figure 4.25, left, where each wavelength was possible to run as single mode. The wavelength steps across the tuning range originates from the water vapor absorption lines from the air in the cavity length. Long wavelength pumped upconversion is demonstrated in figure 4.25, right, with a peak QE on 0.019 % compared to a theoretical maximum on 0.18 %.

As a follow up on the master project and before the ASSL presentation it was tried to compare the upconversion noise between the long and the short wavelength pumped systems directly. In this setup a leak from the 1.9 µm laser was coupled to the short wavelength pumped upconversion module and a 1064 nm laser was guided to the long wavelength pumped laser. In this configuration the parametric process is exactly the same, but with opposite signal and mixing wavelengths. The comparison was performed with a grating spectrometer in order to produce a spectral sweep similar to figure 4.5, but it turned out, that the detected fluorescence from the Tm:YLF crystal at the upconverted signal wavelength was at least 10 times higher than the noise expected for the short wavelength system. It was thus not possible to investigate how the long wavelength pumped upconversion process added to the final noise count.

An improved system with higher quantum efficiency would include a longer PPLN crystal with a coating optimized for the long wavelength mixing and a higher efficiency prism configuration. If the prism is moved to the other side of the PPLN crystal and the signal passed through M8 instead of M2,

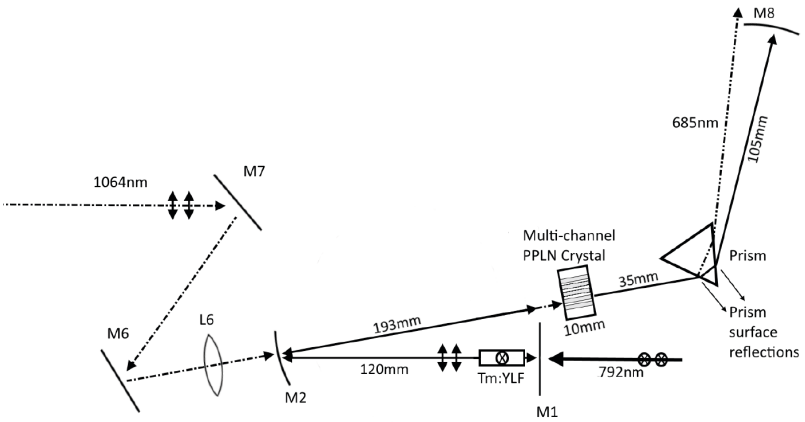

Figure 4.24: Tunable 1.9 µm Tm:YLF setup for test of long wavelength mixing upconversion. Note that a similar setup was designed with two 792 nm diode pump lasers configured in different polarizations in order to achieve higher gain and thus higher intracavity mixing field.

the fluorescence from the Tm:YLF is separated from the upconverted signal, but the tuning capability of the cavity is lost. The broad gain spectrum of the Tm:YLF is an advantage in terms of tuning, but a way to control the wavelength, or at least stabilize it to a single mode, is required to achieve an efficient long wavelength pumped upconversion system.

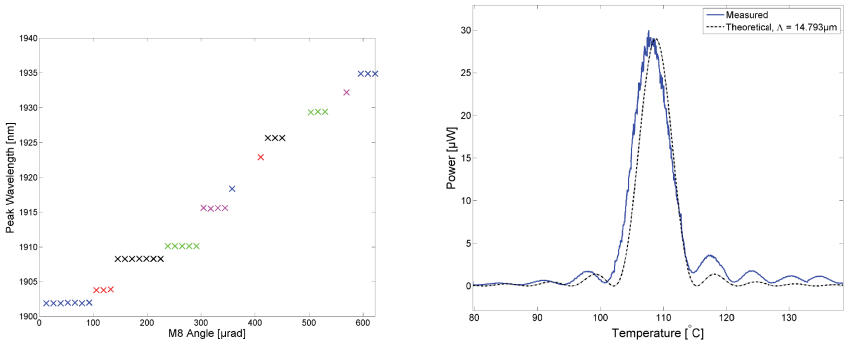

Figure 4.25: Left: Wavelength tuning of the mixing laser as a function of the end mirror angle. The wavelength steps in the tuning originate from water vapor absorption lines from the air in the cavity length. Right: Demonstration of long wavelength pumped intra cavity upconversion, compared to a theoretical calculation of the conversion efficiency as function of temperature.

CHAPTER 5

Application Tests of the Upconversion Technology

The prior work section 1.3 describes how upconversion based detectors have been applied in fields as different as astronomical observations, aerosol detection and hyperspectral imaging. The promise of detectivities improved by several orders of magnitude by shifting from the infrared to the visible regime remains, even after the noise contributions described in section 4.2, but for actual implementations, it is complicated to predict how the SNR in fact would benefit from the upconversion technology. It depends on the specific signal wavelengths, the angle of incidence, the spatial and temporal shape of the signal, the polarization,the phase coherence and the requirements on QE, and noise balance. Detector comparisons are always complex, and with an upconversion module in combination with a visible detector much is virgin ground, and application specific direct comparisons is preferable.

Two completely different applications are presented in this chapter, and both are included as published. There is no specific strategy in the selection of the two applications, other than the curiosity to test the upconversion technology in situations that go beyond the basic technology and parameter tests. The first section includes the work done together with the Combustion Physics Group at Lund University, where acetylene detection limit measurements was performed on their four wave mixing setup in combination with one of our upconversion units. This unit was designed for image upconversion with a larger beam waist and a different mirror configuration than the module described in this thesis, see [24] for details. The included paper is the primary publication on this work, an Optics Letter from 2014 entitled "Low-noise mid-IR upconversion detector for improved IR-degenerate four-wave mixing gas sensing" [76]. Long spectral scans and further discussion on the noise characteristics are found in the conference contribution [77] included in appendix J and a more general description of the measurements are found in an invited paper in Laser Focus World [78].
The second section includes the work entitled "Upconversion-based long-range CO_2 DIAL measurements" published in Optics Express [79]. This work was

done in collaboration with the Department for Atmospheric Physics at the German Aerospace center in Oberpfaffenhofen. The upconversion unit described in section 4.1 was brought to the DLR labs and tested as a potential future detector technology for their long range gas detection systems. Improved detectivity is needed, in order to change their concentration measurements from integrated path length to being range resolved.
Based on the experiences gained from the application tests, the last section in this chapter will discuss some of the more general issues for the implementation of upconversion technology, and present a suggestion for a second generation upconversion module specialized for long range detection.

5.1 Low Noise mid-IR Upconversion Detector for Improved IR-DFWM Gas Sensing

We compare a nonlinear upconversion detector with a conventional cryogenic InSb detector for the detection of coherent infrared light showing near shot-noise limited performance in the upconversion system. The InSb detector is limited by dark noise giving a 500 times lower signal-to-noise-ratio (SNR). The two detectors are compared for the detection of a coherent degenerate four-wave mixing (DFWM) signal in the mid-infrared, applied to measure trace-level acetylene in a gas flow at atmospheric pressure, probing its fundamental ro-vibrational transitions. Beside lower noise the upconversion system provides image information of the signal, thus adding new functionality compared to standard point detection methods. We further show that the upconversion detector system can be implemented as a simple replacement of the cryogenic detector.

5.1.1 Introduction

Mid-infrared (mid-IR) detectors are applied in a wide range of applications and in a wide range of fields, from surveillance and analysis in the industry to advanced research applications. Most detectors are solid-state devices based on direct detection of mid-infrared light [70] and as a result of inherent thermal radiation, dark counts are often a major noise issue.
Alternative methods based on nonlinear upconversion in periodically poled lithium niobate (PPLN) waveguides have been demonstrated around 1550 nm [17],[80] and 2 µm [81] with high efficiencies, allowing for the use of low-noise visible light avalanche photo diodes (APD) for detection of infrared light. The same principles have been applied for the upconversion of incoherent mid-IR images by Dam et al. [24] using a continuous wave intracavity PPLN mixing scheme.
Given the widespread use of mid-infrared detectors, upconversion detection can have a large impact on areas that work with low-noise mid-infrared measurements. The implementation of the upconversion technology will in most setups be a simple detector replacement, using well-established silicon technology to

detect the upconverted light.
Molecular spectroscopy in the mid-infrared spectral range is attracting growing interest. Especially for gas sensing in relation to energy and environmental applications, due to the unique possibility of sensitive measurements of a long list of crucial molecular species, e.g. C_2H_2, CH_4, OCS, H_2S, HCl, HF, HCN, which otherwise hardly can be detected. For this reason a sensitive and noise-free detection method of signal photons in the mid-infrared are of utmost importance. Spectroscopic methods like grating-based monochromators and Fourier transform infrared spectroscopy (FTIR) are commercially available and applied on a routine basis. For pulsed in-situ measurements, infrared polarization spectroscopy and degenerate four-wave mixing (DFWM) has been used within combustion analysis, and acetylene concentrations down to 30 ppm have been detected [82],[83].
Going to lower concentrations would allow for a more detailed analysis of the combustion processes and at the sub-ppm and ppb levels applications in other fields appear, e.g. breath analysis [84] and explosives detection.
In [85] a pump probe experiment demonstrates 2D IR spectroscopy with upconversion using femtosecond pulses and show that upconversion is a feasible way to detect mid-IR signals in DFWM setups. The setup, however, is highly complicated due to the timing issues.
In [77] the combination of upconversion detection and DFWM was first demonstrated in connection with the improved detection of acetylene. These measurements demonstrated detection of acetylene concentrations down to 3 ppm. However, no quantitative comparison of detector performance and the SNR of the upconversion based system where made relative to traditional cryogenic cooled InSb detectors. Using a setup similar to the one in [24] and [77] this letter quantifies a 500 times improvement in SNR compared to a conventional cryogenic InSb detector, using continuous wave upconversion detection. Furthermore, a threefold improvement, down to 1 ppm in the detection of acetylene concentration is demonstrated, compared to previous results reported with a DFWM setup using upconversion [77] and more than a 10 times improvement compared to InSb based detection. The system is based on nonlinear frequency conversion well-known from second harmonic generation (SHG), and can be realized in a compact fashion using commercially available components.

5.1.2 Experimental Setup

For the benchmark test between the upconversion detector at room-temperature and the cryogenic InSb detector, DFWM is a suitable setup as this is in principle a background free technique and the sensitivity in detection of low gas concentrations is limited directly by the detector sensitivity and noise level. In practical measurements, however, there are always unwanted scattered laser light close to the DFWM signal beam. This was also the case in the current setup, but with the imaging capabilities of the upconversion detector it was possible to decrease the background level significantly as mentioned in [77].
The setup used in the experiment is illustrated in Fig. 5.1 and consists of three sections: the mid-IR light source, the gas tube where the four-wave mixing

occurs, and the dual detection section. The light source [82] is based on a 10 Hz tunable dye laser around 790 nm that is frequency mixed in a $LiNbO_3$ crystal to provide mid-infrared light tunable from 2900 cm^{-1} to 3400 cm^{-1}. This is amplified in a second $LiNbO_3$ crystal to achieve pulse energies of 4-5 mJ. The pulse length is around 4 ns and the linewidth has been measured to be 0.025 cm^{-1} [86]. The beam is passed through a set of BOXCAR plates [83] and split into four beams of equal intensities. Three of these beams are focused to overlap at the center of the flow cell with an estimated interaction volume of (0.4x0.4x10) mm^3. Through degenerate four-wave mixing the three beams will generate a fourth beam when acetylene molecules are present in the interaction volume. This fourth beam constitutes the signal and the residual of the three beams is blocked. The signal beam is then passed on to scaling optics and apertures.

One aperture was placed in the Fourier plane to block high spatial frequency scattering components. A flip mirror directed the signal beam to either the upconversion detector, or the cryogenic InSb detector (J10D-M204-R04M-60, Teledyne Judson Tech.) to reproduce the single detector setup [83]. In the upconversion module the vertically polarized mid-infrared signal beam passes through a germanium window and onto a 5% MgO doped $LiNbO_3$ crystal placed inside a 70 W intra-cavity field at 1064 nm in a Nd:YVO_4 laser. In the PPLN crystal, poled with a period of 22 µm, the mid-IR signal is frequency mixed with the intra-cavity field to generate near visible light around 800 nm. This light is passed through a set of filters, before it is detected by an electron multiplying CCD chip (Luca, Andor Technology). To avoid stray light from background emissions the whole upconversion detector system is sealed in a black box. The beam waist of the mixing laser inside the PPLN crystal is 180 µm, defining the effective detector area. The upconversion module is described in greater detail in [24] with the only change that the pump diode for the Nd:YVO_4 laser has been exchanged with an 880 nm laser diode to separate the pump wavelength from the visible signal wavelength. This will allow for more efficient filtering and thus minimize the 800 nm light reaching the CCD chip as spill light from the pump.

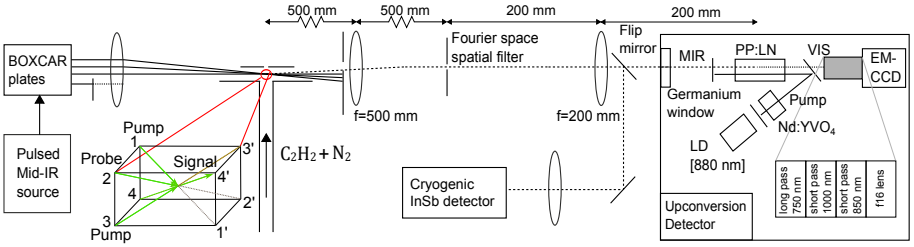

Figure 5.1: Sketch of the full DFWM experimental setup consisting of a pulsed mid-IR light source, a set of BOXCAR plates that splits the beam into four, a gas tube with a diluted acetylene flow and the choice of two detectors for the generated signal.

5.1.3 Spectral Measurements

A measurement was conducted by recording the signal from the gas flow at a given acetylene concentration while the wavelength of the mid-infrared light source was scanned at a rate of 0.05 cm^{-1}/s. For the InSb detector the data acquisition is a straightforward oscilloscope reading. The imaging capability of the upconversion detector [24] is utilized in the data acquisition for the upconversion detector and Fig. 5.2, left, shows a raw image of the upconverted mid-IR signal. A full measurement scan consists of a whole range of CCD frames, each assigned to a specific pulse and wavelength. Each point in a spectrum is thus the sum of the data pixels in a single frame. The data pixels are selected for the lowest concentration to optimize the signal/scattering ratio and this selection is then applied globally to all the measurements. It is not entirely possible to suppress the scattering by pixel selection. Without pixel selection scattering would dominate at low acetylene concentrations [77].

In Fig. 5.2, right, a range of acetylene spectra obtained at low concentrations around the R9e line of the (010(11)ˆ0)-(000 0ˆ0 0ˆ0) band line is displayed. To reduce the effect of power fluctuations from the mid-IR source, each trace is an average of 10 identical sweeps, that each includes all the wavenumbers, as indicated by the first two raw image blocks in Fig. 5.2, left. Furthermore, the background and part of the scattering are removed by subtraction of a reference spectrum acquired with a pure N_2 gas flow. During the scan, dust particles occasionally passed through the beam, causing major single frame spikes in the signal due to scattering. These spikes have been removed by post processing before the spectra was generated, and finally to smooth out the graphs a 10 point running average have been applied on the data. The peaks for the different concentrations do not overlap completely due to wavelength fluctuations

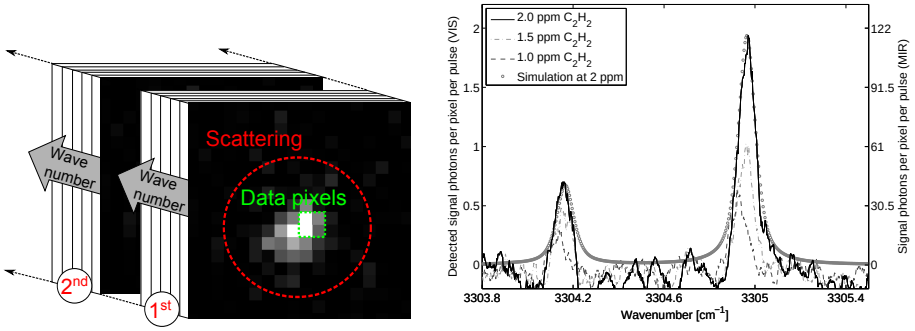

Figure 5.2: Left: Illustration of the raw data image stack that forms the basis for the measured spectra. Each point in a spectrum is the sum of the pixels in a single frame. The displayed frame is a section of the full image and recorded at an acetylene concentration of 6 ppm. Right:Examples of spectra obtained at low acetylene concentrations. Each trace is the average of 10 scans and a running average of 10 points has been applied after the background obtained at 0 ppm has been subtracted. The intensity values are computed from the camera specifications and the right axis is calculated from the inherent loss in the detector system.

of the mid-IR light source that origin from mode-hops and instabilities. As this relates directly to the light source it is relevant for both types of detectors. Overall the measurements correspond well with the gas line simulation from the Hitran 2012 database [87], as seen from Fig. 5.2, right. This simulation is generated with a Voigt line-shape function [83] with a half-width-half-maximum linewidth of 0.06 cm^{-1}. This empirical approach includes contributions from Doppler-, power-, laser linewidth- and collisional broadening [83].
Across short scans the phase matching condition for the frequency upconversion can be regarded constant, but for longer scans it is necessary to tune the temperature continuously during the wavelength sweep. This has been demonstrated in [77].
The detected signal is given as photons per pixel per pulse and in the following the conversion from camera counts to detected photons is described. Specifically, the absolute calibration is computed from the camera counts by comparing the difference in camera counts with and without electron multiplication and the specified well-depth of the CCD without electron multiplication. The dark current is assumed to be 0 which is a good assumption given the dark current of the camera on 0.05 e/pixel/s with an exposure time on 1 ms. The photon number estimation is verified by computing the standard deviation of the camera counts from an unilluminated area of the CCD. This gives a reasonable estimate of the read noise measured in camera counts. From the conversion factor from well-depth estimation, this corresponds to a read noise of 0.5 e. The specified read noise from the CCD in electron multiplication mode is <1 e, thus verifying the power calibration of the camera.
The total amount of detected photons is defined by the selected number of data pixels, in this case four, as shown in Fig. 5.2, left. Without spatial filtering and in the case of no scattering the data pixel area could be extended to include the whole signal area, thus increasing the signal intensity by a factor of approximately 4. To give an understanding of the sensitivity of the upconversion detector in the mid-IR regime, the right y-axis in Fig. 5.2, right, describe the amount of incoming mid-IR signal photons, calculated from the estimated total power transmission efficiency on

$$\eta = \eta_{\mathrm{CCD}} \cdot \eta_{\mathrm{conversion}} \cdot \eta_{\mathrm{filters}} = 0.22 \cdot 0.1 \cdot 0.5 = 0.017 \tag{5.1}$$

where η_{CCD} and $\eta_{\mathrm{conversion}}$ are the quantum efficiencies of the camera and the nonlinear process respectively and η_{filters} is the power fraction through the filter set described in Fig. 5.1.

5.1.4 Concentration Measurements

The line integration of a single gas line, i.e. the area under the peak, obtained from a DFWM measurement is expected to have a quadratic dependence with the gas concentration under optically thin conditions [83]. This is supported by the plot in Fig. 5.3, where the measured line integrated intensity of eight different acetylene concentrations from the upconversion detector and three from the InSb detector are plotted. The data acquired with the upconversion detector are fitted to the equation, $y = ax^k$. A best fit procedure results in

k=1.94 showing a good fit to the expected value of k=2. For the 12 ppm concentration there is a discrepancy for the InSb measurement as this point is close to the noise floor of the detector. The specific acetylene concentrations where calculated from the mass flow meter readings and the used gas concentration. The error bars in Fig. 5.3 represents the standard deviation on the line integrated intensities obtained from ten identical measurements.
The underlying spectra of the three lowest concentrations are shown in Fig. 5.2, right. The horizontal lines on Fig. 5.3 show the standard deviation on the line integration of 10 identical measurements with pure nitrogen flow for the InSb and the upconversion detector respectively. This we define as the detector noise level for each detector and the possible detection limit is the intersection between this line and the quadratic dependency line. From this we can quantify that the upconversion detector has approximately 500 times better signal-to-noise ratio than the cryogenic InSb detector. Due to the quadratic dependency, this translates to a factor of more than 20 in improved detection limit compared to the InSb measurements at hand. Unfortunately, it was not possible to prepare acetylene concentrations below 1 ppm in the current setup due to limitations in the mass flow controllers.
Table 1 shows how the standard deviation on the integrated peak intensities

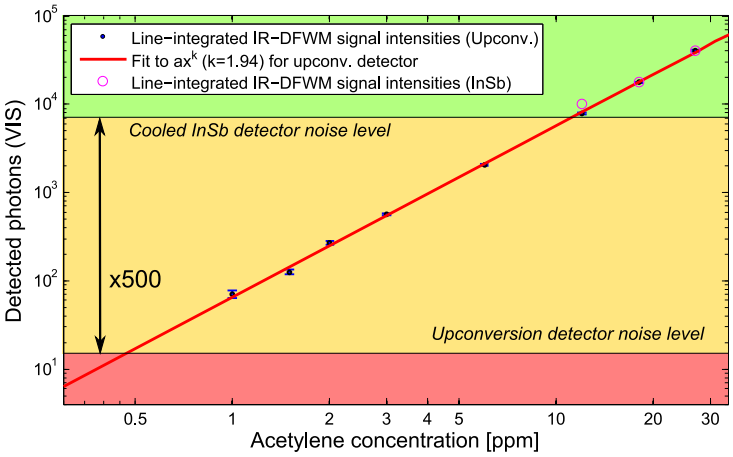

Figure 5.3: Plot of the line integrated intensity of the R9e line of the (010(11)ˆ0)-(000 0ˆ0 0ˆ0) band line as a function of acetylene concentration. The noise levels are computed from the standard deviation on the noise in the two detec-tors. The error bars indicate the standard deviation on the signal intensities.

translates into deviations on the acetylene concentrations. From this we conclude that the upconversion technique is stable and generally performs well in DFWM gas detection. It seems that the precision is limited to 1 %, possibly limited by the laser power fluctuations earlier described. It is possible to use an InSb detector with a smaller detector area and thus a smaller NEP, but this is not recommended due to beam wandering and fundamental alignment difficulties at these wavelengths. In order to get a detailed understanding of the detector performance, a simple comparison of signal-to-noise ratios is not

Table 5.1: Standard deviations of the spectral measurements translated to absolute deviations of the gas concentrations

Concentration C_2H_2 [ppm]	Deviation [ppm] (Upcon. det.)	Deviation [ppm] (InSb det.)
1.0	±0.051(5.1%)	–
1.5	±0.048(3.2%)	–
2.0	±0.055(2.8%)	–
3.0	±0.047(1.6%)	–
6.0	±0.059(0.99%)	–
12	±0.12(1.0%)	±0.43(3.6%)
18	±0.14(0.77%)	±0.51(2.8%)
27	±0.24(0.91%)	±0.33(1.2%)

sufficient. From the experiments it was clear that the InSb detector is limited by the inherent noise equivalent power (NEP=3.0 pW/$\sqrt{\text{Hz}}$) where the upconversion detector is limited by the scattering. This indicates a great potential for pushing the detection limit further down by further suppressing the residual scattering. This could be done by improving the anti-reflection coatings on the optical surfaces, by using higher grade optics in the system or by more efficient filtering and screening. As the upconversion detector is ultimately limited by the signal shot-noise, we expect the system to achieve detection limits that are an order of magnitude better in a scattering free setup. A special feature of the upconversion detector is the inherent limited spectral and angular acceptance bandwidth. For the system at hand, the spectral acceptance bandwidth is calculated, from the Sellmeier equations, to be approximately 6 nm and the monochromatic field of view to be 16 mrad. In high temperature measurements, e.g. under flame conditions, this implies that only a narrow part of the thermal noise is collected, providing a significant advantage compared to conventional cryogenic detectors that both have a large field of view and an acceptance bandwidth that is several orders of magnitude broader.

5.1.5 Conclusion

We have demonstrated that the upconversion detector can be applied as an efficient upgrade to a state-of-the-art low signal mid-IR measurement system. The implementation is a simple detector replacement and further allowing for imaging and corresponding improved spatial filtering. From the quantitative comparison we can conclude that the upconversion system show near shot-noise limited performance while the InSb detector is limited to 500 times lower SNR. This opens for many potential applications where the detection of low level mid-IR signals is critical.

5.2 Upconversion-based Long-range CO_2 DIAL Measurements

For the first time an upconversion based detection scheme is demonstrated for lidar measurements of atmospheric CO_2-concentrations, with a hard target at a range of 3 km and atmospheric backscatter from a range of ∼450 m. The pulsed signals at 1572 nm are upconverted to 635 nm, and detected by a photomultiplier tube, to test how the upconversion technology performs in a long range detection system. The upconversion approach is compared to an existing direct detection scheme using a near-IR detector with respect to signal-to-noise ratio and quantum efficiency. It is for the first time analyzed how the field-of-view of a receiver system, for long range detection, depends critically on the parameters for the nonlinear upconversion process, and how to optimize these parameters in future systems.

5.2.1 Introduction

For a prediction of the rate of climate change during the 21st century, there is an urgent need to better understand the global carbon cycle. This concerns, in particular, the understanding of the processes that control how the most important anthropogenic greenhouse gases, CO_2 and CH_4, flow between the various reservoirs [88].

Currently, there is a significant lack in accurate observations from regional to global scales, needed to infer the fluxes of these important greenhouse gases. A technique that shows potential to provide highly accurate measurements e.g. from ground, aircraft or satellites is the Differential Absorption Lidar (DIAL) technique or its modification, the Integrated Path DIAL (IPDA) [89],[90] applied in the near infrared spectral range. The IPDA technique has proven viable for airborne measurements of integrated path concentrations [90], but a pulsed DIAL system is required to get vertical concentration profiles. This has been demonstrated earlier at 1.6 μm with a near infrared PMT and 5 hours of integration time [91], but much shorter integration times are needed for airborne measurements. The limiting factor to obtain this is the noise properties of the receiver system. There can be four orders of magnitude improvement in detectivity [70] by changing the detection system from an InGaAs PIN-diode to a visible light photo multiplier tube (VIS-PMT) and it is thus an advantage to shift the signal wavelength, from the near infrared to the visible spectral range.

In this work we demonstrate, what we believe, is the first lidar measurement of CO_2 using an upconversion module together with a photomultiplier tube (PMT) to detect the 1572 nm signal at 635 nm. Upconversion is a nonlinear parametric process that provide extra energy to the infrared signal photons by the following energy conservation relation

$$\frac{1}{\lambda_{\mathrm{VIS}}} = \frac{1}{\lambda_{\mathrm{CO_2}}} + \frac{1}{\lambda_{\mathrm{Mix}}} \tag{5.2}$$

In the scope of this investigation $\lambda_{\mathrm{VIS}} = 635\,\mathrm{nm}$, $\lambda_{\mathrm{Mix}} = 1064\,\mathrm{nm}$ and $\lambda_{\mathrm{CO_2}} = 1572\,\mathrm{nm}$. This shift the near infrared photons to the visible region where efficient low noise detectors exist.

We will analyse the advantages and challenges with signal upconversion and discuss how this technology has the potential to improve the sensitivity of CO_2 measurements by orders of magnitude. With an improved sensitivity it will be possible to gather the vertical CO_2 concentration profile and get an extra dimension in the global mapping of the atmospheric greenhouse gas concentrations.

An upconversion based system for long range detection has been demonstrated before for detection of atmospheric aerosols [19]. At a signal wavelength of 1548 nm a 50 mm long periodically poled lithium niobate (PPLN) waveguide was used in a long-wavelength pumped single pass experiment combined with a SI-APD. For the potential use with a CO_2 lidar a high efficiency 2.055 µm intracavity upconversion system shifting the signal to 0.71 µm has been demonstrated in the lab using a 50 mm bulk PPLN crystal [21].

In this paper we demonstrate how an intracavity upconversion system is applied together with a VIS-PMT as the receiver in a pulsed DIAL system for detection of atmospheric CO_2. We measure the on-line and off-line return signals backscattered from a hard target, which in our case is a forest at a distance of $\sim 3\,\mathrm{km}$, and from atmospheric aerosol at a distance of $\sim 450\,\mathrm{m}$. These measurements give rise to, what we believe, is the first analysis of the inherent angular dependency, as an important design parameter for upconversion based long range detection systems.

5.2.2 Theoretical considerations

In efficient long range detection systems the overlap between the field-of-view (FOV) for the transmitted beam and the receiver system are matched. The FOV is defined as the full divergence or acceptance angle for the transmitter and receiver respectively. The conservation of etendue or the angle-area-product is a key relation in the design of the optical receiver. In a long range system the area of the collecting telescope is typically much larger than the area of the detector. When the signal is downscaled, to match the detector, the incident angle increase and it is not unusual with angles close 90°. This works well with the approximately linear angle dependency for conventional detectors, but with an upconversion based receiver system the angular acceptance is strictly limited by the nonlinear parameteric process. This requires a different design of the scaling optics and the FOV may be limited by the upconversion process as displayed in the inset in Fig. 5.4, where a conceptual sketch of the DIAL system is displayed.

The efficiency of the nonlinear upconversion process is given by Eq. (5.3) [92] assuming plane waves, no pump depletion and perfect overlap of the interacting fields.

$$\eta_{\mathrm{up}} = \frac{P_{635}}{P_{1572}} = \frac{8 d_{\mathrm{eff}}^2 \pi^2 P_{1064}}{c n_{1064} n_{635} n_{1572} \lambda_{635}^2 \epsilon_0 A} L^2 \frac{\sin^2\left(\frac{\Delta k L}{2}\right)}{\left(\frac{\Delta k L}{2}\right)^2} \tag{5.3}$$

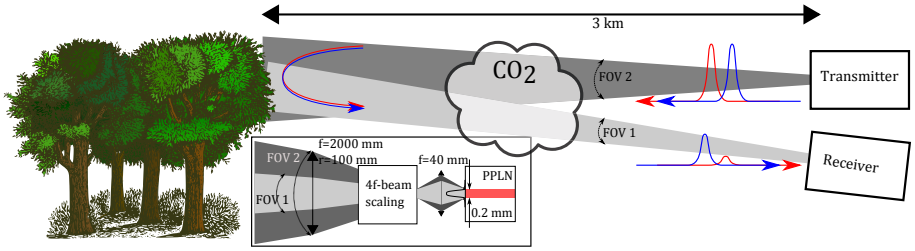

Figure 5.4: Conceptual sketch of the DIAL measurement setup. The inset shows how the upconversion process defines the effective field-of-view for the receiver system.

Where d_{eff} is the effective nonlinearity of the PPLN crystal, P_i the specific power, c the speed of light, n_i the wavelength-specific and temperature dependent index of refraction, λ_{1572} the signal wavelength, ϵ_0 the vacuum permittivity, A is the effective overlap area in the crystal between the pump laser and the incoming signal, L the crystal length and Δk the phasemismatch of the parametric process. Eq. 5.3 is seen to depend linearly on the pump power and quadratic on the crystal length if the upconversion process is phasematched, i.e. $\Delta k = 0$. The phasemismatch is calculated from Eq. (5.4) where Λ_{PPLN} is period of the poling structure in the lithium niobate crystal.

$$\Delta k = k_{1064} - k_{635}\cos\left[\arcsin\left(\frac{k_{1572}}{k_{635}}\sin(\theta)\right)\right] + k_{1572}\cos(\theta) + \frac{2\pi}{\Lambda_{\text{PPLN}}} \qquad (5.4)$$
$$k_i = \frac{2\pi}{\lambda_i} n(\lambda_i, T)$$

Together, Eqs. (5.3)-(5.4) show how the upconversion efficiency depends on the angle, θ, of the incoming light. Assuming a constant temperature, optimized for collinear phasematch, it follows that the efficiency will drop for non-collinear angles and that this defines the angular acceptance bandwidth of the upconversion process. The acceptance bandwidth is specific for the choice of wavelength and decreases for increasing crystal length. PPLN is chosen as the nonlinear material due to the high effective nonlinearity and the large potential for parameter engineering.

In addition to the efficiency of the nonlinear process, the overall efficiency of an upconversion based receiver system, η_{total}, will depend on the efficiency of the visible detector $\eta_{\text{vis.det.}}$ and the overlap between the mixing laser and the signal inside the nonlinear crystal, η_{overlap},

$$\eta_{\text{total}} = \eta_{\text{overlap}}\eta_{\text{up}}\eta_{\text{vis.det.}} \qquad (5.5)$$

where η_{overlap} is calculated as the relation between the signal and mixing laser area. To describe the efficiency when applied for a long range receiver system the angular distribution of the power should to be included in η_{up}. This can be described with a weighted quantum efficiency, defined as

$$QE_{\text{weighted}} = \int_0^{\pi} \eta_{\text{up}}(\theta)\frac{\lambda_{635}}{\lambda_{1572}}\Gamma(\theta)2\pi\theta \mathrm{d}\theta \qquad (5.6)$$

where $\Gamma(\theta)$ is the angular distribution of the incoming power. Together with the conservation of etendue, Eqs. (5.5)-(5.6) form the basis for the optimization of an upconversion based receiver system.

With a 20 mm long PPLN crystal and a pump beam with a diameter of 100 µm, the full width half maximum (FWHM) of the external acceptance angle for the upconversion process is 1.8°. The small acceptance angle together with the small overlap area in the crystal will constrain the design of the rest of the long range detection system and complicate a direct replacement of the InGaAs detector with the upconversion detector. A larger overlap area in the crystal results in a lower conversion efficiency for the collinear part as given by Eqs. (5.3) and (5.4). This can be compensated by a longer crystal, but at the expense of a lower angular acceptance bandwidth. It is, however, possible to find a compromise between the etendue and the QE that justifies the shift of wavelength to the visible regime and this will be discussed in further details in section 5.3.2.4.

5.2.3 Experimental Details

The upconversion detector system is tested using the airborne demonstrator for the French/German MERLIN mission [90] developed at DLR. For the experiments described in the following, the upconversion detection system was set-up side by side to this lidar instrument to allow for a comparison between the direct detection (using InGaAs PIN diodes) and the upconversion approach. An overview of the transmitter and receiver of the airborne demonstrator is found in Fig. 5.5 together with the realization of the upconversion based test receiver setup. The MERLIN demonstrator is based on two optical parametric oscilla-

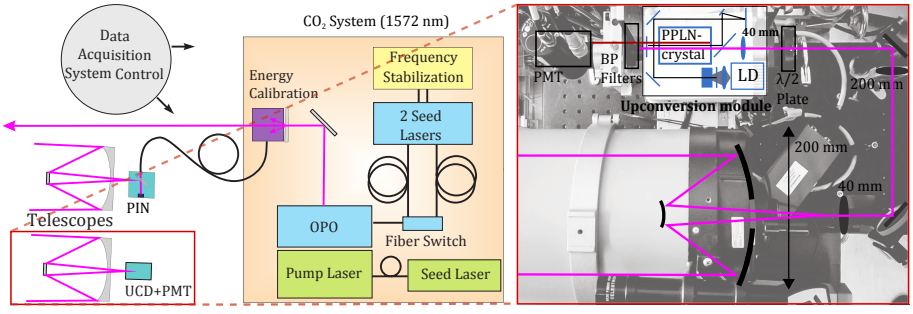

Figure 5.5: Left: Experimental details of the lidar transmitter system with the original receiver system side by side with the upconversion test setup. All IPDA measurements were controlled by the common data acquisition system. Right: Image of the upconversion detection system with diagram overlay. NIR signal → Scaling and guiding → Intracavity upconversion → Visible PMT.

tors (OPOs) which are diode-pumped by means of injection seeded, Q-switched Nd:YAG lasers in a master-oscillator power-amplifier configuration. Originally, the system generates radiation at both 1572 nm and 1645 nm, dedicated to CO_2 and methane, respectively. In the context of this work only the CO_2 part was employed. The IPDA technique requires the generation of two wavelengths

that act as the on- and off-line signals and this is achieved by injection seeding from two stabilized distributed feedback lasers. The system operates in a double pulse mode at 50 Hz and the on- and off-line pulses are emitted with a pulse length of 20 ns and a time separation of 500 µs. For the experiments described the on-line and off-line wavelength were chosen at 1572.0214 nm and 1572.1241 nm, respectively. The single pulse energy exceeded 10 mJ/pulse yielding an average power of ∼1 W. The divergence angle of the transmitted beam was ∼3 mrad. The receiver system in the demonstrator used for comparison uses a 200 mm diameter telescope and a 1 mm InGaAs PIN detector. Further details on the MERLIN demonstrator is found in [90] and for the laser system specifically see [93].

The upconversion based receiver system consists of four main parts: An 8" Cassegrain telescope, beam scaling and guiding optics, the upconversion module, filters and the visible PMT. The telescope has adjustable focus, used for optimization of the signal image in the PPLN crystal. The beam guiding and scaling ensures optimal overlap between the pump and the signal in the PPLN crystal according to the etendue conservation law. An 8f scaling was chosen to give an effective magnification of 250. From the dimensions of the crystal a signal with a 800 µm image, in the crystal, and incident angles up to ±110 mrad is the largest that can pass through the upconversion channel. This translates into an effective FOV close to 1 mrad for the upconversion receiver system. Before the signal enters the upconversion module it passes through a half-wave plate that turns the polarization to match the polarization of the intracavity pump beam, in order to maximize the upconversion efficiency.

The upconversion module are built as a compact, robust and portable unit consisting of a 20 mm PPLN crystal placed in a 1064 nm cavity, to achieve high mixing power. The high finesse mixing laser cavity shown in Fig. 5.5 is build with high reflectivity mirrors (R>99.9% at 1064 nm). For these measurements it typically operates with an intracavity power at 50 W, calculated using a calibrated output mirror. The cavity is designed to have a clear path through the PPLN crystal for an incoming signal, while having two beam waists. $w_{\mathrm{PPLN}} = 100$ µm in the PPLN crystal and $w_{\mathrm{ND:YVO_4}} = 280$ µm in the 5 mm long 0.5% Nd:YVO_4 laser crystal. The PPLN crystal is poled by Covesion in five 1 mm×1 mm channels with periods from 11.8 µm - 15.8 µm. The 11.8 µm is applied for the upconversion of 1572 nm to 635 nm. To control the phasematch of the upconversion process, the PPLN crystal is placed in an oven and the temperature is adjusted to maximize the upconversion efficiency. With a signal at 1572 nm the optimal crystal temperature is measured to 122°C, and the wavelength dependent phasematch acceptance here is wide enough to cover both the on and off resonance wavelength simultaneously. After the upconversion module a VIS-PMT (Hamamatsu R928) is placed behind two OD4 band pass filters with a 10 nm window, centered at 632 nm.

The noise properties and efficiency of the upconversion module is described in [71] and a similar setup using a PPLN crystal with a different poling period has been applied both for low noise point detection and image upconversion of mid-infrared light [76, 24].

5.2.4 Results and Discussion

Long range CO_2 detection is demonstrated experimentally, and the different noise contributions are discussed together with an investigation of the practical challenges in the angular acceptance for the upconversion process.

5.2.4.1 Atmospheric CO_2 Measurements

A forest rising on a hill 3 km away was used as a hard target for the IPDA measurements of CO_2 and the on- and off-resonance data are shown in Fig. 5.6(a), both for the combined upconversion-PMT detector, and for the detection with the InGaAs diode. This demonstrates the first upconversion based IPDA measurement, where the difference between on- and off-resonance signals originates from atmospheric CO_2 in the beam path. The off-resonance peaks are calibrated with respect to the energy reference and normalized to one. The inset shows a comparison of the noise away from the signal peak, giving a ratio of 3.7 between the standard deviations in the two detection systems. This translates into a comparison of the SNR and show that the MERLIN demonstrator is still around 4 times better than the current configuration of the upconversion based system.

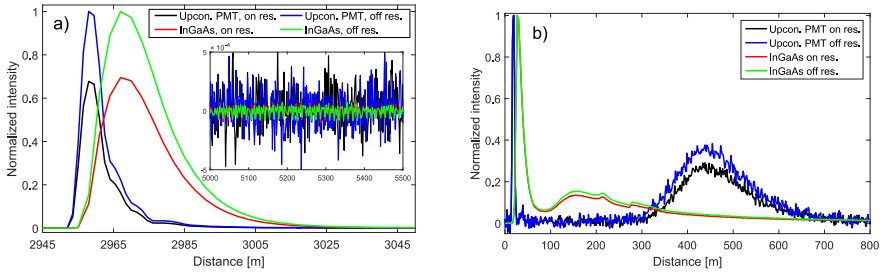

Figure 5.6: a) Backscattered signal from forest on a hill 3 km away from the laboratory. Measured on/off resonance at the 1572 nm CO_2 spectral line. b) Signal from a different alignment configuration optimized for atmospheric backscattered signal. Both plots are averaged over 5 minutes.

The 30% reduction for the on-resonance signal complies with the expected value for a 6 km path in US standard atmosphere at 20°C using the HITRAN2012 [87] spectral line database. The offset of the pulses received by the two detectors is a result of electronic delay difference in the acquisition systems and the different response times for the detectors.

Range resolved CO_2 detection from atmospheric backscattering on a 450 m distance is demonstrated in Fig. 5.6(b), that shows the received signal from a telescope alignment optimized for a signal backscattered close to the transmitter. The intensities in the plot are calibrated to the energy reference peak, first in the plot, but still have arbitrary units and cannot be used for a direct comparison of the different detection methods. It is, however, clear that both methods detect CO_2 in the atmosphere and that an extension of the detection distance requires an improved SNR. It was expected that the PMT signal re-

sembled the InGaAs proximity signal, but due to the angle limitations and the larger separation between the transmitter and the receiver, for the upconversion system, the overlap occurs at larger distances, as seen in the figure.

5.2.4.2 Noise Contributions

DIAL measurements have noise contributions from both atmospheric scattering of sunlight and the inherent dark noise in the detector. This is also the case with the combined upconversion module and PMT system, but there are three important differences.

- Due to the change in wavelength from infrared light to visible light the inherent detector noise will be lower in the case with the visible PMT compared to the InGaAs detector. This improvement can be as much as four orders of magnitude [70].
- The limited acceptance bandwidth from the phasematch condition in the upconversion process function as a $< 1\,\text{nm}$ bandpass filter. This, in combination with conventional bandpass filters after the upconversion module; give a very low background level. With a bandstop filter at 632 nm before the upconversion, inverse of the bandpass filter after the upconversion, the atmospheric noise contribution can be reduced further.
- Different noise sources are inherent for the upconversion process: A low amount of upconverted thermal photons [24], upconverted Raman scattering [17] and upconverted spontaneously parametric downconverted (SPDC) photons [7]. In this case, the upconverted SPDC photons are the only noise source overlapping with the signal frequency and it cannot be filtered away effectively. At the given spot size and power levels the effect on the SNR are, however, limited [71].

Fig. 5.7(a) show, a comparison of the three noise contributions in the specific setup and confirm the expected low noise contributions from both the atmosphere and the upconversion process. The plot b) is included as an example of the SNR in a direct measurement of the backscattered signal from the forest.

5.2.4.3 Angle Dependency

The change to an upconversion system results in largely improved noise specifications and collinear tests, of the upconversion module, with a $637\,\text{kW/cm}^2$ mixing field show QE>80 %. Still it is seen from Fig. 5.6(a) that the SNR is lower than with the direct InGaAs detector. For long range measurements this is a result of a decreased QE. From the theoretical description in section 5.3 and the configuration of signal area and angle described in section 5.3.1 the QE is estimated to be <1 %. With long range applications the angular dependency is critical due to the angular spread of the signal, pointing stability issues and alignment practicalities.

To investigate the angular challenge, a measurement of the backscattering from the forest was done with a thermal gradient applied over the PPLN crystal.

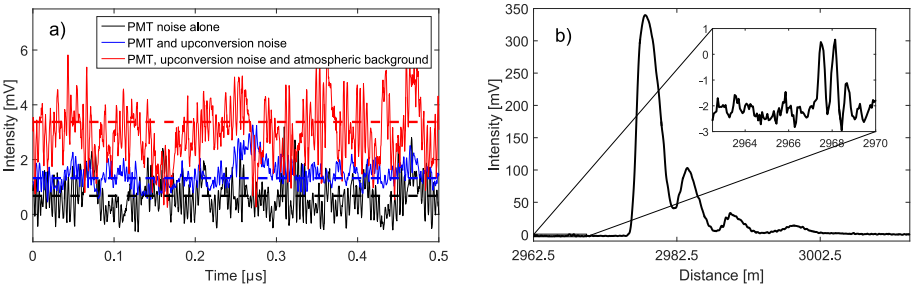

Figure 5.7: a) A comparison of the different noise contributions in the combined upconversion and PMT detector. b) Example of a backscattered signal from nearby forest, illustrating the SNR for the combined PMT and upconversion detector. The oscillations after the main peak are not backscattered signal, but relaxation oscillations from the PMT. The inset show an example of the background noise. All data is an average over 32 pulse sweeps and the intensities are given as output voltages from the PMT.

This is demonstrated in Fig. 5.8(a), where the plot show a backscattering measurement with and without the gradient applied and the peak at 2174 m show up uniquely on the measurement with the gradient applied. This indicates that the acceptance angle is expanded and now picks up signal from a part of the forest on a lower part of the hill closer to the receiver. The inset in Fig. 5.8(a) shows a thermal measurement of the crystal from above. The linear gradient at 9 °C is applied passively by replacing the brass crystal mount with one made of Teflon, designed with a thermal bridge of aluminum to the underlying heater in left end of the crystal. The gradient results in changing phasematch conditions throughout the crystal and thus expands the angle acceptance at the expense of a lower the QE. This is demonstrated both experimentally and theoretically in Fig. 5.8(b) where different configurations are computed and compared with acceptance angle measurements both with and without a thermal gradient. The measurements are performed by rotating the whole upconversion module in a test setup with a uniform oversize signal illumination of the PPLN channel. The upconverted power was monitored upon rotation and both measurements are calibrated equally to the computation without a gradient.

In Fig. 5.8(a) the consequence of a larger acceptance angle is demonstrated with the long range IPDA setup. A second peak occurs at ~ 2180 m, only with the thermal gradient applied, originating from trees, now within the receiver's field of view. The signal level for the main peak drops only $\sim 10\%$, even though the QE for the collinear conversion is reduced by a factor of 4. Phasematch expansion in PPLN have previously been realized in [94] where the emission spectrum of a mid-IR light source was expanded through active control of a thermal gradient.

To investigate the implementation of a thermal gradient further, a plane-wave simulation based on the coupled equations for parametric interaction [92] was established. This model allows for calculations of the phasematch for different wavelengths and angles, when the temperature varies throughout the crystal. Fig. 5.9 shows simulation results of the relation between the accep-

tance angle and the QE, with respect to the influence of a linear temperature gradient, or a linear chirp of the poling structure in the crystal. The computation was done with a crystal length of 20 mm, a poling period of 11.8 µm, a beam waist of 100 µm and a mixing laser power of 200 W at 1064 nm. This translates to a mixing field intensity on 637 kW/cm^2. In the case where the phasematch is optimized for collinear conversion, the angle acceptance curve will look like Fig. 5.8(b), with one central lobe that broadens, when a gradient is applied. In Fig. 5.9, the off-set temperature, at the one end of the crystal, is optimized for non-collinear interaction and the optimum is found to be 6°C lower than the temperature optimal for the collinear phasematch. This results in a double acceptance peak in the case without a gradient and then more regular acceptance curves for higher gradients, see Fig. 5.9(b). In Fig. 5.9(a) it is seen how the acceptance angle increases for higher gradients, but also how the average QE does not reach the optimized collinear level. The stepwise behaviour of the acceptance angle growth occurs as the phasematch at larger angles grow higher than the existing peaks at lower gradients.

The weighted efficiency, stated in Eq. 5.6, is plotted in Fig. 5.9(c) for increasing temperature gradients. Three different angular distribution widths are treated, each showing an optimum gradient around 6 °C. With more power confined in the small angles of the incoming field the overall QE would be higher, but as discussed earlier collinear confinement is not possible in the case of long range detection. The upper limit for the incoming angles results from the geometric bounds of a 20 mm long crystal with 1 mm×1 mm poling channels where angles larger than ±110 mrad will not overlap with the poling structure for the full length of the crystal.

Chirped poling structures are an alternative to the temperature gradient and the use of such crystals is demonstrated in [95] and calculation of bandwidth expansions are presented in [96], with results that agrees well with the conclusions of our temperature gradient calculations. In Fig. 5.9 it is seen that an absolute chirp of approx. 30 nm matches a 10°C temperature gradient.

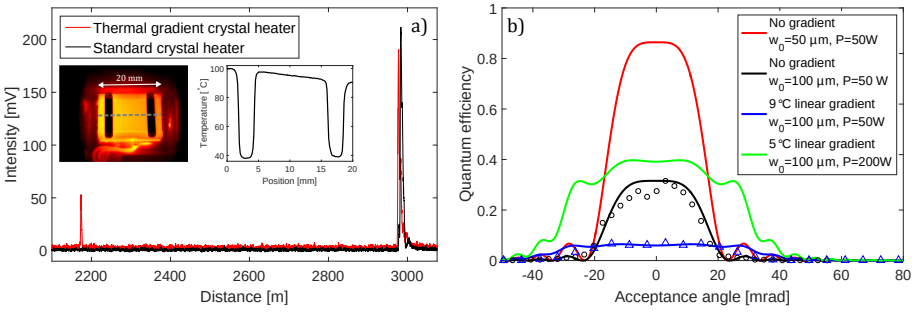

Figure 5.8: a) Comparison of the backscattered signal with and without a gradient applied over the PPLN crystal. Inset show an example of a crystal with a passive gradient applied together with the corresponding surface temperatures. b) Computation of the angular acceptance for the upconversion process together with measurements normalized to fit the no gradient case. Beam waist values and mixing field powers for the simulations are included.

This mean that the maximum increment from the first to the last period in the chirped structure should be 30 nm. Such a fine chirp is not possible to resolve with present day poling procedures, and thus the temperature gradient method is preferable.

5.2.4.4 Future Improvements

The system at hand is very experimental and built from available equipment. In an improved version of the upconversion scheme following the best case in Fig. 5.9(c) the mixing field is increased to 200 W giving 4 times higher QE or 2 times larger beam waist for the same QE, but larger overlap with the incoming signal. The visible detector could be replaced with a high QE SI-APD, or a higher QE PMT, giving a factor of 2 improvement. All these improvements would apply for both IPDA and DIAL measurements. For the DIAL measurements specifically, the detected signal would rise significantly if the transmitter beam was better collimated. The divergence can be at least four times smaller, thereby matching the receiver system better. This would give an signal in the crystal of half the size and an incoming signal with half the angular spread, increasing the overall QE by a factor of 12. With the larger acceptance angle and higher QE the background noise from the atmosphere and the upconversion process could rise as well. The increased atmospheric background can be handled by a narrow band filter before and after the upconversion and the increase in noise from the upconversion process itself can be limited following the procedure for mixing intensity optimization in [71]. When all the above is taken into consideration, it is expected that the SNR of the optimized upconversion system could show an improvement of two orders of magnitude. The improved QE may allow for range resolved concentration measurements of atmospheric CO_2, with much shorter integration times than demonstrated in [91]. In a future integrated implementation of the upconversion system, the beam scaling optics will be configured to match the nonlinear

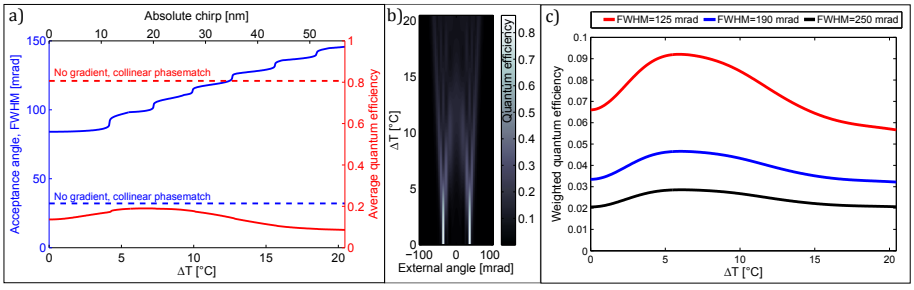

Figure 5.9: a) A computation of the angular acceptance bandwidth for the upconversion process and the average QE for different values of linear temperature gradient or linear chirp of the poling pattern. b) Overview of the angular dependent QE for different temperature gradients. c) Weighted efficiency for the upconversion process calculated with respect to the temperature gradient, shown for three different angular distribution widths for the incoming signal. All plots are obtained for a mixing laser intensity of 637 kW/cm^2 and a off-set temperature 6°C below the collinear optimum.

process. The shift in technology would only marginally increase the overall system complexity, adding a compact $14\times11\,\mathrm{cm}^2$ upconversion module and an associated power supply.

An improved upconversion system applied in a DIAL configuration shows much promise for vertical profiling of atmospheric CO_2, as well as other greenhouse gases, such as methane, with slight modifications to the upconversion module.

5.2.5 Conclusion

It was demonstrated, for the first time, how upconversion in combination with a visible photomultiplier tube can be used for long range detection of atmospheric CO_2. Measurements showed good noise properties for the combination of upconversion and visible detector technology, but also a limitation in angle acceptance and QE for the given upconversion system. With experiments and models with thermal gradient control it is analyzed how to improve the upconversion technology for long range detection.

Given the large potential in the detectivity for the visible detectors, we believe that the upconversion technology has the potential for reaching new frontiers in range resolved, long range atmospheric gas measurements. This holds true for the NIR wavelengths, and at longer wavelengths, where the discrepancy in detector noise, compared to visible detector technology, increases, the benefit of upconversion technology is even more significant [76].

5.3 Summarizing Discussion

The selected applications are examples, where the upconversion technology in combination with visible light detectors replaced conventional semiconductor based IR detectors for point detection of monochromatic coherent light. Upconversion imaging and spectral analysis based on the inherent angle specificity in the parametric processes also show promising potential, e.g. [26], but it is out of the scope for this thesis to treat this subject in further detail.
As expected the largest advantage of the upconversion technology was gained in the acetylene detection application with the MIR signal, presented in section 5.1. Here the conventional state-of-the-art detection was improved 500 times and the limitation was not the upconversion detectivity, but the background laser light scattering. In this case, the imaging capability was a great help in the data analysis and the optimization of the setup. In a future optimized setup, an upconversion system for point detection could be applied to get higher upconversion efficiency and a much simpler data acquisition procedure, without the need for manual pixel selection. In this case the USPDC noise could be a challenge, but from the simulations in section 4.2.1 it seems that the USPDC noise drops of for longer wavelength conversion as the phasematch for the SPDC drops significantly. This is showed in the simulation for the 11.8 µm in figure 5.10. Furthermore, the measurements described in section 4.3.2.1 proof, that the RDC errors are relatively smaller on longer grating periods, see appendix H. A simulation for a 22 µm poling period with 6 % poling errors is included in figure 5.10, showing that the amount of expected USPDC is close to two orders of magnitude lower in the case of MIR upconversion. This might also explain why the USPDC noise is not observed by Dam et al. [24].

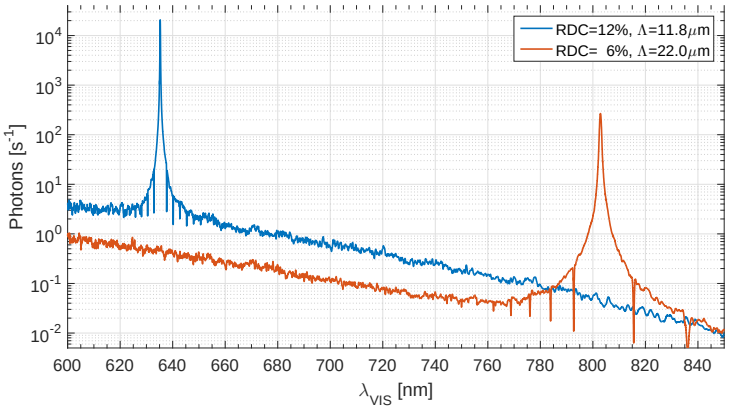

Figure 5.10: Simulation of the rate of generated USPDC noise photons for two different poling periods and RDC error magnitudes. Both simulations are performed at a PPLN temperature at 130°C, 637 kW/cm^2 mxing field intensity and plotted as the mean value of 100 different runs each with a unique set of RDC errors.

Even in the competition with a carefully engineered detection setup and a signal at the NIR wavelengths, the upcovenversion technology proofed only 4 times worse performance in the long range detection of atmospheric CO_2 in section 5.2. In this case, the limiting factor was not the noise or the direct efficiency of the upconversion process, but the fundamental acceptance angle limitation in parametric processes. It was not expected that the upconversion technology would be advantageous in the region of telecommunication, but after the test at DLR it seem that the upconversion technology indeed have a potential even for long range detection of atmospheric gases.

With these promising results, few things should limit the upconversion detector technology from widespread use, but several issues limit the adaption process. Compared to semiconductor based detectors, the extra step adds considerable to both the complexity and the size of a detector. From being a simple component, with small alignment requirements, even a highly optimized and standardized upconversion unit would require careful alignment of the overlap and both an additional power supply and a control unit. If the upconversion unit, furthermore, should be as versatile as a conventional detector, the complexity would rise further and demand control over at least one phasematch tuning parameter. Additional constraints occur from the angle, wavelength, and the polarization dependent nature of the upconversion process, that require specific designs for each application. Regarding the more practical considerations, an intracavity based upconversion unit would be much more sensitive to vibrations and temperature fluctuations, and the price of the unit could exceed the saving by changing to the visible regime. For all the above reasons, the upconversion technology will probably not replace the infrared detectors in general. However, for high sensitivity scientific purposes, where complexity is not an issue, and for OEM use where the specificity is not a problem, the potential is substantial.

5.3.1 2nd-generation Upconversion Unit for Long Range Detection

In section 5.2, in the upconversion DIAL paper it was mentioned briefly how a future system could be optimized to beat the SNR of the MERLIN demonstrator and hopefully perform range resolved measurements of the atmospheric gas concentrations. This section will describe thoroughly how such a system can be designed and how it may perform. The overall optimized system is presented in figure 5.11 and the seven different optimization points is described in the following paragraphs.

40 mm Crystal A two times longer crystal would improve the upconversion efficiency by a factor of 4, following equation 2.8, but the FWHM with respect to the acceptance angle would be reduced a factor of $\sqrt{2}$ following equation 2.18. This could be expanded to even longer crystals, but long PPLN-crystals are costly and 40 mm is the largest length commercially available.

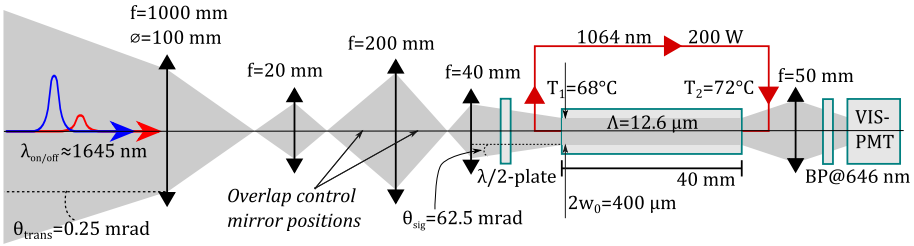

Figure 5.11: Suggestion for an optimized upconversion based receiver setup for long range detection of atmospheric methane. The drawing is not to scale and the mixing laser cavity mirrors and pump diode are omitted for simplicity.

Increased Mixing Field Power Going from 50 W to 200 W of mixing laser power, the QE would increase by a factor of 4. This could be achieved either by increasing the finesse of the cavity or by increasing the pump power. The finesse could be increased if the cavity was designed to fit better with the 45° mirrors. Another challenge for the finesse is the spot size at the point where the beam pass the D-mirror, here the beam waist is $< 300\,\mu m$, and given the tolerances in the cavity this makes it hard to align without cutting a part of the beam by the D-mirror edge.
The pump power for the mixing laser could be increased with a more powerful laser pump diode. An 8 W 808 nm diode was implemented in the current system and the intracavity power came close to 200 W before a hole was burned in the Nd:YVO_4. A full reassembly was required and several attempts to reestablish the high intracavity power in different configurations failed. Due to lack of time and components, further tests was canceled and the work continued with an intracavity power on 50 W following the old configuration.
In future configurations, it is advised to consider possible reflections back to the diode and thermal lensing in the laser crystal. The influence from the thermal lensing could be avoided with a longer crystal with a lower doping level or by changing to an AR/AR coated crystal and a seperate end mirror. A third option would be to change the laser crystal to a Nd:$GdVO_4$ that have thermal properties that are very suitable for high power diode-pumped lasers [97].

Increased Mixing Field Beam Waist Increasing the beam waist to $w_0 = 200\,\mu m$ will match the size of the signal when scaled the 50 times down from a telescope diameter on 100 mm. Following the conservation of etendue a larger mixing field beam waist generally relaxes the acceptance angle constraint. With a 200 W mixing field the intensity is 160 kW/cm^2 which is double the optimal intensity, found in section 4.3.1, for a 40 mm crystal. However, with a thermal gradient applied, the overall QE will drop significantly and presumably move the optimum towards higher intensities.

Improved Filtering Currently two standard OD4 10 nm wide bandpass filters is used, specified to a center wavelength at 632 nm. From the noise analy-

sis in section 4.2 and figure 4.5, specifically it is clear that all the upconverted SPDC cannot be filtered away, but if a sub-nm bandpass filter was designed and implemented, the contribution from the pedestal and the flanks of the peak would be reduced. An bandstop filter with the inverted specifications could be implemented before the upconversion module, in case atmospheric noise at the visible wavelengths passed directly through. A discussion of the use of a prism pair, a holographic transmission grating or a volume bragg grating as filters for upconversion noise is found in [18]. These methods can typically achieve a narrower bandwidth than the standard dielectric fiters and the prism pairs have the advantage of being tunable, but they also add complexity to the setup. The volume Bragg grating specified has the smallest acceptance bandwidth at 24 GHz, but it is still wide enough to allow for transmission of both the on- and off-resonance peak [89].

Active Thermal Gradient Changing from a passive to an active thermal gradient would allow a verification of the computations for the gradient and acceptance angle dependency. For the more practical part, it would be much simpler to adjust the actual gradient to the optimum value. In the current setup the tuning of the gradient size was done through trial and error with different thicknesses of steel. A thermal model of the gradient heater was performed in SolidWorks, but it was complicated to include the correct thermal properties and the model did only give a rough estimate. A downside of an active gradient would be the risk of inducing mechanical tension and break the crystal, if the gradient control failed and either turned the gradient up too high or too fast.

Smaller Telescope In the DIAL measurements using backscattering from atmospheric aerosols, most of the light is scattered back against the transmitter at an increased divergence angle [98]. The amount of received signal photons will thus scale with the angle-area-product or etendue. In the case of an upconversion based detector the etendue is limited by the parameters for the nonlinear process, and this requires the right balance between conversion efficiency, divergence angle and telescope size. In order to optimze this balance for the second generation of the detection system, it is suggested to reduce the telescope diameter by a factor of two and use a 100 mm telescope. With a poling channel size of 1 mm$\times$1 mm, the $1/e^2$-signal diameter should not exceed 800 µm and a phasesmatched limited FOV of 125 mrad. This translates to a telescope size of 100 mm and an corresponding FOV on 0.5 mrad.

Tighter Transmitter Focus As described in 5.2, the current DIAL system is optimized for integrated path measurements and the transmitter have a FOV on 3 mrad that result in a ø=30 m spot on a 10 km distance. This is done to ensure sufficient averaging of the surface reflectance variation when measuring the integrated path concentrations from an aircraft. In case of range resolved DIAL measurements, the high intensity from a narrow collimated beam would be ideal, but the system design is currently bi-static and for practical reasons it is not possible to obtain good overlap if the FOV is less than 0.5 mrad. This would still be 6 times better than in the current design and would alone allow

for approximately 10 times more light to be accepted by the upconversion process following equation 5.6. In a complete redesign of the system a mono-static approach could be considered, where a collimated beam could be used while keeping the overlap. This would give a large reflection from the transmitter, but it may be separated in time as the system operates with nanosecond pulses on kilometer distances and with a low repetition rate.

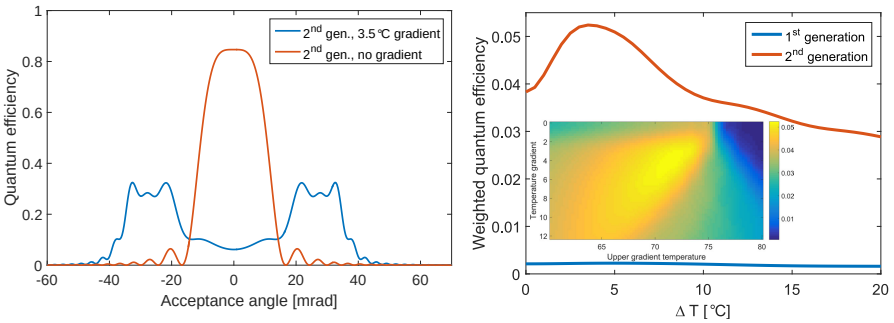

Figure 5.12: Left: Computation of the phasematch dependent angle accemptace for the upconversion process in the second generation module in case of gradient and no gradient. Right: A comparison of the weighted QE for the implemented first generation detection system and the second generation proposal. Inset show an overview of the optimization process for identification of the optimal size and end temperature for the thermal gradient across the 40 mm PPLN crystal. The plots are made for the methane system, but the change in wavelength does not affect the effective SNR noticable.

From the above description of all the system improvements, the second generation would improve 160 times on the SNR compared to the upconversion detector based system demonstrated at DLR currently. The DLR system is 4 times better for now which will result in a 40 times improvement going from the conventional MERLIN system to the upconversion based system. The contribution from the increased crystal length, the increased mixing power, the new gradient, and the reduced FOV, can all be included in the computation of the weighted efficiency for the upconversion process, collected in equation 5.6 and plotted for the second generation module in figure 5.12 to the right. This accounts for a factor of 20 improvement, and from using a smaller telescope and increasing the mixing field beamwaist, a further improvement on 16 times is achieved. On the down side the smaller telescope will cause a 4 times decrease in collected photons, assuming a homogeneously signal field. The last factor of 2 can be obtained from using a PMT with double quantum efficiency, such as a Hamatsu R9880U-20. A discussion on the use of PMT's or APD's is found in the next section.
Further improvements of the noise figure may be obtainable by selecting the right crystal with a poling period with a set of RDC-errors, that give low noise exactly at the signal wavelength, following the conclusions on figure 4.16.
Another approach to see the potential of the upconversion system is to compare the detectivity of a InGaAs detector with the VIS-PMT directly. From

[70] this amounts to at least three orders of magnitude advantage for the VIS-PMT, but the QE is approximately 5 times lower and the overall efficiency for the upconversion process would be around 5 %. The amount of detected signal photons decreases thus two orders of magnitude while the noise decrease three orders of magnitude. This rough estimate on a 10 times improvement is not too far from the improvement estimate from the DLR measurements and confirms the large potential for the upconversion technology.
The improvement from the thermal gradient only amounts to a little more than a single percent point, because the incoming angles are now smaller than in the first generation system. The inset in figure 5.12 shows the specific optimization procedure, that tested the weighted QE with respect to the gradient size and end temperature. The same procedure was used to find the 6°C offset in section 5.2. For the 2nd generation the optimum high temperature for the gradient is 3.8°C lower than optimal temperature for typical collinear phasematching. A comparison of the phasematch dependent angle acceptance is displayed in figure 5.12 to the left, and the shape is a consequence of the angular distribution of the incoming signal where most of the signal photons are found at the larger angles following from the solid angle integration in equation 5.6. The complicated change of the angular phasematch also indicates, that the potential gain from a gradient may be larger than computed, as the actual phasematch dependency or incoming signal distribution may be different than assumed in the calculations. This could be optimized, if an active gradient was implemented, easiest optained with a double Peltier element that can heat up to 115°C at room temperature which is enough to reach phasematch for the methane line with a poling period on 12.6 µm. This poling period would allow for phasematching of the sum-frequency generation between 1064.5 nm and 1645 nm, at a PPLN temperature of 75.8°C, giving a visible signal at 646 nm.

It is the hope and the belief, that the second generation system would proof capable of demonstrating range resolved measurements of atmospheric methane on distances, up to several kilometers. If the upconversion principle is proofed as a viable technology for future measurement systems, a more integrated design with the transmitter would be advantageous for alignment and stability.
A fully integrated system may even utilize the pump for the MERLIN signal beam OPO is a 30 ns 75 mJ pulse exactly at 1064 nm [93], corresponding to the mixing laser wavelength for the upconversion process. Translated to a peak power this amounts to 2.5 MW and if this can be coupled into a 100 m long optical fiber and tapped 1 %, each round the leak pulse could be used as a single pass mixing laser field for the backscattered light. This allows for a much simpler upconversion system only consisting of a PPLN crystal and some filters, and give a range-gated-signal at the same time. The crystal could be shorter and the mixing beam waist larger improving the weighted QE, and an unpoled crystal could possibly be used to reduce the upconversion noise. It would however be a challenge to find an optical fiber that could withstand the high power levels.

5.3.1.1 PMT or APD

The choice of a Si-APD in combination with the upconversion module is the obvious choice, as the Si-APD has high gain, high QE, is fast, and very simple to use as a replacement for the InGaAs PIN or APD detectors. In the NIR region, however, the difference in detectivity for state-of-the-art detectors are not very large due to the small difference in thermal noise and the large amount of electronic Johnson-Nyquist noise, apparent for both technologies. For this reason the real jump in detectivity occurs when changing to a wavelength where the visible PMT's are sensitive [70]. Here the three orders of magnitude in detectivity originates from the total absence of electronic noise in the light-matter-interaction and the following amplification. The QE is lower, it requires a high voltage power supply and, the detector is more bulky, but in comparative SNR tests in the visible few photon region, the PMT's beats the SI-APD's. See Agishev et al. for a LIDAR based comparison [99] and the Hamatsu guide to choosing the right detector for a more general comparison [100]. In figure 5.13 an qualitative overview of the pros and cons for the two detector types are included.

SI-APD's	VIS-PMT's
⊕ High gain	⊕ High gain
⊕ Simple operation	⊕ Photon noise limited
⊕ High QE (~80%@646 nm)	⊕ Fast (<ns rise time)
⊕ Immune to EM-fields	⊕ Large active area (>8 mm^2)
⊖ Johnson-Nyquist noise	⊖ Require high voltage
⊖ Small active area (<0.5 mm^2 if <ns rise time)	⊖ Low QE (~15%@646 nm)
	⊖ Sensitive to EM-fields

Figure 5.13: Overview of the pros and cons for typical high-end SI-APD's and VIS-PMT's. For the QE and area values, a Hamatsu S12023-02 and a R9880U-20 is used as examples for the APD and the PMT respectively. Note that the EM-field immunity is not relevant in this context, but included for completeness.

If the methane detection systems was pumped e.g. at 1.9 µm, the upconverted signal ends at 881 nm where the PMT's are not efficient anymore. The APD is thus the only possibility of the two. A comparison of the extra USPDC noise in the short wavelength systems and the difference in noise between an APD and an PMT have not been made. For the low intensities suggested for the long range detection systems, I believe that the short wavelength pumping in combination with a PMT is preferable. This may also change the belief that long wavelength pumped upconversion systems in general are superior to the short wavelength systems [72]. The situation might be different if the APD can be operated in Geiger mode, which is typically much lower in noise, but further investigations are required.

CHAPTER 6

Outlook and Conclusion

6.1 Outlook

Based on the experiences gained throughout the thesis, this outlook presents suggestions on how to continue to bring parametric devices for novel use and give to new scientific insights. The OPG from section 3.2 could be tested with a larger bandwidth design, possibly in the long infrared wavelength regime, and compared with a super continuum light source for spectroscopic applications. The OPA in section 3.3 could be tested in the proposed configuration with a tunable quantum cascade laser. This could work as a light source for a compact parametric mid-infrared gas detector.

Tests of the upconversion technology as a replacement of infrared point detectors could be extended to the long infrared region. This would require a transparent crystal in the long wave infrared region such as an $AgGaS_2$, which then requires a longer wavelength mixing laser. Such a system could be based on the 1.9 µm intracavity laser presented in section 4.3.3 and work as an upconverter for 6-11 µm light where spectral analysis of e.g. explosives could be an application.

In continuation of the work done on the upconversion based DIAL system in section 5.2 the next step could be to implement the recommendations for the second generation system, described in section 5.4.1. This optimization require work on both the laser cavity design for the upconversion system and more fundamental work on the noise and the efficiency with long range upconversion detection. The cavity can be improved with a higher finesse, a larger intracavity field and a simpler mechanical design. A fundamentally different approach to simplify the cavity design, and keep control of the two important beam waists, could be an intracavity lens system for beam scaling. The overall long range system design need a thorough analysis and feasibility study of a full integration of the upconversion technology in a range-resolved DIAL system for methane detection.

More fundamentally, the experimental and modeling investigation done on the USPDC noise in section 4.3.2 could be continued and expanded. This could include: Implementation of Raman scattering in the noise models, higher resolution noise spectra measurements and accumulated noise measurements with respect to varying mixing laser wavelengths.

6.2 Conclusion

The goal of this thesis was to investigate different applications of parametric amplification for low noise detection systems, e.g. infrared gas spectroscopy. This resulted in construction and test of two light sources, a compact upconversion module and two tests with infrared gas spectroscopy.
The light source testing gave some interesting results on mid-infrared seeded optical parametric amplifiers. This approach could be a good solution for tunable mid-infrared light sources where the large gain from the PPLN crystal could be combined with the tunability and stability of a semiconductor mid-infrared laser, used as a seed. For the current project, it was concluded that further development of the light source technology would require to many resources compared to the possible novelty and present focus of the work in the group. The light sources proved fine for initial application testing and investigation of the parametric principles in the infrared, but for more sophisticated light sources it was decided to use those of corporation partners.
The second part of the project was an investigation of the upconversion process for low noise detection of infrared signals. With the offset in the compact parametric conversion module, the important features of an upconversion system was investigated. Quantum efficiencies above 80 % was demonstrated and a wide tunability allowed for upconversion of both mid- and near-infrared signals. The most central part of the detector investigation was measurement and modeling of the generated noise photons from the upconversion process. This noise was measured both in the spectral and the spatial regime, and two different models were constructed in order to verify the origin of the different noise sources. It was concluded that the primary source of noise, not possible to filter away, is the upconverted spontaneously parametric downconverted noise and that the amount of generated photons from this process depend crucially on both the size and the specific set of the random duty cycle errors on the periodically poled lithium niobate crystals.
It was demonstrated how the signal-to-noise ratio for an upconvertion based detector system can be optimized by balancing the quantum efficiency and the generated noise through the intensity of the mixing laser. Another approach to limit the noise would be to select a crystal with a specific set of random duty cycle errors, that generates few noise photons at an application specific wavelength.

Two applications of the upconversion principle for detection purposes was tested. Together with the Combustion Physics Group at Lund University an upconversion module was demonstrated to improve the detection limit for acetylene in a four-wave-mixing process by a factor of 500, where the final limit was not set by the upconversion module.
A collaboration with the Department for Atmospheric Physics at the German Aerospace center resulted in a the demonstration of the first upconversion based long range detection of atmosperic CO_2, and the constructed upconversion module proved here capable of external application testing. This test gave rise to an investigation of the constraints that the phasematch, of the upconversion

process, induce on the field-of-view for long range detection systems. A design for a specialized system for this purpose was suggested as a second generation module, that keeps the noise low and the quantum efficiency reasonable high.

The parametric amplification indeed showed capable for use with both light sources and detection systems for low noise infrared detection. This thesis demonstrates that there is a large potential of novel applications within upconversion based gas spectroscopy and that a range of fundamental investigations of noise and parametric efficiency are open for future investigations.

APPENDIX A

List of Abbreviations

APD	Avalanche photo detector
CW	Continuous wave
DFG	Difference frequency generation
DWFM	Degenerate four wave mixing
DIAL	Differential absorption LIDAR
EM-CCD	Electron multiplication charge coupled device
FFT	Fast Fourier transform
FOV	Field-of-view
FWHM	Full with half maximum
LIDAR	Light detection and ranging / Light radar
MIR	Mid-infrared
NEP	Noise equivalent power
NIR	Near-infrared
OPA	Optical parametric amplifier
OPG	Optical parametric generator
OPO	Optical parametric oscillator
OSA	Optical spectrum analyser
PMT	Photo multiplier tube
PPLN	Periodically poled lithium niobate
QE	Quantum efficiency
QPM	Quasi-phasematching
RDC	Random duty cycle
SBS	Slab-by-slab
SNR	Signal-to-noise ratio
SPDC	Spontaneous parametric downconversion
USPDC	Upconverted spontaneous parametric downconversion

APPENDIX B

Overview of Poling Periods and Datasheet Example

NIR SFG crystal: (11.8, 12.8, 13.8, 14.8 15.8) µm

MIR SFG crystal: (21.0, 21.5, 22.0, 22.5, 23.0) µm

OPG/OPA crystal: (29.52,29.98,30.49,31.02,31.59) µm

Covesion Ltd. Unit A7, The Premier Centre Premier Way, Romsey, Hampshire, SO51 9DG www.covesion.com	Device Specification – MLN_SFG(1064-3300) 1mm Thick	covesion

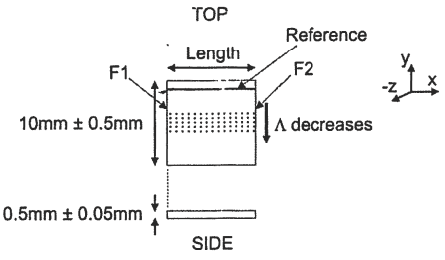

[Image for reference only. Not to scale.]

Dimensions: Thickness(z) = 1.0mm±0.05mm, Width(y) = 10mm±0.5mm
Length(x) = 20mm±0.5mm, 10mm±0.2mm, 5mm±0.1mm, 2.5mm±0.1mm or 1mm±0.05mm

Periods: 21.00, 21.50, 22.00, 22.50, 23.00µm

NOTES:

1 The SFG device material is Magnesium doped lithium niobate with five periodically poled gratings. Each grating is 1.0mm wide with individual periods as listed above. A saw-cut reference mark is provided on the +z face of the crystal to determine the largest grating period (see above diagram). Each poled grating is separated by 0.2mm wide regions of unpoled material.

2 The average mark-to-space ratio of each grating is better than 70:30.

3 Each device is etched to make the poled gratings visible. Due to the wet-etch nature of this process the top and bottom surface finish of each device may appear cloudy or uneven.

4 Perpendicularity of facets F1 and F2 to gratings is within ± 0.15°. Parallelism between end facets F1 and F2 is within ± 5 minutes.

5 Optical finish of facets F1 and F2 is within 20/10 scratch dig with λ/8@1064nm. No more than two 100µm size chips per end facet.

6 AR coated to less than 5% reflectivity at 770-890nm, 0.25% at 1064nm and 5% at 2.85-4.9um on both facets.

31-05-10		Page 1 of 1

APPENDIX C

Intarsia Cavity Design Example

Screenshot of the cavity design calculation for the parametric module.

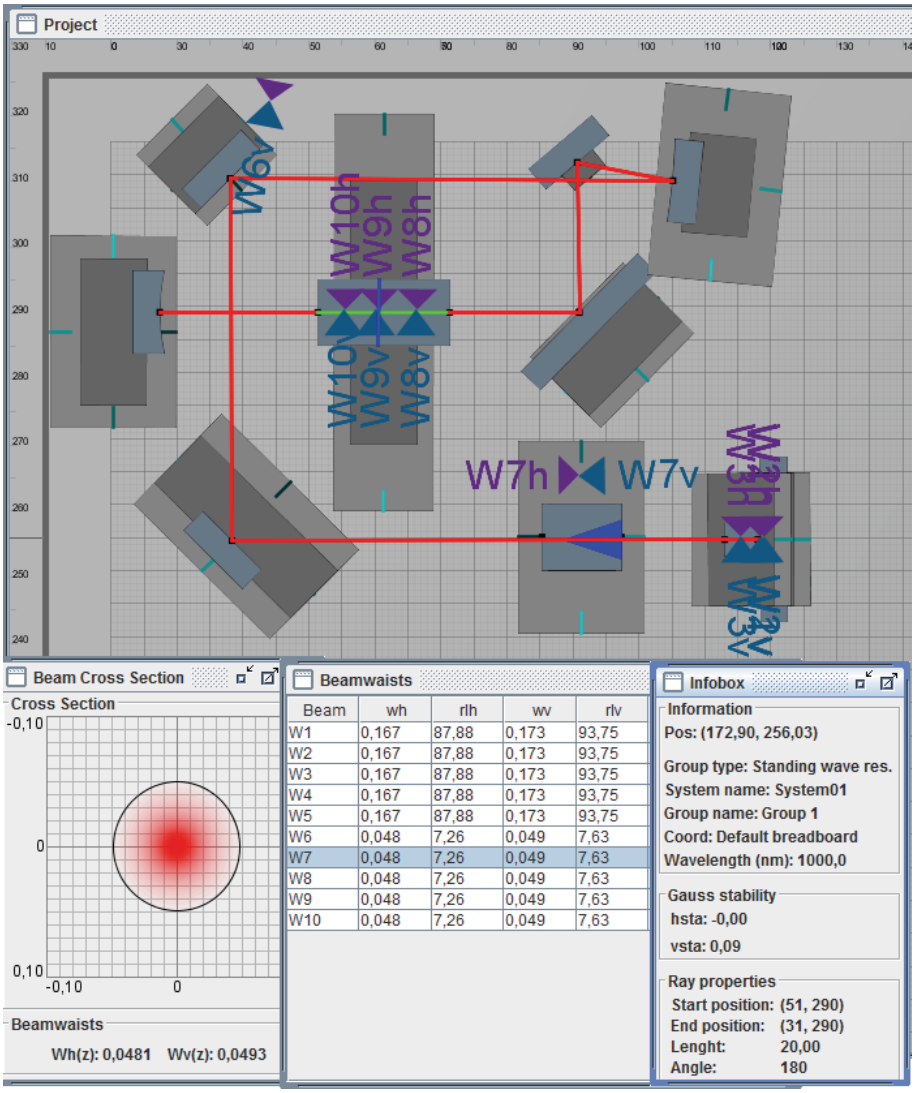

Beam	wh	rlh	wv	rlv
W1	0,167	87,88	0,173	93,75
W2	0,167	87,88	0,173	93,75
W3	0,167	87,88	0,173	93,75
W4	0,167	87,88	0,173	93,75
W5	0,167	87,88	0,173	93,75
W6	0,048	7,26	0,049	7,63
W7	0,048	7,26	0,049	7,63
W8	0,048	7,26	0,049	7,63
W9	0,048	7,26	0,049	7,63
W10	0,048	7,26	0,049	7,63

APPENDIX D

Aligment Procedure - Parametric Module Cavity

1. Make sure that all optical surfaces in the cavity are clean and free for dust.
2. Adjust focus of the pump diode to be as symmetric as possible.
3. Focus the pump diode to the laser crystal in a beamwaist that corresponds to the cavity beamwaist. This can be fine-tuned once the laser cavity is running.
4. Align a linear cavity of the laser crystal end-facet and a plane support-mirror, high reflective for 1064 nm. The plane-plane cavity is stable due to the thermal lensing in the laser crystal.
5. Align the main cavity such that the beam from the support cavity overlap with itself after a full roundtrip. Coupled cavity lasing is observed when the alignment is close to the optimum. Intracavity pinholes placed on the oven can help to ensure a straight pass through the PPLN crystal. Take care of the close pass at the D-mirror, the beam waist here is $> 300\,\mu m$.
6. Place the PPLN crystal in the oven in the cavity.
7. Repeat 4 if necessary.
8. Remove the support mirror.
9. Tune the cavity to highest possible power in a TEM_{00} mode by adjusting the mirror tilt and angle for the three adjustable mirrors. The intracavity power monitoring should be done with a leak from one of the two mirrors with normal incidence.
10. In case of first alignment: Optimize the laser crystal position with respect to output power and mode shape.
11. Control the PPLN crystal position by observing the green fluorescence and adjust if necessary. Fine tuning of the PPLN crystal position might affect the intracavity power.
12. Repeat 8 for last optimization.

APPENDIX E

Poster Presented at ASSL Paris 2013

Advanced Solid State Lasers, Optical Society of America, JTh2A. 23

DTU Fotonik
Department of Photonics Engineering

Optical Sensor Technology Group

Mid-infrared seeded optical parametric amplified light source

Lasse Høgstedt*, Peter Tidemand-Lichtenberg, Christian Pedersen
Technical University of Denmark, lhog@fotonik.dtu.dk

Abstract

We present a two stage pulsed mid-infrared light source based on non-linear down-conversion of light. The light source is single frequency, tunable, all passive and single moded.

Three configurations are presented:

- Spontaneous parametric fluorescense (un-seeded)
- Near infrared (NIR) seed
- Mid-infrared (MIR) seed

Introduction

A single frequency, tunable and pulsed light source is needed to construct a successful system for remote gas detection. This could be deployed in a differential absorption LIDAR (DIAL) system.

Previous work, [1-3] on seeded OPA's have primarily focused on seeding at the NIR wavelength in the DFG process, whereas this project presents the results from MIR seeding.

The output wavelengths are defined from the energy and momentum conservation in the difference frequency generation in the OPA

$$\frac{1}{\lambda_3} = \frac{1}{\lambda_2} - \frac{1}{\lambda_1} \qquad k_1 - k_2 - k_3 \qquad |k_3| = \frac{2\pi}{\lambda_3} n(\lambda_3, T)$$

where λ_3 is the generated mid-IR light, λ_2 the passive Q-switched laser, λ_{id} the residual energy from the pump photon and the **k**'s is the corresponding wave numbers.

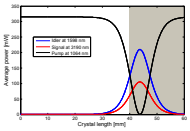

A simulated example of the average power evolution through an OPA crystal, seeded at the MIR wavelength.

Setup

The all passive setup consists of four main parts: An OPA, two seeds and an OPA pump.

- The mid-IR seed is a single frequency, tunable CW lightsource based on DFG mixing between a tunable 1 W 800 nm laser and a 1064 nm intracavity field. [4]
- For the NIR seed a tunable Ando AQ4321D is used.
- The OPA pump is a passive Q-switched laser build with Nd/Cr:YAG-crystals [5]. The pulse width is 7 ns, the repetition rate 5 KHz and the pulse energy 75 µJ
- In the final stage all beams overlap in a 40 mm long temperature controlled 5 % MgO doped PPLN crystal.

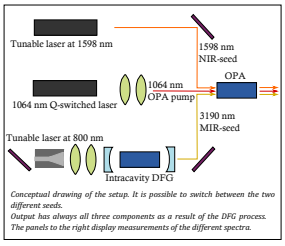

Conceptual drawing of the setup. It is possible to switch between the two different seeds.
Output has always all three components as a result of the DFG process.
The panels to the right display measurements of the different spectra.

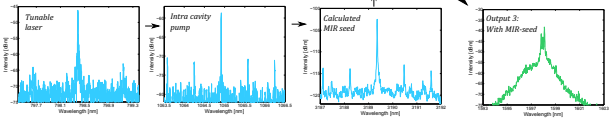

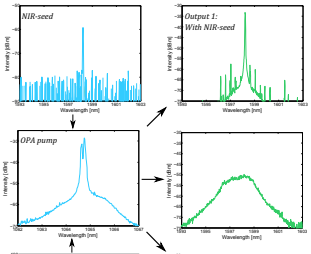

Results

If the OPA is seeded and measured at the same wavelength the spectral output will reflect the width of the seed, whereas it will represent the width of the OPA pump if the seed is shifted to the other wavelength.

At the MIR wavelength the peak width is calculated to shift the FWHM from ~2 nm with the NIR seed to 0.1 nm with the MIR seed.

To the right is an example of the MIR output where the NIR-case is the convolution between the OPA pump and the NIR-seed, and the MIR-case represents an amplification of the calculated MIR seed.

The power levels give a feeling of the different conversion efficiencies. All the intensities on the spectra have an arbitrary reference level.

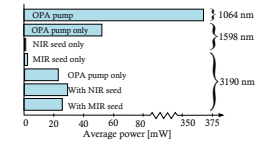

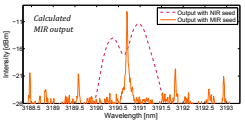

Conclusion

- We have demonstrated a tunable, pulsed mid-IR light source based on parametric down-conversion of light.
- The results show that the spectral width of the output decreases significantly when we seed directly at the mid-IR wavelength.
- The system proofs a general method to produce high quality mid-IR pulses with an all passive system over a wide range of frequencies

Outlook

- A measurement of the mid-IR spectrum directly with a monochromator and investigate the pulse to pulse stability.
- Apply the light source for remote gas sensing.

References:

1) *P.E. Powers, K.W. Aniolek, T.J. Kulp, B.A. Richman, and S.E. Bisson, Opt. Lett., 23,1886 (1998)*
2) *T.J. Kulp, S.E. Bisson, R.P. Bambha, T.A. Reichardt, U.-B. Goers, K.W. Aniolek, D.A.V. Kliner, A.A. Richman, K.M. Armstrong, R. Sommers, B. Schmitt, P.E. Powers, O. Levi, T. Pinguet, M. Fejer, J.P. Koplow, L. Goldberg, T.G. Mcrae, Appl. Phys. B 75, 317–327 (2002)*
3) *A. R. Pandey, P. E. Powers, and J. W. Haus, IEEE J. Quantum Electron, 44, 203 (2008)*
4) *L. Høgstedt, O. B. Jensen, J. S. Dam, C. Pedersen, P. Tidemand-Lichtenberg, Laser Physics, 22, 1676 (2012)*
5) *P.T. Lichtenberg, M. T. Andersen, S. Johansson, C. Canalias, F. Laurell, P. Buchhave, E. Karamehmedovic, C. Pedersen, Opt. Expr. 15, 9799 (2007)*

APPENDIX F

Poster Presented at ASSL Berlin 2015

Advanced Solid State Lasers, Optical Society of America, AM5A. 6

DTU Fotonik
Department of Photonics Engineering

Optical Sensor Technology Group

Design of a solid state laser for low noise upconversion detection

Lasse Høgstedt*, Peter Tidemand-Lichtenberg, Christian Pedersen
Technical University of Denmark, lhog@fotonik.dtu.dk

Abstract

We present an analysis of a solid state mixing laser used for upconversion of infrared to visible light.

It is demonstrated how to optimize the upconversion process for maximum signal-to-noise ratio, when used in a detector system.

It is found that the mixing laser intensity should be 300 KW/cm² in the system example.

Introduction

Detectors in the near infrared region are used for spectroscopic gas detection, e.g. CO_2 in the atmosphere at 1572 nm [1]. An InGaAs semiconductor detector is the typical choice, but the quantum efficiency (QE) is low and the dark noise high at room temperature.

If the wavelength of the signal is converted to the visible region it is possible to detect the light using highly efficient low noise silicon detectors [2,3]. The conversion results from the addition of energy in a nonlinear sum frequency generation (SFG) process with an efficiency defined as

$$\eta_{NIR\to VIS} = \frac{8\pi^2 d_{eff}^2}{\epsilon_0 c n_{1064} n_{635} n_{1572} \lambda_{vis}} I_{1064} L \,\mathrm{sinc}^2\left(\frac{|\Delta k| L}{2}\right)$$

One of the main challenges with efficient signal upconversion is the noise from spontanous parametric downconversion (SPDC) [4]. The problem is enhanced by random poling errors in the nonlinear crystal, that induce a non-zero phasematch at all wavelengths [5].

The SPDC is upconverted to the signal wavelength and the phasesmatch for the combined process is illustrated below.

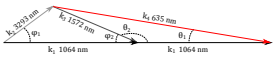

$\Delta k_{SPDC} = k_2 + k_3 - k_1 + k_{span}$ and $\Delta k_{SFG} = k_1 + k_2 - k_4 + k_{span}$, where $k(T, \lambda)$

Setup

The upconversion module consist of a 1064 nm high finesse laser cavity with a periodically poled lithium niobate crystal placed intracavity. Three points for efficient upconversion are emphasized:

- A compact and robust design ensure stability and easy in- and output coupling.
- A small beamwaist inside the nonlinear crystal and a finesse>400 ensure a high intensity mixing field.
- The nonlinear crystal is placed inside an oven on a translation stage. This allows for tuning of the specific phasematch by temperature tuning and/or shifting between the five poling channels.

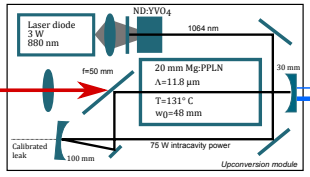

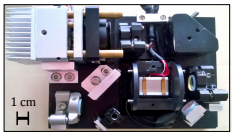

Sketch of the solid state laser that defines the upconversion module. All mirrors have losses below 0.02% at 1064 nm.

Image of the realization of the upconversion module.

Noise

There exist five different noise sources in the upconversion process, all visible on the plot below, displaying the output with no signal in.

- **Upconverted SPDC noise**, enters both as a peak at the signal wavelength and as a pedestal around. Cannot be filtered away.
- **Thermal noise**, essentially at all wavelengths. Low in NIR region. Typically not phasematched. Mostly filtered away.
- **Raman noise**, **higher order phase-matching** and **laser diode residual**. All three typically not at the signal wavelength. Can be filtered away.

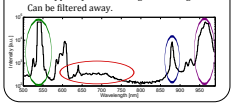

Signal-to-noise ratio

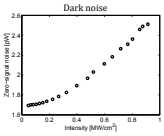

The dominant noise source in the upconversion process after narrow-band filtering is upconverted SPDC.

It depends quadratically on the mixing field intensity as the efficiency for both processes depend linearly on this intensity.

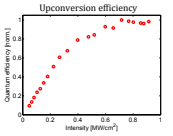

At low intensities the efficiency of the upconversion process is linear. At higher efficiencies the signal depletes and the intensity dependency become sinusoidal.

QE>80% have been demonstrated with this system.

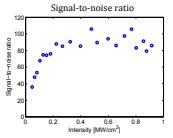

With a quadratic dependency for the dominant noise source and a QE that saturates at high intensities there is an optimum for the SNR of the upconversion process.

From the plot the optimum for the specific system is I_{1064}=300 KW/cm².

Few photon infrared signal

Few photon infrared signal

Few photon infrared signal

Visible noise photons

Few photon visible signal

Visible noise photons

InGaAs - detector
Low QE, high noise

Conclusion

We have demonstrated a high finesse solid state laser module optimized for up-conversion of infrared light to visible light.

The analysis show how upconverted SPDC noise dominate and that an optimum SNR is reached with I_{1064}=300 KW/cm².

Outlook

This general optimization approach for upconversion detection can be applied for longer wavelength detection systems with different poling periods.

The system performance should be tested against state-of-art NIR detection systems [6].

Silicon - detector
High QE, low noise

References:

1) *Ehret, G., Kiemle, C., Wirth, M., Amediek, A., Fix, A., Houweling, S. "Space-borne remote sensing of CO_2, CH_4, and N_2O by integrated path differential absorption lidar: a sensitivity analysis", Applied Physics B,* **90**, *(2008)*
2) *L. Høgstedt, J. S. Dam, A. Sahlberg, Z. Li, M. Aldén, C. Pedersen, and P. Tidemand-Lichtenberg, "Low-noise mid-IR upconversion detector for improved IB-degenerate four-wave mixing gas sensing", Optic Letters* **39** *(2014).*
3) *T. Wong, J. Fu, Y. Bai, W. Johnson, S. Own, M. Petrus, and U. N. Singh, "Sensitive infrared signal detection by upconversion technique," Optical Engineering* **53**, *(2014).*
4) *C.L. Tang, "Spontaneous Emission in the Frequency Up-Conversion Process in Nonlinear Optics", Physical Review* **182**, *(1969).*
5) *J. S. Pelc, C. R. Phillips, D. Chang, C. Langrock and M. M. Fejer, "Efficiency pedestal in quasi-phase-matching devices with random duty-cycle errors", Optic Letters* **36**, *(2011)*
6) *L. Høgstedt, M. Wirth, C. Pedersen, and P. Tidemand-Lichtenberg, "Upconversion based long range CO_2 DIAL measurements" - to be submitted*

APPENDIX G

Selected Noise Spectra of the Upconversion Process

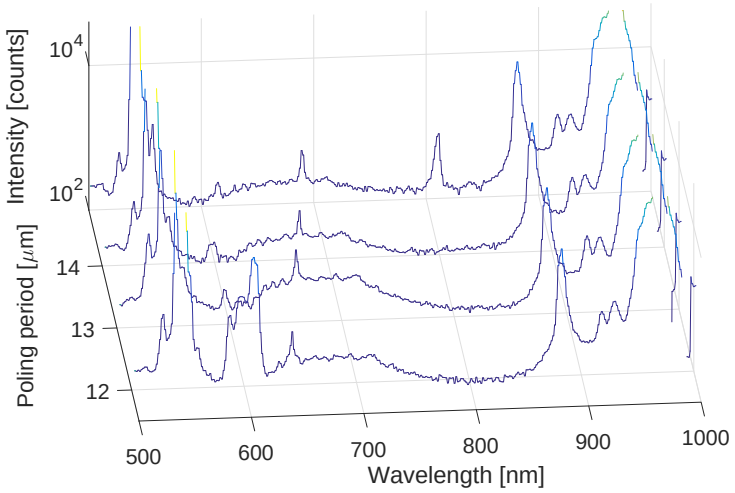

Figure G.1: Output noise spectra for four poling periods: 11.8 µm, 12.8 µm, 13.8 µm, 14.8 µm. The peak at 810 nm in the last spectra is scattering from a different laser setup. Measured with an Ocean Optics QE6500 spectrometer.

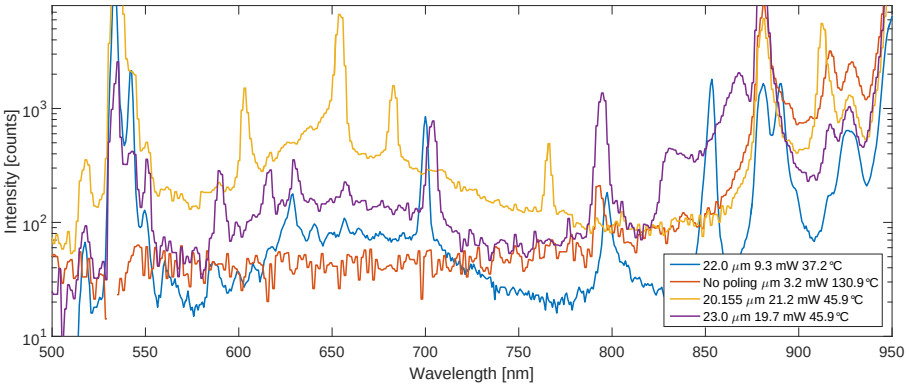

Figure G.2: Output noise spectra for two different poling periods and at a position in the crystal with no poling. Measured with an Ocean Optics QE6500 spectrometer.

APPENDIX H

Statistical Data for Poling Period Measurements

Table H.1: Statistical poling data, stated for low/high domain. The star mark the crystal data used in the thesis.

	Mean [µm]	Std [µm]	RDC [%]
11.8 - 02*	6.00/6.02	0.74/0.68	11.3/12.4
11.8 - 01	6.26/5.78	0.80/0.76	12.8/13.2
22.0 - 02	11.7/11.7	0.49/0.49	4.5/4.2
22.0 - 03	10.3/11.9	0.59/0.53	5.7/4.4

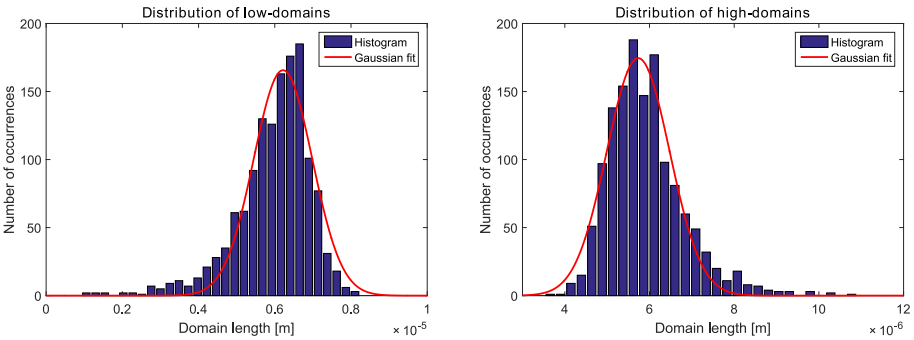

Figure H.1: Distribution of poling domains in the crystal 1 with $\Lambda = 11.8\mu m$.

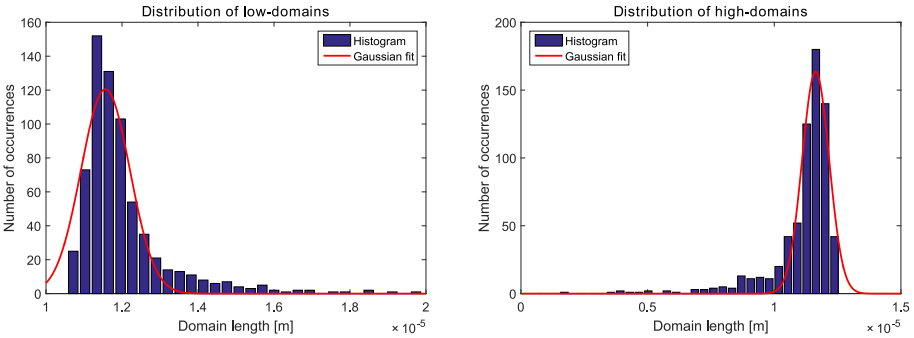

Figure H.2: Distribution of poling domains in the crystal 2 with $\Lambda = 22.0\mu m$.

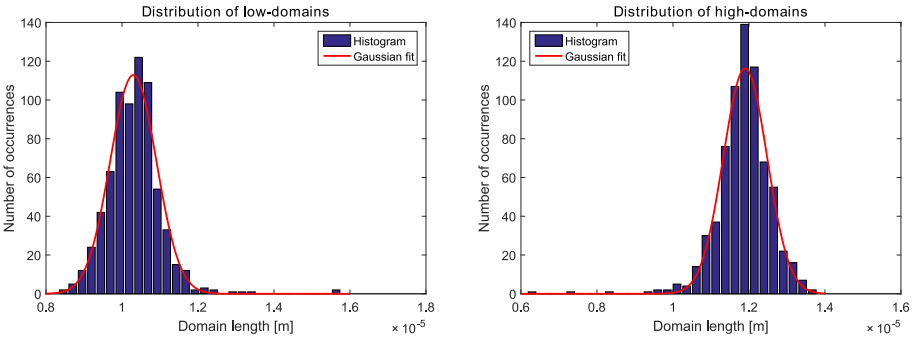

Figure H.3: Distribution of poling domains in the crystal 3 with $\Lambda = 22.0\mu$m.

APPENDIX I

Model Comparison with Identical Random Gratings

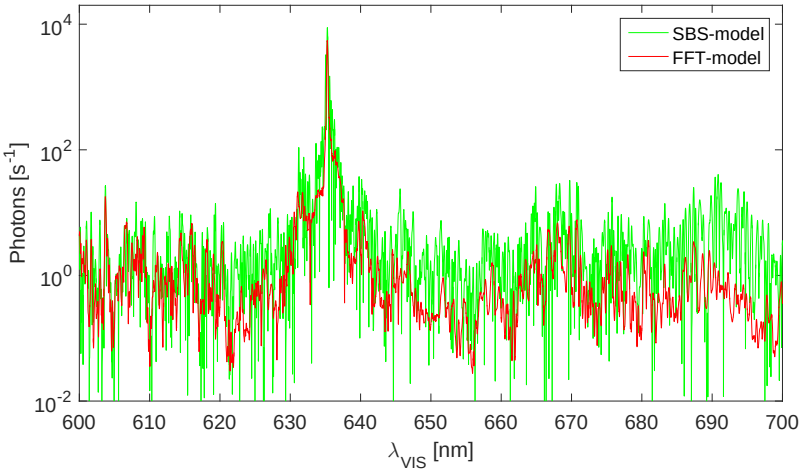

Figure I.1: Simulated output noise spectrum from the upconversion process with a poling period on 11.8 µm, 20 mm long PPLN crystal, a mixing field intensity at 637 kW and a PPLN temperature at 130°C. The two models got the exact same random grating as input.

APPENDIX J

Poster Presented at Photonics West 2014

SPIE LASE, International Society for Optics and Photonics, 89641H-89641H-6

DTU Fotonik
Department of Photonics Engineering

Optical Sensor Technology Group

Upconversion enhanced degenerate four-wave mixing in the mid-infrared for sensitive detection of acetylene in gas flows

Lasse Høgstedt[a], Jeppe Seidelin Dam*[a], Anna-Lena Sahlberg[b], Zhongshan Li[b], Marcus Aldén[b], Christian Pedersen[a], Peter Tidemand-Lichtenberg[a]
[a]Technical University of Denmark, Dept. of Photonics Engineering, Frederiksborgvej 399, 4000 Roskilde, Denmark
[b]Lund University, Dept. of Physics, Combustion Physics, Professorsgatan 1, SE-223 63 Lund, Sweden

Abstract

We present a new background free method for in situ gas detection. A combination of degenerate four-wave mixing and an infra-red light detector based on parametric frequency upconversion.

It is demonstrated that the system is able to cover more than 100 nm in scanning range and detect concentrations below 1 ppm based on the R9e acetylene line.

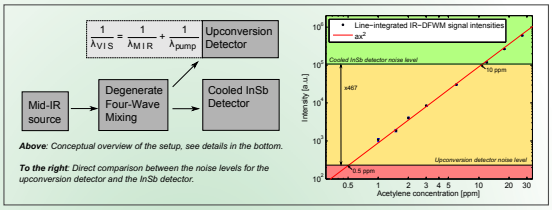

Above: *Conceptual overview of the setup, see details in the bottom.*

To the right: *Direct comparison between the noise levels for the upconversion detector and the InSb detector.*

Data analysis

From data to spectrum with the upconversion detector:

- Acquire one image per pulse
- Subtract background
- Define the pixel selection area
- Sum the pixels in each frame
- Construct a spectrum from all frames

Three examples of scattering influence are displayed in figure 3.

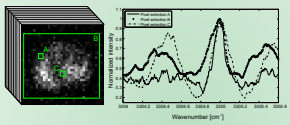

Data from three different pixel selections in images from the upconversion detector. B simulates a case without pixel selection, A and B demonstrates the best and worst case scenario respectively. Measured at an acetylene concentration of 11 ppm.

Results

From scans with the two detectors it was possible to demonstrate close to a 500 times improvement in detector noise level. This was both due to spatial filtering of the scattering and the inherent lower noise levels in the visible light detector.

The spectra below show examples of spectra obtained with the two different detectors. The wide scan show how it was possible to cover a broad spectral region with a high dynamic range.

The detection levels are limited by scattering in the system and the lower limit of the flow controller.

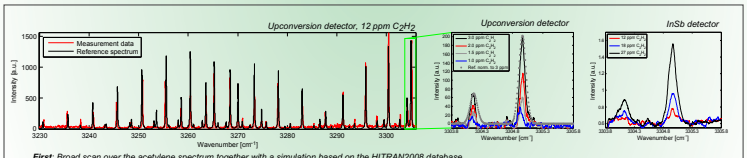

First: *Broad scan over the acetylene spectrum together with a simulation based on the HITRAN2008 database.*
Second and third: *Scan over the R9e acetylene line for various concentrations with the upconversion detector and the InSb detector respectively. Both are an average of 10 scans and all have running average on 20 points.*

Description of experiment

The mid-infrared light is generated by a tunable DFG system [1] and split into four beams using the specially designed IR-BOXCAR plates [2]. Three of these beams are focused into the middle of the gas tube. The signal beam is collimated and directed to the detectors.

The upconversion detector [3] consists of two parts, a conversion unit and a CCD based camera. In the conversion unit the mid-infrared light is focused into a 20 mm long periodically poled 5% MgO doped lithium niobate crystal. Here it is mixed with a intra-cavity field of a 1064 nm laser in order to generate light at the sum-frequency around 800 nm. This is defined from the conservation of both energy and momentum.

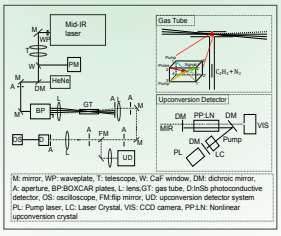

M: mirror, WP: waveplate, T: telescope, W: CaF window, DM: dichroic mirror, A: aperture, BP:BOXCAR plates, L: lens,GT: gas tube, D:InSb photoconductive detector, OS: oscilloscope, FM:flip mirror, UD: upconversion detector system PL: Pump laser, LC: Laser Crystal, VIS: CCD camera, PP-LN: Nonlinear upconversion crystal

Conclusion

- We have demonstrated gas sensing with a DFWM system combined with an upconversion detector for the mid-IR region.
- Results show sub-ppm acetylene detection levels and a noise level improvement of approx. 500 times compared to a cryogenically cooled InSb detector.
- The imaging capabilities of the upconversion detector allows spatial filtering of the system scattering, in order to lower the main noise source.

References:
[1] Li, Z. S., Hu, C. H., Zetterberg, J., Linvin, M., Alden, M., "Midinfrared polarization spectroscopy of OH and hot water in low pressure lean premixed flames," Journal of Chemical Physics 127, 084310 (2007)
[2] Sun, Z. W., Li, Z. S., Li, B., Alden, M., Ewart, P., "Detection of C2H2 and HCl using mid-infrared degenerate four-wave mixing with stable beam alignment: towards practical in situ sensing of trace molecular species," Applied Physics B: Lasers and Optics 98, 593-600 (2010)
[3] Dam, J. S., Tidemand-Lichtenberg, P., and Pedersen, C., "Room-temperature mid-infrared single-photon spectral imaging," Nature Photonics 6, 788–793 (2012)

DTU
LUND UNIVERSITY

Bibliography

[1] *Commercial laser lines*. 2015. URL: https://en.wikipedia.org/wiki/Laser#/media/File:Commercial_laser_lines.svg.

[2] *Optical Detection Systems - Technocal Note*. 2015. URL: http://www.newport.com/Technical-Note-Optical-Detection-Systems/397680/1033/content.aspx.

[3] P. A. Franken, A. E. Hill, C. W. Peters, and G. Weinreich. "Generation of Optical Harmonics". In: *Physical Review Letters* 7.4 (Aug. 15, 1961), pp. 118–119.

[4] J. A. ARMSTRONG, N. Bloembergen, J. Ducuing, and P.S. Pershan. "Interactions between Light Waves in a Nonlinear Dielectric". In: *PHYSICAL REVIEW* 127.1918 (1962).

[5] J. E. Midwinter and J. Warner. "Up-Conversion of Near Infrared to Visible Radiation in Lithium-Meta-Niobate". In: *Journal of Applied Physics* 38.2 (1967), pp. 519–523.

[6] R. L. Byer and S. E. Harris. "Power and Bandwidth of Spontaneous Parametric Emission". In: *Physical Review* 168.3 (Apr. 15, 1968), pp. 1064–1068.

[7] C. L. Tang. "Spontaneous Emission in the Frequency Up-Conversion Process in Nonlinear Optics". In: *Physical Review* 182.2 (June 10, 1969), pp. 367–374.

[8] G. D. Boyd and D. A. Kleinman. "Parametric Interaction of Focused Gaussian Light Beams". In: *Journal of Applied Physics* 39.8 (July 1, 1968), pp. 3597–3639.

[9] Tr Gurski, Hw Epps, and Sp Maran. "Astronomical Demonstration of an Infrared Upconverter". In: *Nature* 249.5458 (1974), pp. 638–639.

[10] M. M. Abbas, T. Kostiuk, and K. W. Ogilvie. "Infrared upconversion for astronomical applications". In: *Applied Optics* 15.4 (Apr. 1, 1976), pp. 961–970.

[11] Rw Boyd. "Infrared Upconversion for Astronomy". In: *Optical Engineering* 16.6 (1977), pp. 563–568.

[12] J. Falk and Yc See. "Internal CW Parametric Upconversion". In: *Applied Physics Letters* 32.2 (1978), pp. 100–101.

[13] Y. C. See, Shekhar Guha, and Joel Falk. "Limits to the NEP of an intracavity LiNbO3 upconverter". In: *Applied Optics* 19.9 (May 1, 1980), pp. 1415–1418.

[14] Rostislav V. Roussev, Carsten Langrock, Jonathan R. Kurz, and M. M. Fejer. "Periodically poled lithium niobate waveguide sum-frequency generator for efficient single-photon detection at communication wavelengths". In: *Optics Letters* 29.13 (2004), p. 1518.

[15] J. S. Pelc, C. R. Phillips, D. Chang, C. Langrock, and M. M. Fejer. "Efficiency pedestal in quasi-phase-matching devices with random duty-cycle errors". In: *Optics Letters* 36.6 (Mar. 15, 2011), pp. 864–866.

[16] J. S. Pelc, C. Langrock, Q. Zhang, and M. M. Fejer. "Influence of domain disorder on parametric noise in quasi-phase-matched quantum frequency converters". In: *Optics Letters* 35.16 (Aug. 15, 2010), pp. 2804–2806.

[17] J. S. Pelc, L. Ma, C. R. Phillips, Q. Zhang, C. Langrock, O. Slattery, X. Tang, and M. M. Fejer. "Long-wavelength-pumped upconversion single-photon detector at 1550 nm: performance and noise analysis". In: *Optics Express* 19.22 (Oct. 24, 2011), p. 21445.

[18] Paulina S. Kuo, Jason S. Pelc, Oliver Slattery, Yong-Su Kim, M. M. Fejer, and Xiao Tang. "Reducing noise in single-photon-level frequency conversion". In: *Optics Letters* 38.8 (Apr. 15, 2013), p. 1310.

[19] Haiyun Xia, Guoliang Shentu, Mingjia Shangguan, Xiuxiu Xia, Xiaodong Jia, Chong Wang, Jun Zhang, Jason S. Pelc, M. M. Fejer, Qiang Zhang, Xiankang Dou, and Jian-Wei Pan. "Long-range micro-pulse aerosol lidar at 15 m with an upconversion single-photon detector". In: *Optics Letters* 40.7 (Apr. 1, 2015), p. 1579.

[20] Haifeng Pan and Heping Zeng. "Efficient and stable single-photon counting at 1.55 m by intracavity frequency upconversion". In: *Optics Letters* 31.6 (Mar. 15, 2006), pp. 793–795.

[21] Teh-Hwa Wong, Jirong Yu, Yingxin Bai, William Johnson, Songsheng Chen, Mulugeta Petros, and Upendra N. Singh. "Sensitive infrared signal detection by upconversion technique". In: *Optical Engineering* 53.10 (2014), pp. 107102–107102.

[22] R. Baudoin. "Sum frequency generation process for a new astronomical instrument". In: *Proceedings of Spie - the International Society for Optical Engineering* 8964 (2014).

[23] Jeppe Seidelin Dam, Christian Pedersen, and Peter Tidemand-Lichtenberg. "High-resolution two-dimensional image upconversion of incoherent light". In: *Optics Letters* 35.22 (Nov. 15, 2010), p. 3796.

[24] Jeppe Seidelin Dam, Peter Tidemand-Lichtenberg, and Christian Pedersen. "Room-temperature mid-infrared single-photon spectral imaging". In: *Nature Photonics* 6.11 (Nov. 2012), pp. 788–793.

[25] Qi Hu, Jeppe Seidelin Dam, Christian Pedersen, and Peter Tidemand-Lichtenberg. "High-resolution mid-IR spectrometer based on frequency upconversion". In: *Optics Letters* 37.24 (Dec. 15, 2012), p. 5232.

[26] Louis Martinus Kehlet, Peter Tidemand-Lichtenberg, Jeppe Seidelin Dam, and Christian Pedersen. "Infrared upconversion hyperspectral imaging". In: *Optics Letters* 40.6 (Mar. 15, 2015), p. 938.

[27] Malcolm H. Dunn and Majid Ebrahimzadeh. “Parametric Generation of Tunable Light from Continuous-Wave to Femtosecond Pulses”. In: *Science* 286.5444 (Nov. 19, 1999), pp. 1513–1517.

[28] Valentin Petrov. “Frequency down-conversion of solid-state laser sources to the mid-infrared spectral range using non-oxide nonlinear crystals”. In: *Progress in Quantum Electronics* 42 (2015), pp. 1–106.

[29] L. E. Myers, R. C. Eckardt, M. M. Fejer, R. L. Byer, W. R. Bosenberg, and J. W. Pierce. “Quasi-phase-matched optical parametric oscillators in bulk periodically poled LiNbO3”. In: *Journal of the Optical Society of America B* 12.11 (Nov. 1, 1995), pp. 2102–2116.

[30] U. Bäder, T. Mattern, T. Bauer, J. Bartschke, M. Rahm, A. Borsutzky, and R. Wallenstein. “Pulsed nanosecond optical parametric generator based on periodically poled lithium niobate”. In: *Optics Communications* 217.1 (Mar. 1, 2003), pp. 375–380.

[31] Kenji Numata, Steve Li, Haris Riris, Stewart Wu, Antonios Seas, Anthony Yu, Michael Krainak, and James Abshire. “Seeded nanosecond optical parametric generator for trace gas measurements”. In: *Proc. of SPIE*. Nonlinear Frequency Generation and Conversion: Materials, Devices, and Applications IX. Vol. 7582. 2010, 75820K–75820K–6.

[32] P. E. Powers, K. W. Aniolek, T. J. Kulp, B. A. Richman, and S. E. Bisson. “Periodically poled lithium niobate optical parametric amplifier seeded with the narrow-band filtered output of an optical parametric generator”. In: *Optics Letters* 23.24 (Dec. 15, 1998), p. 1886.

[33] John H. Marquardt, Ross W. Mackes, and Duane D. Smith. “Single-Mode, Tunable Output from a Midwave-Infrared-Seeded Optical Parametric Oscillator System”. In: *Applied Optics* 41.6 (Feb. 20, 2002), p. 1163.

[34] John J. Zayhowski. “Periodically poled lithium niobate optical parametric amplifiers pumped by high-power passively Q-switched microchip lasers”. In: *Optics Letters* 22.3 (Feb. 1, 1997), p. 169.

[35] Q. Clément, J.-M. Melkonian, J.-B. Dherbecourt, M. Raybaut, A. Grisard, E. Lallier, B. Gérard, B. Faure, G. Souhaité, and A. Godard. “Long-wave infrared, single-frequency, tunable, pulsed optical parametric oscillator based on orientation-patterned GaAs for gas sensing”. In: *Optics Letters* 40.12 (June 15, 2015), p. 2676.

[36] Karsten Rottwitt and Peter Tidemand-Lictenberg. *Nonlinear Optics*. CRC Press, 2015.

[37] B.E.A. Saleh and M.C. Teich. *Fundamentals of photonics*. second edition. Wiley, 2009.

[38] Robert W. Boyd. *Nonlinear Optics*. Third edition. Academic Press, 2008.

[39] O. Gayer, Z. Sacks, E. Galun, and A. Arie. “Temperature and wavelength dependent refractive index equations for MgO-doped congruent and stoichiometric LiNbO3”. In: *Applied Physics B* 91.2 (Apr. 11, 2008), pp. 343–348.

[40] William H. Press, Brian P. Flannery, Saul A. Teukolsky, and William T. Vetterling. *Numerical Recipes in C book set: Numerical Recipes in C: The Art of Scientific Computing*. 2 edition. Cambridge ; New York: Cambridge University Press, Oct. 30, 1992. 1020 pp.

[41] M.M. Fejer, G.A. Magel, Dieter H. Jundt, and R.L. Byer. "Quasi-phase-matched second harmonic generation: tuning and tolerances". In: *IEEE Journal of Quantum Electronics* 28.11 (Nov. 1992), pp. 2631–2654.

[42] Anders C. Bilfeldt. "Numerical modeling of optical parametric frequency conversion". Master thesis. Photonics Engineering, Optical Sensor Technology group: Technical University of Denmark, 2014.

[43] Preben Buchhave. "Generation of higher order Gauss-Laguerre modes in single-pass 2nd harmonic generation". In: *Optics Express* 16.22 (2008), pp. 17952–17961.

[44] Sasson Somekh and Ammon Yariv. "Phase matching by periodic modulation of the nonlinear optical properties". In: *Optics Communications* 6.3 (Nov. 1, 1972), pp. 301–304.

[45] L. Arizmendi. "Photonic applications of lithium niobate crystals". In: *physica status solidi (a)* 201.2 (2004), pp. 253–283.

[46] *Covesion Guide to PPLN*. 2015. URL: `http://www.covesion.com/support/material-properties-of-lithium-niobate.html#materialproperties`.

[47] Ian E Barry, Graeme W Ross, Peter G. R Smith, Robert W Eason, and Gary Cook. "Microstructuring of lithium niobate using differential etch-rate between inverted and non-inverted ferroelectric domains". In: *Materials Letters* 37.4 (Nov. 1998), pp. 246–254.

[48] H. Ishizuki. "High-energy quasi-phase-matched optical parametric oscillation in a periodically poled MgO:LiNbO3 device with a 5 mm x 5 mm aperture". In: *Optics Letters* 30.21 (2005), pp. 2918–2920.

[49] L. Høgstedt, O. B. Jensen, J. S. Dam, C. Pedersen, and P. Tidemand-Lichtenberg. "500 nm continuous wave tunable single-frequency mid-IR light source for C-H spectroscopy". In: *Laser Physics* 22.11 (Oct. 1, 2012), pp. 1676–1681.

[50] Peter Tidemand-Lichtenberg, Martin T. Andersen, Sandra Johansson, Carlota Canalias, Fredrik Laurell, Preben Buchhave, Emir Karamehmedovic, and Christian Pedersen. "Nonlinear cavity dumping of a high finesse frequency mixing module". In: *Optics Express* 15.15 (2007), p. 9799.

[51] Bopeng Wang. "Quantum analysis of optical parametric fluorescence in the optical parametric amplification process". In: *Journal of Optics* 17.7 (2015), p. 075503.

[52] Pu Zhao, Baigang Zhang, Enbang Li, Rui Zhou, Degang Xu, Yang Lu, Tieli Zhang, Feng Ji, Xueyu Zhu, Peng Wang, and Jianquan Yao. "Experimental study on a high conversion efficiency, low threshold, high-repetition-rate periodically poled lithium niobate optical parametric generator". In: *Optics Express* 14.16 (2006), p. 7224.

[53] E.M. Daly and A.I. Ferguson. “Spatial and temporal dependence of single-pass parametric gain”. In: *Journal of Modern Optics* 48.4 (2001), pp. 729–744.

[54] H. J. Bakker, P. C. M. Planken, and H. G. Muller. “Numerical calculation of optical frequency-conversion processes: a new approach”. In: *Journal of the Optical Society of America B* 6.9 (Sept. 1, 1989), pp. 1665–1672.

[55] Christian Homann and Eberhard Riedle. “Direct measurement of the effective input noise power of an optical parametric amplifier”. In: *Laser & Photonics Reviews* 7.4 (July 1, 2013), pp. 580–588.

[56] H. Statz, G. A. DeMars, D. T. Wilson, and C. L. Tang. “Problem of Spike Elimination in Lasers”. In: *Journal of Applied Physics* 36.5 (May 1, 1965), pp. 1510–1514.

[57] B. W. Mayer. “Mid-infrared pulse generation via achromatic quasi-phase-matched OPCPA”. In: *Optics Express* 22.17 (2014), pp. 20798–20808.

[58] Ritwick Das, S. Chaitanya Kumar, G. K. Samanta, and M. Ebrahim-Zadeh. “Broadband, high-power, continuous-wave, mid-infrared source using extended phase-matching bandwidth in MgO:PPLN”. In: *Optics Letters* 34.24 (Dec. 15, 2009), p. 3836.

[59] Lasse Høgstedt, Peter Tidemand-Lichtenberg, and Christian Pedersen. “Direct Seeded Single Frequency mid-IR OPA all Passive Light Source”. In: Advanced solid state lasesrs. OSA, 2013, JTh2A.23.

[60] Ichiro Shoji, Takashi Kondo, Ayako Kitamoto, Masayuki Shirane, and Ryoichi Ito. “Absolute scale of second-order nonlinear-optical coefficients”. In: *Journal of the Optical Society of America B* 14.9 (Sept. 1, 1997), p. 2268.

[61] Yingxin Bai, Nianle Wu, Jian Zhang, Jiaqiang Li, Shiqun Li, Jun Xu, and Peizhen Deng. “Passively Q-switched Nd:YVO4 laser with a Cr4+:YAG crystal saturable absorber”. In: *Applied Optics* 36.12 (Apr. 20, 1997), p. 2468.

[62] R. F. SCHAUFELE and M. J. WEBER. “RAMAN SCATTERING BY LITHIUM NIOBATE”. In: *PHYSICAL REVIEW* 152.2 (1966), p. 705.

[63] L. J. Hu, Y. H. Chang, M. L. Hu, M. W. Chang, and W. S. Tse. “Effect of doping on the Raman modes in MgO-doped lithium niobate crystals”. In: *Journal of Raman Spectroscopy* 22.6 (1991), pp. 333–337.

[64] Andrey V. Okishev and Jonathan D. Zuegel. “Intracavity-pumped Raman laser action in a mid IR, continuous-wave (cw) MgO:PPLN optical parametric oscillator”. In: *Optics Express* 14.25 (2006), p. 12169.

[65] C. R. Phillips, J. S. Pelc, and M. M. Fejer. “Parametric processes in quasi-phasematching gratings with random duty cycle errors”. In: *Journal of the Optical Society of America B* 30.4 (Apr. 1, 2013), pp. 982–993.

[66] R. A. Andrews, Herbert Rabin, and C. L. Tang. “Coupled Parametric Downconversion and Upconversion with Simultaneous Phase Matching”. In: *Physical Review Letters* 25.9 (Aug. 31, 1970), pp. 605–608.

[67] Husam H. Abu-Safe. “Investigation of multiconversion processes in periodically poled LiNbO3-based optical parametric oscillators”. In: *Applied Optics* 44.34 (2005), p. 7458.

[68] K. G. Koprulu, T. Kartaloglu, Y. Dikmelik, and O. Aytur. “Single-crystal sum-frequency-generating optical parametric oscillator”. In: *Journal of the Optical Society of America B-Optical Physics* 16.9 (Sept. 1999), pp. 1546–1552.

[69] Ziya Gürkan Figen. “Seeded optical parametric generator with efficiency-enhanced mid-wave infrared beam output”. In: *Journal of Modern Optics* 61.15 (Sept. 2, 2014), pp. 1269–1281.

[70] Antoni Rogalski. *Infrared detectors*. 2nd edition. CRC Press, 2011.

[71] Lasse Høgstedt, Peter Tidemand-Lichtenberg, and Christian Pedersen. “Design of a solid state laser for low noise upconversion detection of near infrared light”. In: Advanced solid state lasesrs. OSA, 2015, AM5A.6.

[72] Carsten Langrock, Eleni Diamanti, Rostislav V. Roussev, Yoshihisa Yamamoto, M. M. Fejer, and Hiroki Takesue. “Highly efficient single-photon detection at communication wavelengths by use of upconversion in reverse-proton-exchanged periodically poled LiNbO3 waveguides”. In: *Optics Letters* 30.13 (2005), p. 1725.

[73] Amnon Yariv. *Quantum Electronics*. Third Edition. Wiley, 1989.

[74] Rasmus Lyngbye Pedersen. “1.9 m Laser System for Mid-IR Upconversion Detection”. Master thesis. Department of photnic engineering: Technical University of Denmark, 2015.

[75] Rasmus Pedersen, Peter Tidemand-Lichtenberg, and Lasse Høgstedt. “Tunable 1.9µm Laser System for Mid-IR Upconversion Detection”. In: Advanced solid state lasesrs. OSA, 2015, ATh1A.8.

[76] Lasse Høgstedt, Jeppe Seidelin Dam, Anna-Lena Sahlberg, Zhongshan Li, Marcus Aldén, Christian Pedersen, and Peter Tidemand-Lichtenberg. “Low-noise mid-IR upconversion detector for improved IR-degenerate four-wave mixing gas sensing”. In: *Optics Letters* 39.18 (Sept. 15, 2014), pp. 5321–5324.

[77] Lasse Høgstedt, Jeppe Seidelin Dam, Anna-Lena Sahlberg, Zhongshan Li, Marcus Aldén, Christian Pedersen, and Peter Tidemand-Lichtenberg. “Upconversion enhanced degenerate four-wave mixing in the mid-infrared for sensitive detection of acetylene in gas flows”. In: *Proc. SPIE 8964*. Vol. 8964. 2014, 89641H–89641H–6.

[78] Anna-Lena Sahlberg, Jeppe Dam Seidelin, Li Zhongshan, Lasse Høgstedt, and Peter Tidemand-Lichtenberg. “Mid-IR Imaging: Upconversion imager improves IR gas sensing”. In: *Laser Focus World* 50.11 (2014), pp. 53–55.

[79] Lasse Høgstedt, Andreas Fix, Martin Wirth, Christian Pedersen, and Peter Tidemand-Lichtenberg. “Upconversion-based lidar measurements of atmospheric CO2”. In: *Optics Express* 24.5 (2016), pp. 5152–5161.

[80] J. S. Pelc, Q. Zhang, C. R. Phillips, L. Yu, Y. Yamamoto, and M. M. Fejer. “Cascaded frequency upconversion for high-speed single-photon detection at 1550 nm”. In: *Optics Letters* 37.4 (Feb. 15, 2012), p. 476.

[81] Guo-Liang Shentu, Xiu-Xiu Xia, Qi-Chao Sun, Jason S. Pelc, M. M. Fejer, Qiang Zhang, and Jian-Wei Pan. “Upconversion detection near 2 m at the single photon level”. In: *Optics Letters* 38.23 (Dec. 1, 2013), p. 4985.

[82] Z. S. Li, M. Linvin, J. Zetterberg, J. Kiefer, and M. Aldén. “Mid-infrared polarization spectroscopy of C2H2: Non-intrusive spatial-resolved measurements of polyatomic hydrocarbon molecules for combustion diagnostics”. In: *Proceedings of the Combustion Institute* 31.1 (Jan. 2007), pp. 817–824.

[83] Z. W. Sun, Z. S. Li, B. Li, M. Aldén, and P. Ewart. “Detection of C2H2 and HCl using mid-infrared degenerate four-wave mixing with stable beam alignment: towards practical in situ sensing of trace molecular species”. In: *Applied Physics B* 98.2 (Feb. 1, 2010), pp. 593–600.

[84] Matthew R. McCurdy, Yury Bakhirkin, Gerard Wysocki, Rafal Lewicki, and Frank K. Tittel. “Recent advances of laser-spectroscopy-based techniques for applications in breath analysis”. In: *Journal of Breath Research* 1.1 (2007), p. 014001.

[85] William Rock, Yun-Liang Li, Philip Pagano, and Christopher M. Cheatum. “2D IR Spectroscopy using Four-Wave Mixing, Pulse Shaping, and IR Upconversion: A Quantitative Comparison”. In: *The Journal of Physical Chemistry A* 117.29 (July 25, 2013), pp. 6073–6083.

[86] Z. S. Li, M. Rupinski, J. Zetterberg, Z. T. Alwahabi, and M. Aldén. “Mid-infrared polarization spectroscopy of polyatomic molecules: Detection of nascent CO2 and H2O in atmospheric pressure flames”. In: *Chemical Physics Letters* 407.4 (May 27, 2005), pp. 243–248.

[87] L. S. Rothman et al. “The HITRAN2012 molecular spectroscopic database”. In: *Journal of Quantitative Spectroscopy and Radiative Transfer*. HITRAN2012 special issue 130 (Nov. 2013), pp. 4–50.

[88] Stocker, T.F., D. Qin, G.-K. Plattner, M. Tignor, S.K. Allen, J. Boschung, A. Nauels, Y. Xia, V. Bex, and P.M. Midgley. *Climate Change 2013: The Physical Science Basis: Working Group I Contribution to the Fifth Assessment Report of the Intergovernmental Panel on Climate Change*. Cambridge University Press, Mar. 24, 2014. 1553 pp.

[89] G. Ehret, C. Kiemle, M. Wirth, A. Amediek, A. Fix, and S. Houweling. “Space-borne remote sensing of CO2, CH4, and N2O by integrated path differential absorption lidar: a sensitivity analysis”. In: *Applied Physics B* 90.3 (Mar. 1, 2008), pp. 593–608.

[90] Andreas Fix, Axel Amediek, Christian Büdenbender, Gerhard Ehret, Mathieu Quatrevalet, Martin Wirth, Jens Löhring, Raphael Kasemann, Jürgen Klein, Dieter Hoffmann, and Volker Klein. "Development and First Results of A New Near-ir Airborne Greenhouse Gas Lidar". In: Advanced solid state lasers. OSA, 2015, ATh1A.2.

[91] Daisuke Sakaizawa, Chikao Nagasawa, Tomohiro Nagai, Makoto Abo, Yasukuni Shibata, Masahisa Nakazato, and Tetsu Sakai. "Development of a 16 um differential absorption lidar with a quasi-phase-matching optical parametric oscillator and photon-counting detector for the vertical CO2 profile". In: *Applied Optics* 48.4 (Feb. 1, 2009), p. 748.

[92] V. G. Dmitriev, G. G. Gurzadyan, and D. N. Nikogosyan. *Handbook of Nonlinear Optical Crystals*. 2nd. Springer, 1995.

[93] Jens Löhring, Jörg Luttmann, Raphael Kasemann, Michael Schlösser, Jürgen Klein, Hans-Dieter Hoffmann, Axel Amediek, Christian Büdenbender, Andreas Fix, Martin Wirth, Mathieu Quatrevalet, and Gerhard Ehret. "INNOSLAB-based single-frequency MOPA for airborne lidar detection of CO2 and methane". In: *Proc. of SPIE*. Solid State Lasers XXIII: Technology and Devices. Vol. 8959. 2014, 89590J–89590J–8.

[94] Jianhua Chang, Zhenbo Yang, and Qing Sun. "Broadband mid-infrared difference frequency generation in uniform grating periodically poled lithium niobate". In: *Optik - International Journal for Light and Electron Optics* 126.11 (June 2015), pp. 1123–1127.

[95] Ameneh Bostani, Meenu Ahlawat, Amirhossein Tehranchi, Roberto Morandotti, and Raman Kashyap. "Design, fabrication and characterization of a specially apodized chirped grating for reciprocal second harmonic generation". In: *Optics Express* 23.4 (Feb. 23, 2015), p. 5183.

[96] X. Sanchez-Lozano and Jose Luis Lucio. "Spontaneous parametric down conversion in chirped, aperiodically-poled crystals". In: *International Journal of Quantum Information* (July 2, 2015), p. 1550032. arXiv: 1412.7339.

[97] Huai-Dong Jiang, Huai-Jin Zhang, Ji-Yang Wang, Hai-Rui Xia, Xiao-Bo Hu, Bing Teng, and Cheng-Qian Zhang. "Optical and laser properties of Nd:GdVO4 crystal". In: *Optics Communications* 198.4 (Nov. 1, 2001), pp. 447–452.

[98] Q. S. He. "A study on the aerosol extinction-to-backscatter ratio with combination of micro-pulse LIDAR and MODIS over Hong Kong". In: *Atmospheric Chemistry and Physics* 6.11 (2006), p. 3243.

[99] Ravil Agishev, Barry Gross, Fred Moshary, Alexander Gilerson, and Samir Ahmed. "Simple approach to predict APD/PMT lidar detector performance under sky background using dimensionless parametrization". In: *Optics and Lasers in Engineering* 44.8 (Aug. 2006), pp. 779–796.

[100] *A Guide to Choosing the Right Detector*. 2015. URL: http://www.hamamatsu.com/us/en/community/optical_sensors/tutorials/guide_to_detector_selection/index.html.